DOCTOR OF SCIENCES

Probing the primordial Universe by detecting high-frequency gravitational waves with resonant electromagnetic cavities

Herman, Nicolas

Award date:
2023

Awarding institution:
University of Namur

UNIVERSITÉ DE NAMUR
FACULTÉ DES SCIENCES
DÉPARTEMENT DE MATHÉMATIQUE

Probing the primordial Universe by detecting high-frequency gravitational waves with resonant electromagnetic cavities

Thèse présentée par
Nicolas Herman
pour l'obtention du grade
de Docteur en Sciences

Composition du Jury :

Alexandre MAUROY (Président)
Andreas RINGWALD
Aldo EJLLI
Michaël LOBET
Sébastien CLESSE
Massimiliano RINALDI
André FŰZFA (Promoteur et secrétaire)

2023

Cover design: ©Presses universitaires de Namur

Rue Grandgagnage 19
B – 5000 Namur (Belgium)

Printed in Belgium.

ISBN: 978-2-39029-165-7
Registration of copyright: D/2023/1881/2

Université de Namur
Faculté des Sciences
rue de Bruxelles, 61, B-5000 Namur (Belgique)

Probing the primordial Universe by detecting high-frequency gravitational waves with resonant electromagnetic cavities

by Nicolas Herman

Abstract: The first detection of gravitational waves in 2015 by LIGO/VIRGO [Abbott et al., 2016] with interferometers is one of the most wonderful scientific achievements in this century, leading to a brand new astronomy era. The frequency content of such waves is at the order of the hertz, but there are several interests in much higher frequencies, above megahertz. Interferometers can not detect such high frequency content. In this thesis we are going to study high-frequency gravitational wave possible detection using electromagnetic fields, through the inverse Gertsenshtein effect. Our detector is a patented [Füzfa, 2018] cylindrical electromagnetic cavity immersed in an intense external magnetic field. We study how we could detect two high-frequency sources that are witnesses of the early Universe, which are primordial black holes and stochastic gravitational wave background. We will study analytically and numerically the possible detection of these signals, showing how we can get information about those primordial Universe objects.

Sonder l'Univers primordial en détectant des ondes gravitationnelles haute-fréquence grâce à des cavités électromagnétiques résonantes

par Nicolas Herman

Résumé : La première détection des ondes gravitationnelles en 2015 [Abbott et al., 2016] par des interféromètres est un des plus formidables exploits scientifiques de ce siècle, qui a mené à l'élaboration d'une nouvelle astronomie. La fréquence de ces ondes est de l'ordre du hertz, mais il existe un intérêt à détecter des ondes de fréquences bien plus grandes, au-delà du mégahertz. Les interféromètres ne sont pas capables détecter d'aussi hautes fréquences. Dans cette thèse, nous allons étudier la détection d'ondes gravitationnelles haute-fréquence en utilisant des champs électromagnétiques, via l'effet Gertsenshtein inverse. Notre détecteur est une cavité électromagnétique cylindrique brevetée [Füzfa, 2018] plongée dans un intense champ magnétique externe. Nous étudions ici la détection de deux sources haute-fréquence qui sont des témoins du début de l'Univers, que sont les trous noirs primordiaux et le fond diffus d'ondes gravitationnelles. Nous allons étudier analytiquement et numériquement la détection de ces signaux, en montrant comment nous pouvons obtenir des informations sur ces objets de l'Univers primordial.

Thèse de doctorat en Sciences Mathématiques (Ph.D. thesis in Mathematics)

Date : 27/01/2023

Département de Mathématique

Promoteur (Advisor) : André FŰZFA

Remerciements

I wanted first to thank all the jury members for accepting the invitation of André and me, and for reading my manuscript carefully. I really enjoyed our discussions during the private defense. Your comments and suggestions helped me to improve the final quality of this thesis.

Je voulais remercier particulièrement Sébastien, qui a aidé André et moi à ouvrir notre recherche à la communauté des trous noirs primordiaux. Cela n'a fait qu'augmenter la visibilité et le nombre de perspectives de notre recherche.

Je voulais également remercier Léonard, avec qui j'ai collaboré pendant son stage à Namur. J'ai beaucoup apprécié travailler avec toi, et te souhaite le meilleur pour ta carrière de scientifique, qui sera sans aucun doute fructueuse.

Enfin, merci André pour tout ce que tu as fait pour moi. Arriver au département de mathématiques pour travailler avec toi a été probablement la meilleure décision de ma jeune carrière. Merci de m'avoir emmené avec toi sur ce sujet passionnant. Merci pour ces discussions tout aussi intéressantes sur notre recherche, sur nos charges de cours, ou sur tout autre sujet. Tu as été un mentor exceptionnel, qui m'a accordé assez de confiance et d'espace pour m'épanouir dans mon parcours doctoral.

Je remercie également tout le département de mathématiques. Ses académiques avec lesquels ce fut toujours plaisant de travailler. Ses secrétaires, Alice et Pascale, qui jouent un rôle crucial dans l'efficacité de ce département. Et enfin mes plus proches collègues et anciens collègues, avec qui chaque jour au bureau pouvait se transformer en succession de moments d'amusement. Je pense entre autres et dans le désordre à mes collègues de bureau Arnaud et Martin qui a la responsabilité reprendre le flam-

beau (pas la série), à Candy, Cédric, Anthony, Riccardo, François, Eve, Eve-Aline, Pauline, Delphine, Martin, Jon, Jojo, Morgane, Watson, Julien, Alexis et Gaëtan. Merci pour tous ces moments et ceux encore à venir quoi qu'il arrive.

Pour Jérémy, le dernier des Mohicans, je n'ai qu'une chose à dire : C'est génial !

Un autre merci tout particulier à Sarah qui a toujours été une oreille attentive pour moi, surtout pendant les moments difficiles du confinement.

Merci également à mes proches en dehors de l'Université. Je pense d'abord à ceux du badminton de Namur, PY, Denis, Godi, JM et Thomas. J'apprécie toujours nos moments passés ensemble. Pensée aussi pour Jerem et Mathilda, Sam, Hélène, Sun, Pascal, Pavel avec qui c'était un plaisir de partager sur les courts et en dehors.

Je pense bien évidemment à mon ami liégeois Max. On ne s'est malheureusement plus beaucoup vu depuis le covid mais c'est un honneur pour moi d'être ton témoin de mariage ! C'est toujours un grand plaisir de partager des moments en ta compagnie !

Je voulais également remercier les amis avec lesquels on a réalisé les 400 coups ces dernières années, dont une croisière mémorable ! Mélissa, merci pour ton accueil toujours chaleureux et pour m'avoir véhiculé plus d'une fois. Tes avis toujours tranchés sont souvent d'une aide précieuse. Merci Romain pour être l'anderlechtois le plus acharné que je connaisse. COYM ! Merci Diandra pour la multitude de moments que l'on a partagés, surtout pendant la période du Covid. Les moments passés avec Romain et toi ont été une bouffée d'oxygène plus que nécessaire et je vous serai toujours reconnaissant pour cela. Merci à Sam et Marjow, c'est toujours un plaisir de découvrir l'Ardenne avec vous. J'ai hâte de voir ce que va donner votre demeure bertrigeoise. Après chaque moment en votre compagnie, je retourne toujours avec le sourire ! Tous les 5, je ne serais pas arrivé où je suis sans votre soutien.

Il me reste à remercier ma famille. Ces moments de recul sur ces dernières années ne peuvent m'empêcher de penser à mes grands-parents. Parrain, Marraine, Mamy Francine, vous me manquez tous les jours de ma vie, mais si je peux écrire ces remerciements dans le cadre d'une thèse de doctorat, c'est sans nul doute grâce à vous aussi ! Et où que vous soyez, je sais que vous êtes fiers de moi.

Merci aussi à ma belle-famille, Jacqueline : un docteur pourra maintenant s'occuper de tes problèmes informatiques. Merci de m'avoir accueilli en tant que futur beau-fils, et d'être aux petits soins avec nous. Merci est un mot bien trop faible pour Axelle et Lénaïc. Merci pour les moments que l'on passe ensemble et qui finissent systématiquement en fous rires. Merci aussi d'être là dans nos petites galères quotidiennes, et aussi dans les plus grandes. Je n'oublierai jamais ce que vous avez fait pour nous durant nos problèmes de logement.

Un merci particulier à ceux qui sont là depuis le début, mes parents. Merci pour l'éducation et les valeurs que vous m'avez transmises, merci pour votre soutien dans tous mes projets, merci pour la confiance et la liberté que vous m'avez toujours accordées. Merci d'être les parents les plus géniaux du monde. Merci aussi d'avoir amené le petit Juju dans notre vie. Plus qu'un frère, c'est aussi un complice, avec qui je partage beaucoup de choses (dont la passion pour les mauves). Je suis fier de l'homme que tu deviens et serai toujours là pour toi !

Enfin, last but not least, il me reste à remercier ma fiancée, Céline. Te rencontrer est la meilleure chose qui me soit arrivée. Merci pour cette complicité au quotidien qui rend tout plus facile. Merci d'avoir amené deux "petits" chats dans ma vie. Merci pour ton soutien indéfectible durant la rédaction de cette thèse. Merci d'être la plus jolie des supportrices d'Anderlecht. Merci d'être toi, tout simplement. Merci pour tout ce que l'on partage et ce que l'on doit encore partager. Je t'aime !

Contents

Introduction

The Universe fascinates people and civilizations around the world for centuries. Humanity always searches to understand where we are, what is around us and what happens beyond the limits of our planet Earth. The scientists developed many ways to observe the celestial sphere, or to observe space from space itself. But on September 14th 2015, another type of astronomy was born. A new type of wave was detected, a gravitational wave. This was made by the LIGO/Virgo collaboration [Abbott et al., 2016] thanks to ground based interferometers. This first detection was groundbreaking in physics. Gravitational waves are a perturbation of the spacetime itself that propagates through the Universe. Their existence was already predicted by Albert Einstein when he elaborate the general relativity [Einstein, 1916b, Einstein, 1918], the physics geometrization theory. Detecting those gravitational waves was a successful test of the general relativity, but also a technical and technological breakthrough. The effect of gravitational waves on test masses will modify the local distance separation between them, and will also modify the optical path of light, but the amplitude of such waves on Earth is extremely faint. The first detection [Abbott et al., 2016] of gravitational waves detected a strain amplitude of 10^{-21} along several kilometers. This is equivalent to measure a displacement of 10^{-18} m, the size of a fraction of an atom nucleus. The first signal detected was the merging of intermediate mass black holes, so this new gravitational wave astronomy can probe objects that does not emit electromagnetic waves, like black holes, turning gravitational wave detectors as a perfect add-on to classical telescopes to understand the Universe phenomena.

Among the pending questions about the Universe, the one questioning its origin and its beginning is not fully answered. Many aspects of these early stages of the Universe demand further understanding about their mechanisms, that happened quickly compared

to the Universe time scale and involved energy scales unreachable today, and could improve the way to access to the grand unification theory of the fundamental interactions. The oldest image of the early Universe is the cosmological microwave background, the first electromagnetic wave emission after the photon decoupling, where the light can finally propagate through the Universe, that became transparent. This event is considered to have occurred about 400 000 years after the beginning of the Universe, so we miss information about those years before photon decoupling. This is where the gravitational waves could be useful. Their propagation is by the way very different than the electromagnetic ones. They exist before photon decoupling, since they can exist as soon as the gravity began to exist. The first gravitational wave emission could be done seconds after the Big Bang [Aggarwal et al., 2021], in a so-called stochastic gravitational wave background, that could contain many information about this early moments of our Universe. In this epoch hard to probe, some compact objects, called primordial black holes could have been formed. Those are tiny black holes formed in this young Universe, but with a different scenario compared to the stellar and supermassive black holes we know. Primordial black holes are what we call a dark matter candidate [Carr et al., 2016], an object that could explain the matter in the Universe that we can not see. In the history of the Universe, primordial black hole binaries could happen and merge like their big brothers detected by LIGO/VIRGO. This merger produces gravitational waves and we can detect them to get information about these early Universe witnesses.

Gravitational waves are in this case a messenger from the early Universe. But these gravitational wave sources emit at quite high frequencies, too high for interferometers. Several techniques are studied to detect those high-frequency gravitational waves. In this thesis, we are going to consider the resonant electromagnetic detection through the so-called Gertsenshtein effect, studied first by Gertsenshtein [Gertsenshtein, 1960] in the 1960s. This effect was studied by several scientists, mostly soviet, until 1980 [Boccaletti et al., 1970, Braginskii and Menskii, 1971, Braginskii et al., 1973, Grishchuk and Sazhin, 1975, Grishchuk, 1977]. After that, most of the scientists working on gravitational waves put their effort in interferometry techniques, with the success we know four decades after. After the first gravitational wave detection, the electromagnetic detection of gravitational waves came back to the spotlight, in order to detect high-frequency gravitational waves and maybe unveil some secrets about the early Universe.

This thesis aims at studying resonant electromagnetic detection inside cylindrical cavities immersed in a strong external magnetic field. After that, we apply our results to the expected detection of high-frequency gravitational wave sources, that contain information about the early Universe.

Chapter 1 consider gravitational waves, by constructing their general theory, before their propagation and generation, in order to focus a bit more on the high-frequency window. There we study different sources, focusing on primordial black hole merger and stochastic gravitational wave background. We end this chapter by questioning the choice of the frame we use to model the detection.

Chapter 2 focus on the link between gravitational waves and electromagnetism. Firstly we construct the Einstein-Maxwell system, which illustrates the minimal coupling between gravitation and electromagnetism in the framework of the general relativity. Secondly, we will consider the direct and inverse Gertsenshtein effect, that can be used for electromagnetic production/detection of gravitational waves. The end of this chapter is a review of the research on the gravitational wave detection with the inverse Gertsenshtein effect.

Chapter 3 will show how we use cylindrical cavities in an external strong magnetic field to detect gravitational waves. After describing the detector, we used some analytical developments to compute the cavity response: the electromagnetic power in the cavity induced by the passing of gravitational waves. To compute that, one must solve wave equations by using spectral methods. We finish this chapter by computing the source term of our wave equations that contains information about the passing gravitational wave.

The final chapter will be dedicated to the numerical simulations of incoming signals detection. We will explain how we build the code to perform that, in order to study how we could detect primordial black hole merger and stochastic gravitational wave background. We end this chapter by the expected sensitivity of our detectors.

Finally, we will draw our conclusions and put some perspectives for further research.

Acknowledgment

This research used resources of the "Plateforme Technologique de Calcul Intensif (PTCI)" (`http://www.ptci.unamur.be`) located at the University of Namur, Belgium, which is supported by the FNRS-FRFC, the Walloon Region, and the University of Namur (Conventions No. 2.5020.11, GEQ U.G006.15, 1610468, RW/GEQ2016 et U.G011.22). The PTCI is member of the "Consortium des Équipements de Calcul Intensif (CÉCI)" (`http://www.ceci-hpc.be`).

Contributions

The thesis leads to the elaboration of two articles.

The first is "Detecting planetary-mass primordial black holes with resonant electromagnetic gravitational-wave detectors", written by Nicolas Herman, André Fűzfa, Léonard Lehoucq, and Sébastien Clesse, published in July 2021 in Physical Review D, volume 104, 023524, referenced as [Herman et al., 2021]

The second is "Electromagnetic Antennas for the Resonant Detection of the Stochastic Gravitational Wave Background" available on arXiv:2203.15668, written by Nicolas Herman, Léonard Lehoucq and André Fűzfa, and submitted to Physical Review D, referenced as [Herman et al., 2022].

In this thesis, the first personal contribution is the review on inverse Gertsenshtein effect detection. No review on this specific topic were made before. This is the section 2.3 of this manuscript. The next contribution is Chapter 3 that described our detector proposal and the analytical development around this. The practical approximation of the source term in the proper detector frame is an innovative contribution. The last contribution is the numerical results presented in Chapter 4 and in the two papers mentioned above. These results pave the way to experimental development of resonant electromagnetic detectors for gravitational waves, a brand new research topic.

The codes used to obtain the numerical results are available on a GitHub repository `http://github.com/nherman95/simHFGW_res_cav/`

Chapter 1

High-Frequency Gravitational Waves

This chapter is a subjective introduction to high-frequency gravitational waves. We first introduce how the gravitational waves are described in the framework of the general relativity theory. Then, we will show which frequency range is covered by the gravitational waves propagating through the Universe, with insisting on the high-frequency window. After that, we will develop some different astrophysical sources that can emit gravitational waves at such high frequencies. These waves are especially interesting here because they could be detected by electromagnetic resonant detectors that we will describe in the next chapter.

1.1 Gravitational waves

Albert Einstein [Einstein, 1916b, Einstein, 1918] predicted the gravitational waves in his general relativity theory. These particular waves are ripples of the spacetime itself, and propagate in the entire Universe at the speed of light. To model those waves, we need to apply perturbation theory to general relativity, to obtain the gravitational wave equation. Considering the propagation in vacuum, we can show that gravitational wave polarization exists. The generation of such gravitational waves occurs quite often in the Universe, through many astrophysical mechanisms and at different frequencies.

1.1.1 General relativity in a nutshell

The general relativity theory can be seen as a geometrization of classical physics and particularly gravitation. From a mathematical point of view, the classical field theory becomes a covariant classical field theory. First imagined by Einstein [Einstein, 1915, Einstein, 1916a], this theory contains some important hypotheses. The first hypothesis is the same as in special relativity, the case where no gravitation is present, it is that the speed of light is constant in vacuum. It is set by convention to $c = 299\,792\,458\ \mathrm{m/s}$. If we add the fact that we want to add a fourth coordinate to describe our spacetime, this leads to the use of pseudo-Euclidean geometry, a four-dimensional space where the norm of vector fields can be either positive, negative or null. Such a space is made to get any causal events trapped in the so-called light cone. In this case, the geometry of spacetime is still flat, but adding gravitation induces curvature, and the use of differential geometry concepts. In this manuscript we use the Einstein summation convention where repeated upper and lower indices are summed over. We use also Greek alphabet indices for values going from 0 to 3 and Latin alphabet indices for values going from 1 to 3.

In the theory of general relativity, we can describe spacetime as a differential manifold. This manifold is a four-dimensional Lorentzian manifold M, associated with a metric tensor $g_{\mu\nu}$. This symmetric tensor solely describes gravitation. The manifold possesses also a connection, generalization of the derivative for curved spaces, compatible with the metric. We assume that our spacetime is torsion-free, so the connection is unique, the so-called Levi-Civita connection

$$g_{\lambda\kappa}\,\Gamma^{\lambda}{}_{\nu\mu} = \frac{1}{2}\left(\partial_\mu g_{\nu\kappa} + \partial_\nu g_{\mu\kappa} - \partial_\kappa g_{\mu\nu}\right). \tag{1.1.1}$$

In this manifold, we can also consider its curvature. This is done by the Riemann tensor $R^{\kappa}{}_{\lambda\mu\nu}$, defined as

$$R^{\kappa}{}_{\lambda\mu\nu} = \partial_\mu \Gamma^{\kappa}{}_{\lambda\nu} - \partial_\nu \Gamma^{\kappa}{}_{\lambda\mu} + \Gamma^{\eta}{}_{\lambda\nu}\Gamma^{\kappa}{}_{\eta\mu} - \Gamma^{\eta}{}_{\lambda\mu}\Gamma^{\kappa}{}_{\eta\nu}. \tag{1.1.2}$$

We can also define two other curvature-related quantities, contractions of the Riemann tensor. Those are the Ricci tensor $R_{\mu\nu} = R^{\lambda}{}_{\mu\lambda\nu}$ and the Ricci scalar $R = R^{\mu}{}_{\mu}$. These are crucial for the mathematical formulation of general relativity, and can be seen as a classical field theory and its master equation can be derived by applying a variational

principle to the so-called Einstein-Hilbert action [Misner et al., 1973, Hobson et al., 2006]

$$S_{E-H} = \frac{c^4}{16\pi G}\int_M R\sqrt{-g}\,d^4x, \tag{1.1.3}$$

where G is Newton's constant and g the determinant of the metric. The variation of this action with respect of a variation of the metric leads to the Einstein equation in vacuum

$$G_{\mu\nu} = 0, \tag{1.1.4}$$

where $G_{\mu\nu} = R_{\mu\nu} - \frac{1}{2}Rg_{\mu\nu}$ is the Einstein tensor, symmetric by construction. If we take the trace of the equation (1.1.4), we find $G = R = 0$. That implies that in this case $G_{\mu\nu} = R_{\mu\nu}$. Equation (1.1.4) has several solutions, that we call vacuum solutions, that are empty Universes. If we want to take into account the content of matter in the Universe, denoted by the Lagrangian density $\mathscr{L}_{mat}$. We thus have to take into account the total action $S_{\rm tot}$ defined by

$$S_{\rm tot} = S_{E-H} + S_{\rm mat} \tag{1.1.5}$$

where $S_{\rm mat} = \int_M \mathscr{L}_{mat}\sqrt{-g}\,d^4x$, is the action of the matter content. The variational principle on this action leads to the famous Einstein equation,

$$G_{\mu\nu} = \frac{8\pi G}{c^4}T_{\mu\nu}, \tag{1.1.6}$$

where $T_{\mu\nu}$ is the energy-momentum tensor, defined by

$$T_{\mu\nu} = -\frac{2}{\sqrt{-g}}\left(\frac{\partial\left(\mathscr{L}_{mat}\sqrt{-g}\right)}{\partial g^{\mu\nu}}\right). \tag{1.1.7}$$

It contains the energy and momentum of the matter. Einstein equation (1.1.6) is a second order partial differential equation and relates the curvature of the spacetime and the mass, or more generally the energy. The divergence of the Einstein tensor is $\nabla_\mu G^{\mu\nu} = 0$ where ∇_μ is the covariant derivative, generalization of the derivative in curved space. This null-divergence is due to Bianchi's identities, that are geometric properties of the Riemann tensor. The right-hand side of equation (1.1.6) is consistent with this null-divergence property because the relation $\nabla_\mu T^{\mu\nu} = 0$ is a consequence of the Noether's theorem and denotes the conservation of energy and momentum in the Universe. The solution of the Einstein equation (1.1.6) is a metric tensor, often

presented as a line element, sort of infinitesimal distance described by

$$ds^2 = g_{\mu\nu} dx^\mu dx^\nu. \tag{1.1.8}$$

General relativity gives a geometrical form to gravitation, and also a covariant way to express it. The fact that this equation is tensorial, implies that this equation keeps the same form when changing the coordinates. The Einstein equation (1.1.6) shows how spacetime is curved depending on its energy content. But we still have no information about the particle dynamics in the spacetime. This is described by the geodesic equation, that we can also obtain using a variational principle. By supposing a curve with parametric equations $x^\mu(\lambda)$ where λ is the parameter of the curve and minimizing the length of the curve $\int_{\lambda_0}^{\lambda_f} \frac{ds}{d\lambda} d\lambda$ with respect to x^μ, we obtain

$$\frac{d^2x^\mu}{d\lambda^2} + \Gamma^\mu{}_{\nu\rho} \frac{dx^\nu}{d\lambda} \frac{dx^\rho}{d\lambda} = 0. \tag{1.1.9}$$

These curves, called geodesics are the generalization of straight lines in a curved spacetime. For massive particles, the λ parameter is given by $d\lambda^2 = c^2 d\tau^2 = -ds^2$ and $x^\mu(\tau)$ represent their trajectory if no external forces are present. The parameter τ describing the curve is known as the proper time. This is the time of any clock carried by the test particle. To denote the trajectory of light or of non-massive particles in the spacetime, the geodesics have zero-length, that is why we call them null-geodesics.

After these few comments and definitions about general relativity, we will show how gravitational waves can exist and propagate in the Universe using this theory.

1.1.2 Linear regime of the General relativity

In general relativity, the solution of the Einstein equation is a metric tensor. In the case of special relativity, the vacuum solution far from any gravitational field, is a flat spacetime denoted by the Minkowski metric ($\eta_{\mu\nu} = \text{diag}(-1,1,1,1)$ in orthonormal coordinates). The gravitational wave theory begins with nearly flat solutions. By considering a perturbed flat metric as solution of the Einstein equation, the metric becomes

$$g_{\mu\nu} = \eta_{\mu\nu} + \bar{h}_{\mu\nu}\ , \tag{1.1.10}$$

where $\bar{h}_{\mu\nu} \ll 1$. In this section, we focus on the leading terms of the different quantities, generally at first order. That is why we call this method the linearization of the Einstein equation. For more information about this theory, see e.g. [Maggiore, 2007, Hobson et al., 2006, Gourgoulhon, 2013]. The first part of the Einstein equation that we want to compute is the Einstein tensor. At first order we find

$$\begin{aligned} G_{\mu\nu} =& \frac{1}{2}\left(\eta^{\lambda\kappa}\left(\partial_\lambda\partial_\mu\bar{h}_{\nu\kappa} + \partial_\lambda\partial_\nu\bar{h}_{\mu\kappa} - \partial_\lambda\partial_\kappa\bar{h}_{\mu\nu}\right) - \partial_\mu\partial_\nu\bar{h}\right) \\ & -\frac{1}{2}\eta^{\alpha\beta}\left(\eta^{\lambda\kappa}\partial_\kappa\partial_\beta\bar{h}_{\alpha\lambda} - \partial_\alpha\partial_\beta\bar{h}\right)\eta_{\mu\nu}. \end{aligned} \tag{1.1.11}$$

We can write this Einstein tensor more compactly by considering the trace-reversed perturbation $h_{\mu\nu} = \bar{h}_{\mu\nu} - \frac{1}{2}\bar{h}\eta_{\mu\nu}$, which leads to

$$G_{\mu\nu} = \frac{1}{2}\left(-\Box h_{\mu\nu} + \partial_\mu V_\nu + \partial_\nu V_\mu - \eta^{\alpha\beta}\partial_\alpha V_\beta \eta_{\mu\nu}\right) \tag{1.1.12}$$

where $V_\alpha = \partial_\kappa\left(\eta^{\lambda\kappa}h_{\alpha\lambda}\right)$. After getting this more compact tensor, where we can already see the wave operator on Minkowski background $\Box = \eta^{\mu\nu}\partial_\nu\partial_\mu$, we can show that this tensor has a gauge invariance. Equation (1.1.12) remains the same with an infinitesimal change of coordinate $y^\mu = x^\mu + \xi^\mu$, where $\xi^\mu \ll 1$. We can show that in this case the trace-reversed perturbation is modified as

$$h'_{\alpha\beta} = h_{\alpha\beta} - \partial_\beta\xi_\alpha - \partial_\alpha\xi_\beta + \eta_{\alpha\beta}\partial_\mu\xi^\mu. \tag{1.1.13}$$

and the V_α field as

$$V'_\alpha = V_\alpha - \Box\xi_\alpha. \tag{1.1.14}$$

By computing the consequences of the infinitesimal change of frame, we can choose the gauge $V_\alpha = 0$ without loss of generality. This choice is called the Lorenz gauge and can be expressed in terms of perturbation as

$$\partial^\mu h_{\mu\alpha} = 0. \tag{1.1.15}$$

Gathering this Lorenz gauge (1.1.15) with equations (1.1.6) and (1.1.12), the lin-

earized Einstein equation can be written in a very simple way,

$$\Box h_{\mu\nu} = -\frac{16\pi G}{c^4} T_{\mu\nu}, \tag{1.1.16}$$

which is a wave equation for the trace-reversed perturbation $h_{\mu\nu}$. The solution of equation (1.1.16) is what we call gravitational waves, and these waves are sourced by the energy momentum tensor. In vacuum, this equation reduces to $\Box h_{\mu\nu} = 0$, which means that these waves can freely propagate through the Universe at the speed of light. Let us now study this case.

1.1.3 Gravitation waves polarization

To detect gravitational waves, we have to study how they behave when they propagate, and also how they interact with test masses. Let us get back to the gravitational wave equation in vacuum

$$\Box h_{\mu\nu} = 0. \tag{1.1.17}$$

We can see in this situation that the Lorenz gauge condition (1.1.15) does not fix the gauge completely. If we take back the equation (1.1.14), any infinitesimal change of coordinates where $\Box \xi_\alpha = 0$ will preserve the Lorenz gauge condition (1.1.15). In order to cancel this gauge freedom, we can fix a change of coordinates ξ_α where $\alpha = 0, \dots, 3$ and $\Box \xi_\alpha = 0$, to impose four conditions on the $h_{\mu\nu}$ tensor. The first one is to fix ξ_0 to get the $h_{\mu\nu}$ traceless. This condition is very useful because we get $h_{\mu\nu} = \bar{h}_{\mu\nu}$. The three other ξ_i are set to make the three spatial-time components vanish $h_{0i} = 0$. This condition associated to the Lorenz gauge (1.1.15) leads to $\partial^0 h_{00} = 0$, meaning that h_{00} must be constant in time. This metric component is related to the Newtonian gravitational potential. Since this component only models the metric perturbation, evolving with time, we can without loss of information set $h_{00} = 0$. This is consistent with the Newtonian physics intuition since we are studying here propagation in vacuum, far from any massive body, so the classical Newtonian potential is null. To sum up these gauge fixing conditions, we can show that our perturbation tensor in this new gauge satisfies

$$h_{0\mu} = 0, \qquad h^{\mu}{}_{\mu} = 0, \qquad \partial^j h_{ij} = 0, \tag{1.1.18}$$

where $\mu = 0,\dots,3$ and $i,j = 1,\dots,3$. This gauge reduces the number of degrees of freedom for our $h_{\mu\nu}$ tensor to only two. This gauge is called the traceless-transverse (TT) gauge.

Now the gauge is totally fixed, the two degrees of freedom left are the polarization modes for the gravitational waves. To describe how we can model this polarization, we can assume for simplicity that our gravitational waves are plane waves along the z-axis $h_{\mu\nu} = A_{\mu\nu}e^{ik_\alpha x^\alpha}$, where $x^\alpha = (ct,x,y,z)$ and $k_\alpha = \left(-\frac{\omega}{c},0,0,k\right)$. Since the gravitational wave is moving at the speed of light, we have the dispersion relation in vacuum $\frac{\omega^2}{c^2} = k^2$. Considering the Lorenz gauge with the plane wave approximation, we can show that the only non-vanishing components of our gravitational wave tensor are

$$\begin{aligned} h^{11} &= -h^{22} = h_+ = A_+ e^{i(kz-\omega t)}, \quad \text{and} \\ h^{12} &= \quad h^{21} = h_\times = A_\times e^{i(kz-\omega t)}. \end{aligned} \tag{1.1.19}$$

These are our two degrees of freedom, the plus (+) polarization and the cross ($\times$) polarization. To understand the name of these modes, we have to describe the effect that each polarization has on test masses. To do so, we have to compute the geodesic deviation, difference between two nearby geodesics. This equation can be found in [Maggiore, 2007] written as

$$\frac{D^2}{D\tau^2}\sigma^\alpha = R^\alpha{}_{\gamma\kappa\beta}\ \ \sigma^\beta \frac{dx^\gamma}{d\tau}\frac{dx^\kappa}{d\tau}. \tag{1.1.20}$$

Here $\frac{D}{D\tau}$ denotes the directional covariant derivative along the tangent vector of the geodesics and σ^α is the deviation vector, denoting the oriented distance between two nearby geodesics. Considering our TT gauge metric perturbation, the equation (1.1.20) becomes [1]

$$\begin{aligned} \frac{d^2}{dt^2}\sigma^1 &= \frac{1}{2}\frac{d^2h_+}{dt^2}\sigma^1 + \frac{1}{2}\frac{d^2h_\times}{dt^2}\sigma^2 \\ \frac{d^2}{dt^2}\sigma^2 &= \frac{1}{2}\frac{d^2h_\times}{dt^2}\sigma^1 - \frac{1}{2}\frac{d^2h_+}{dt^2}\sigma^2. \end{aligned} \tag{1.1.21}$$

We can now consider very small deviations around a fixed deviation, $\sigma^1 = x_0 + \delta x$ and $\sigma^2 = y_0 + \delta y$, to see how tests masses will behave with each polarization. When

(1). We have that $R_{i0j0} = -\frac{1}{2c^2}\ddot{h}_{ij}$

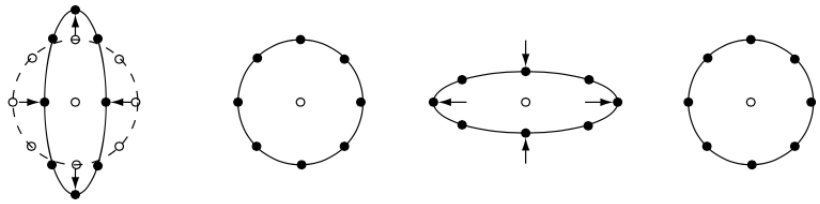

Figure 1.1 – The plus polarized GW action on a ring of test masses (source : [Hobson et al., 2006])

we put $h_\times = 0$, equation (1.1.21) where we keep only dominant terms becomes

$$\frac{d^2}{dt^2}\delta x = -\frac{1}{2}A_+ \, x_0 \, \omega^2 \cos(\omega t),$$
$$\frac{d^2}{dt^2}\delta y = \frac{1}{2}A_+ \, y_0 \, \omega^2 \cos(\omega t),$$

and the solution is

$$\delta x = \frac{1}{2}A_+ \, x_0 \, \cos(\omega t),$$
$$\delta y = -\frac{1}{2}A_+ \, y_0 \, \cos(\omega t).$$

If we consider a ring of test masses, this ring will move in a + shape (figure 1.1), this is why the polarization is called plus. The same analysis can be carried on with $h_+ = 0$ and the solution is

$$\delta x = \frac{1}{2}A_\times \, y_0 \, \cos(\omega t),$$
$$\delta y = \frac{1}{2}A_\times \, x_0 \, \cos(\omega t).$$

If we consider a ring of test masses, the ring will move by forming a cross (figure 1.2), this is why we call it cross polarization.

Please note here that we consider linearly polarized gravitational waves. Here the polarization state does not evolve with time. As for electromagnetic waves, one can consider circular polarization for gravitational waves, where the polarization state is a combination of the two polarization states that evolves with time. Circular gravitational wave polarization is for instance considered in [Kahniashvili et al., 2021].

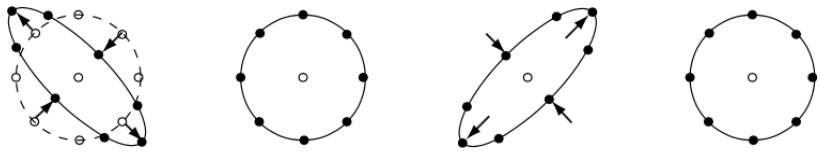

Figure 1.2 – The cross polarized GW action on a ring of test masses (source : [Hobson et al., 2006])

1.2 The High-frequency window

Now we have described the gravitational waves general characteristics, we are going to talk about the different frequencies of gravitational waves we can get from astrophysical sources. After describing how gravitational waves are generated, we focus on high frequency sources, conveniently detected by electromagnetic fields.

1.2.1 Generation of gravitational waves

The first part of this chapter focused on describing the modeling of gravitational waves, their existence and propagation. This section talk about how to get gravitational waveforms from analytical computations. Getting accurate gravitational waveforms is an entire research field by itself (see e.g. [Blanchet, 2014]). Here is a synthesis for a broader physics audience.

As seen in the wave equation (1.1.16), gravitational wave are directly sourced by the energy-momentum tensor. This is a classical wave equation problem and, assuming a totally flat background, the solution outside a gravitational wave source can be found using retarded time functions and more accurately Green function formalism [Maggiore, 2007], which is

$$h_{\mu\nu}(t,\vec{r}) = \frac{4G}{c^4}\int \frac{d\vec{r}'}{|\vec{r}-\vec{r}'|} T_{\mu\nu}\left(t_{ret},\vec{r}'\right) \tag{1.2.1}$$

where $t_{ret} = t - \frac{|\vec{r}-\vec{r}'|}{c}$.

We can also take back this expression to the TT gauge, by using the TT projector $\Lambda_{ij}{}^{kl}$, often called Lambda tensor that makes any h_{kl} tensor transverse and traceless

with the relation $h_{ij}^{TT} = \Lambda_{ij}{}^{kl} h_{kl}$ [2]. If h_{kl} satisfies the Lorenz gauge, the gravitational wave equation (1.1.16) in vaccum can be written as $\Box h_{ij}^{TT} = 0$. This projector can be expressed as in [Maggiore, 2007]

$$\Lambda_{ij}{}^{kl} = \delta_i{}^k \delta_j{}^l - \frac{1}{2}\delta_{ij}\delta^{kl} - n_j n^l \delta_i{}^k - n_i n^k \delta_j{}^l + \frac{1}{2} n^k n^l \delta_{ij} + \frac{1}{2} n_i n_j \delta^{kl} + \frac{1}{2} n_i n_j n^k n^l \tag{1.2.2}$$

where δ_{ij} is the Kronecker symbol and n_i is the constant wave direction of propagation, parallel to the wavevector. Using this projector on equation (1.2.1), we obtain

$$h_{ij}^{TT}(t,\vec{r}) = \frac{4G}{c^4}\Lambda_{ij}{}^{kl} \int \frac{d\vec{r}'}{|\vec{r}-\vec{r}'|} T_{kl}\left(t_{ret},\vec{r}'\right). \tag{1.2.3}$$

The four time-related components of $T_{\mu 0}$ can be eliminated since we can re-express these components in function of T_{kl} using the four conservation laws of the energy-momentum tensor $\partial_\mu T^{\mu\nu} = 0$. As it can be made for electromagnetic wave generation, if the source can be considered as stationary, we can decompose equation (1.2.3) in a multipolar expression

$$h_{ij}^{TT}(t,\vec{r}) = \frac{4G}{rc^4}\Lambda_{ijkl}\left[S^{kl} + \frac{1}{c} n_m \dot{S}^{klm} + \frac{1}{2c^2} n_m n_p \ddot{S}^{klmp} + \dots\right]_{ret}, \tag{1.2.4}$$

where $[\cdot]_{ret}$ denotes that the quantities are taken at $t = t_{ret}$. n_i denotes the unit vector in the $\vec{r}$ direction and the multipolar moments are the ones of the energy-momentum tensor and can be defined as

$$S^{ij}(t) = \int d\vec{r}\, T^{ij}(t,\vec{r}), \tag{1.2.5}$$

$$S^{ijk}(t) = \int d\vec{r}\, x^k T^{ij}(t,\vec{r}), \tag{1.2.6}$$

$$S^{ijkl}(t) = \int d\vec{r}\, x^k x^l T^{ij}(t,\vec{r}). \tag{1.2.7}$$

This multipolar expansion is very powerful but the physical interpretation of these multipole moments is not very straightforward. Fortunately we can express S^{ij} in term of the mass quadrupole M^{ij} defined by

$$M^{ij} = \frac{1}{c^2}\int d\vec{r}\, x^i x^j T^{00}(t,\vec{r}). \tag{1.2.8}$$

(2). We can show that this projector makes any (0,2) tensor transverse and traceless

The temporal derivative of M^{ij} is given by

$$\dot{M}^{ij} = \frac{1}{c}\int d\vec{r}\, x^i x^j\, \partial_{ct} T^{00}(t,\vec{r}). \tag{1.2.9}$$

The energy-momentum tensor conservation implies that $\partial_{ct} T^{00} = -\partial_k T^{0k}$, so by integrating by parts we have

$$\dot{M}^{ij} = \frac{1}{c}\int d\vec{r}\left(x^i\,\partial_k x^j\, T^{0k}(t,\vec{r}) + x^j\,\partial_k x^i\, T^{0k}(t,\vec{r})\right) = \frac{1}{c}\int d\vec{r}\left(x^i\, T^{0j}(t,\vec{r}) + x^j\, T^{0i}(t,\vec{r})\right) \tag{1.2.10}$$

where we use the fact that $\partial_k x^i = \delta^i_k$. Performing another time derivative on the equation above and using the fact that $\partial_{ct} T^{0i} = -\partial_k T^{ki}$ we obtain

$$\ddot{M}^{ij} = \int d\vec{r}\left(T^{ij}(t,\vec{r}) + T^{ji}(t,\vec{r})\right) = 2S_{ij} \tag{1.2.11}$$

where we use the symmetry of the energy momentum tensor. Thus, we can rewrite the leading term of equation (1.2.4) as

$$h^{TT}_{ij}(t,\vec{r}) = \frac{2G}{rc^4}\Lambda_{ijkl}\ \ddot{M}^{kl}(t_{ret}). \tag{1.2.12}$$

This equation is known as the quadrupole formula [Hobson et al., 2006, Maggiore, 2007, Gourgoulhon, 2013]. This formula shows that for a massive system (i.e. when T_{00} dominates, see equation (1.2.8)), it is the mass quadrupole variation that leads to the generation of gravitational waves. If we consider a direction of propagation along the Z-axis of our massive system $n_i = \delta_{i3}$, we can express easily the two polarization states of the gravitational wave sourced by the mass quadrupole,

$$h_+ = \frac{G}{rc^4}(\ddot{M}_{11} - \ddot{M}_{22}), \tag{1.2.13}$$

$$h_\times = \frac{2G}{rc^4}\ddot{M}_{12}. \tag{1.2.14}$$

A common example of mass quadrupole variation is binary systems. In a more general way, one can observe gravitational waves coming from an arbitrary direction given by $n_i = (\sin\theta\sin\phi, \sin\theta\cos\phi, \cos\theta)$, where θ is the angle between $\vec{n}$ and the Z-axis, and ϕ is the angle between the orthogonal projection of $\vec{n}$ on the X-Y plane and the Y-axis (see figure 1.3). For instance, applying this formula to the inspiral phase of a compact binary system with circular orbit [Maggiore, 2007], we find that we can express the

mass quadrupole as $M^{ij} = \mu x^i x^j$ where $\mu = \frac{m_1 m_2}{m_1+m_2}$ is the reduced mass, and $m_{1,2}$ are the mass of the two compact bodies of the binary system. In a fixed circular orbit, we can assume that the motion is in the X-Y plane so the orbit is given by

$$x(t) = R\cos(\omega_s t + \frac{\pi}{2}) \quad (1.2.15)$$

$$y(t) = R\sin(\omega_s t + \frac{\pi}{2}) \quad (1.2.16)$$

$$z(t) = 0, \quad (1.2.17)$$

where ω_s is the angular velocity and the choice of the phase $\frac{\pi}{2}$ is useful for the origin of t. We can show that

$$\ddot{M}_{11} = -\ddot{M}_{22} = 2\mu R^2 \omega_s^2 \cos(2\omega_s t), \quad (1.2.18)$$

$$\ddot{M}_{12} = 2\mu R^2 \omega_s^2 \sin(2\omega_s t). \quad (1.2.19)$$

Thus, the gravitational waveform is

$$h_+(t) = \frac{4G\mu\omega_s^2 R^2}{c^4 r}\left(\frac{1+\cos^2\theta}{2}\right)\cos[2\omega_s t_{ret} + 2\phi], \quad (1.2.20)$$

$$h_\times(t) = \frac{4G\mu\omega_s^2 R^2}{c^4 r}\cos\theta\sin[2\omega_s t_{ret} + 2\phi] \quad (1.2.21)$$

where we find the angles θ and ϕ coming through vector n_i. We can see that the frequency of the produced gravitation wave is $\omega_{gw} = 2\omega_s$ and we can then express the angular velocity ω_s thanks to the third Kepler law $\omega_s^2 = \frac{G(m_1+m_2)}{R^3}$. We can thus rewrite the equations above as

$$h_+(t) = \frac{4}{r}\left(\frac{GM_c}{c^2}\right)^{5/3}\left(\frac{\omega_{GW}}{2c}\right)^{2/3}\left(\frac{1+\cos^2\theta}{2}\right)\cos[\omega_{gw} t_{ret} + 2\phi], \quad (1.2.22)$$

$$h_\times(t) = \frac{4}{r}\left(\frac{GM_c}{c^2}\right)^{5/3}\left(\frac{\omega_{GW}}{2c}\right)^{2/3}\cos\theta\sin[\omega_{gw} t_{ret} + 2\phi], \quad (1.2.23)$$

where $M_c = \frac{(m_1 m_2)^{3/5}}{(m_1+m_2)^{1/5}}$ is the chirp mass, useful quantity to study binary systems. Until now we assumed that the orbit is fixed. But when such a system produces gravitational waves, the energy of the system decreases, the distance between the compact object also decreases and the frequency evolves with time. By equating the emitted power of gravitational waves and the variation of the orbital energy with time, one can find

in [Maggiore, 2007] that

$$\dot{\omega}_{gw} = \frac{12}{5} 2^{1/3} \left(\frac{GM_c}{c^3} \right)^{5/3} \omega_{gw}^{11/3}. \tag{1.2.24}$$

Maggiore proposes to rewrite equations (1.2.22) and (1.2.23) by using the function

$$\phi(t) = \int_{t_0}^{t} dt' \omega_{gw}(t'), \tag{1.2.25}$$

whre t_0 is the initial time. The final waveform for a compact binary system with a circular orbit is

$$h_+(t) = \frac{1}{r} \left(\frac{GM_c}{c^2} \right)^{5/4} \left(\frac{5}{c\tau} \right)^{1/4} \left(\frac{1+\cos^2\theta}{2} \right) \cos\left[\phi(\tau)\right], \tag{1.2.26}$$

$$h_\times(t) = \frac{1}{r} \left(\frac{GM_c}{c^2} \right)^{5/4} \left(\frac{5}{c\tau} \right)^{1/4} \cos\theta \sin\left[\phi(\tau)\right], \tag{1.2.27}$$

where we can compute that

$$\phi(\tau) = -2 \left(\frac{5GM_c}{c^3} \right)^{-5/8} \tau^{5/8} + \phi_0, \tag{1.2.28}$$

with ϕ_0 an integration constant and $\tau = t^{\text{coal}} - t = t_{ret}^{\text{coal}} - t_{ret}$. The quantities t^{coal} and t_{ret}^{coal} are the time of the coalescence, the fusion between the two compact objects, respectively in the observer's time and retarded time. A schematic representation of this waveform is given in figure 1.4

If we want to look at the frequency content of these waves, we can perform the temporal Fourier transform of the waveform, $h_+(t) = A(t_{ret})\cos(\phi(t_{ret}))$ and we get

$$\tilde{h}_+(\omega) = \frac{e^{i\frac{\omega r}{c}}}{2} \int A(t_{ret}) \left(e^{i\phi(t_{ret})} + e^{-i\phi(t_{ret})} \right) e^{i\omega t_{ret}} dt_{ret}. \tag{1.2.29}$$

Maggiore computed this integral using the stationary phase method, considering the limit of the integrand above when t_{ret} goes to infinity. Thus the term in $e^{i\phi(t_{ret})}$ is always oscillating fast and becomes negligible in the integral and we have a fixed phase point at t^* when $\dot{\phi}(t^*) = \omega$. Considering that $A(t_{ret}) = A(t^*)$ and expanding the

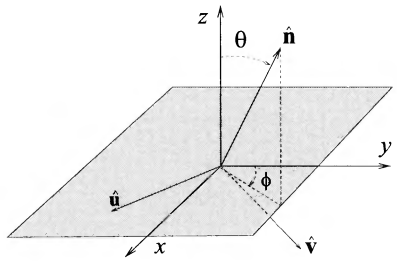

Figure 1.3 – Representation of the direction of the gravitational wave propagation $\vec{n}$ along an arbitrary direction and the reference frame in Cartesian coordinates (x,y,z), the vectors $\vec{u}$ and $\vec{v}$ are the transverse directions of the wave (source : [Maggiore, 2007]).

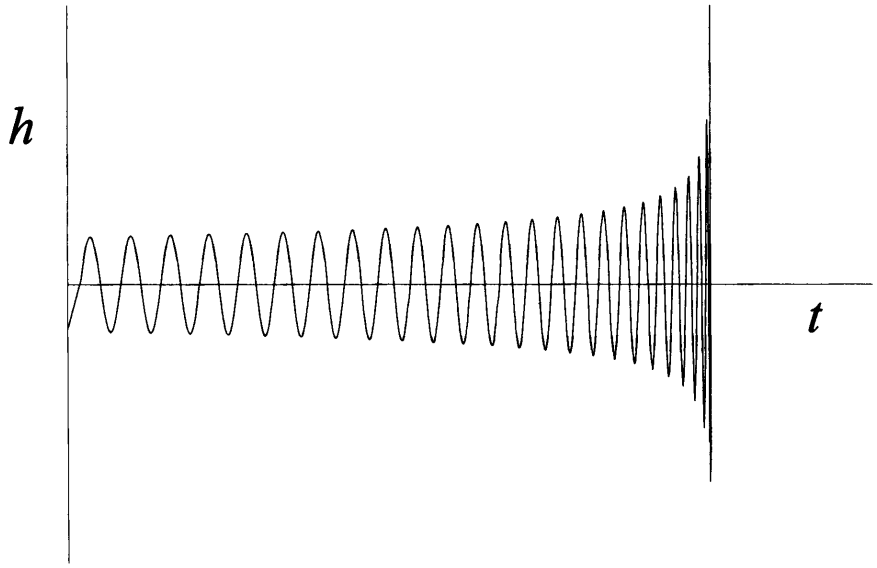

Figure 1.4 – Schematic curve of the waveform from the inspiral phase of compact binary systems (source : [Maggiore, 2007]).

terms in a Taylor series around t^* to the second order, we find that

$$\tilde{h}_+(\omega) = \frac{e^{i\psi_+(\omega)}}{2} A(t^*) \sqrt{\frac{2\pi}{\ddot{\phi}(t^*)}} \tag{1.2.30}$$

where $\psi_+(\omega)$ is a linear function of ω. By replacing the functions A and ϕ by their expressions we find that

$$\tilde{h}_+(\omega) = C e^{i\psi_+(\omega)} \frac{c}{r} \left(\frac{GM_c}{c^3}\right)^{5/6} \left(\frac{\omega}{2\pi}\right)^{-7/6} \left(\frac{1+\cos^2\theta}{2}\right). \tag{1.2.31}$$

where $C = \pi^{-2/3}\sqrt{\frac{5}{24}}$ is a constant. In the same way we obtain the expression for the $\times$ polarization

$$\tilde{h}_\times(\omega) = C e^{i\psi_\times(\omega)} \frac{c}{r} \left(\frac{GM_c}{c^3}\right)^{5/6} \left(\frac{\omega}{2\pi}\right)^{-7/6} \cos\theta \tag{1.2.32}$$

where $\psi_\times$ is a linear function of ω. The equations (1.2.31) and (1.2.32) above provide us a first waveform to roughly understand the properties of the generated waves, but we made also a huge hypothesis: we must have a flat background, so it will be useful only in non-relativistic case.

We need something that takes into account the relativistic effects, on a possible non-flat background, we therefore use post-Newtonian approximations. To understand how these methods works we need to define another field [Maggiore, 2007, Blanchet, 1987, Blanchet and Damour, 1989, Blanchet, 2014]

$$\mathfrak{h}^{\mu\nu} = (-g)^{1/2} g^{\mu\nu} - \eta^{\mu\nu}, \tag{1.2.33}$$

slightly different from the definition of the metric perturbation (1.1.10). Here we do not assume any order of the perturbation to truncate the expression of the metric. With the quantity defined in equation (1.2.33), we consider the non-perturbative component of the metric in a exact way. However, if we restrict ourselves to the first order of the metric perturbation, one can easily show that $\mathfrak{h}^{\mu\nu} = -h^{\mu\nu}$. The difference between the two quantities will show up when we will consider the Einstein Equation for $\mathfrak{h}^{\mu\nu}$. If we impose the de Donder gauge $\partial_\mu \mathfrak{h}^{\mu\nu} = 0$, we obtain the so-called relaxed Einstein

equation [Blanchet, 2014]

$$\Box \mathrm{h}^{\mu\nu} = \frac{16\pi G}{c^4}\mathrm{t}^{\mu\nu}. \tag{1.2.34}$$

This equation seems very similar to the gravitational wave equation described earlier (1.1.16), but the right hand side of the equation is quite different, its expression is

$$\mathrm{t}^{\mu\nu} = (-g)\,(T^{\mu\nu} + t^{\mu\nu}) + \partial_\alpha\partial_\beta\chi^{\mu\nu\alpha\beta}, \tag{1.2.35}$$

where we identify the energy-momentum tensor contribution, and two others. The first is the Landau-Lifshitz pseudo-tensor [3] $t^{\mu\nu}$, which can be expressed by

$$\begin{aligned}(-g)t^{\mu\nu} = \frac{c^4}{16\pi G}\Big[&g_{\lambda\alpha}g^{\beta\rho}\partial_\beta \mathrm{h}^{\mu\lambda}\partial_\rho \mathrm{h}^{\nu\alpha} + \frac{1}{2}g_{\lambda\alpha}g^{\mu\nu}\partial_\rho \mathrm{h}^{\lambda\beta}\partial_\beta \mathrm{h}^{\rho\alpha} \\ &- g_{\alpha\beta}\left(g^{\lambda\mu}\partial_\rho \mathrm{h}^{\nu\beta} + g^{\lambda\nu}\partial_\rho \mathrm{h}^{\mu\beta}\right)\partial_\lambda \mathrm{h}^{\rho\alpha} \\ &+ \frac{1}{8}(2g^{\mu\lambda}g^{\nu\alpha} - g^{\mu\nu}g^{\lambda\alpha})(2g_{\beta\rho}g_{\sigma\tau} - g_{\rho\sigma}g_{\beta\tau})\partial_\lambda \mathrm{h}^{\beta\tau}\partial_\alpha \mathrm{h}^{\rho\sigma}\Big],\end{aligned} \tag{1.2.36}$$

and the second new contribution is the $\chi^{\mu\nu\alpha\beta}$ tensor defined by

$$\chi^{\mu\nu\alpha\beta} = \frac{c^4}{16\pi G}\left(\mathrm{h}^{\mu\alpha}\mathrm{h}^{\nu\beta} - \mathrm{h}^{\alpha\beta}\mathrm{h}^{\mu\nu}\right). \tag{1.2.37}$$

With these expressions we can notice that in the relaxed Einstein equation (1.2.34), the quantity $\mathrm{h}^{\mu\nu}$ is sourced by the energy-momentum tensor, but also from non-linear functions of the metric and $\mathrm{h}^{\mu\nu}$ itself. These kind of equations are the very basis of the so-called post-Newtonian expansion, developed in the 1990s by Blanchet and Damour [Blanchet, 1987, Blanchet and Damour, 1989, Blanchet, 2014]. Their way to solve (1.2.34) is to consider the non-flat metric outside of the source as a series expansion of the Newton's constant G. If we restrict ourselves to the first order we have

$$\mathrm{h}^{\mu\nu} = G\mathrm{h}^{\mu\nu}_{(1)} + \mathscr{O}(G^2). \tag{1.2.38}$$

In this case, in vacuum, the relaxed Einstein equation becomes

$$\Box \mathrm{h}^{\mu\nu}_{(1)} = 0, \tag{1.2.39}$$

(3). $t^{\mu\nu}$ is a pseudo-tensor because the laws of conservation of this tensor is made with partial derivatives instead of covariant ones.

where we have the gauge condition $\partial_\nu \mathsf{h}^{\mu\nu}_{(1)} = 0$. Blanchet and Damour found a complete analytical solution for this problem [Blanchet, 2014]. They consider after a series expansion of $\mathsf{h}^{\mu\nu}$ in terms of G powers,

$$\mathsf{h}^{\mu\nu} = \sum_{n=1}^{+\infty} G^n \, \mathsf{h}^{\mu\nu}_{(n)}, \tag{1.2.40}$$

where each $\mathsf{h}^{\mu\nu}_{(n)}$ has the dimension of G^{-n}. The wave equations for the first terms of the expansion become

$$\begin{aligned}
\Box \mathsf{h}^{\mu\nu}_{(2)} &= N^{\mu\nu}\left(\mathsf{h}_{(1)}, \mathsf{h}_{(1)}\right), && (1.2.41)\\
\Box \mathsf{h}^{\mu\nu}_{(3)} &= M^{\mu\nu}\left(\mathsf{h}_{(1)}, \mathsf{h}_{(1)}, \mathsf{h}_{(1)}\right) + N^{\mu\nu}\left(\mathsf{h}_{(1)}, \mathsf{h}_{(2)}\right) + N^{\mu\nu}\left(\mathsf{h}_{(2)}, \mathsf{h}_{(1)}\right), && (1.2.42)\\
\Box \mathsf{h}^{\mu\nu}_{(4)} &= L^{\mu\nu}\left(\mathsf{h}_{(1)}, \mathsf{h}_{(1)}, \mathsf{h}_{(1)}, \mathsf{h}_{(1)}\right)\\
&\quad + M^{\mu\nu}\left(\mathsf{h}_{(1)}, \mathsf{h}_{(1)}, \mathsf{h}_{(2)}\right) + M^{\mu\nu}\left(\mathsf{h}_{(1)}, \mathsf{h}_{(2)}, \mathsf{h}_{(1)}\right) + M^{\mu\nu}\left(\mathsf{h}_{(2)}, \mathsf{h}_{(1)}, \mathsf{h}_{(1)}\right)\\
&\quad + N^{\mu\nu}\left(\mathsf{h}_{(2)}, \mathsf{h}_{(2)}\right) + N^{\mu\nu}\left(\mathsf{h}_{(1)}, \mathsf{h}_{(3)}\right) + N^{\mu\nu}\left(\mathsf{h}_{(3)}, \mathsf{h}_{(1)}\right), && (1.2.43)\\
&\vdots
\end{aligned}$$

where the functions $L^{\mu\nu}$, $M^{\mu\nu}$ and $N^{\mu\nu}$ can be computed straightforwardly [Blanchet, 2014] by expanding the relaxed Einstein equation (1.2.34). We can thus conclude that at every order the wave equation and the gauge condition are

$$\begin{aligned}
\Box \mathsf{h}^{\mu\nu}_{(n)} &= \Lambda^{\mu\nu}_{(n)}\left(\mathsf{h}_{(1)}, \mathsf{h}_{(2)}, \ldots, \mathsf{h}_{(n-1)}\right), && (1.2.44)\\
\partial_\mu \mathsf{h}^{\alpha\mu}_{(n)} &= 0. && (1.2.45)
\end{aligned}$$

That means that every order n is sourced by the $(n-1)$ previous orders, denoted by the functions $\Lambda_{(n)}$. The main result of Blanchet and Damour is that all the wave equations can be solved by getting, as all linear differential equations, their homogeneous and non-homogeneous part such as

$$\mathsf{h}^{\mu\nu}_{(n)} = u^{\mu\nu}_{(n)} + v^{\mu\nu}_{(n)}, \tag{1.2.46}$$

where $u^{\mu\nu}_{(n)}$ in a particular solution part and $v^{\mu\nu}_{(n)}$ a homogeneous one to preserve the de Donder gauge condition (1.2.45). They provide analytical solutions [Blanchet, 2014] to these equations and applied to the inspiral phase of binary compact objects

with all the terms until G^4. It helps to provide tools to implement physical and accurate waveforms for gravitational wave research, when the size of the source is bigger than the considered Schwarzschild radius and for sufficiently small velocities. This is why we need numerical relativity techniques near the merger for compact binaries. Their work was implemented in the LIGO software packages, the LALsuite software [LIGO Scientific Collaboration, 2018]. For instance, the functions `SimInspiralChooseWaveformTD` and `SimInspiralChooseWaveformFD` generates post-newtonian waveforms coming from binary inspiralling phase respectively in the time domain and the frequency domain, which will be useful to model detection processes. More details about the waveform generation implementation can be found in [Buonanno et al., 2009].

1.2.2 Current situation on gravitational wave detection

After the first detection of gravitational waves by the LIGO and Virgo Scientific Collaboration [Abbott et al., 2016], research interest on gravitational wave physics increased a lot over the last years. The two main topics about gravitational wave research is improving detection techniques and sources modeling. About detection techniques, scientists mostly focus on interferometry techniques (ground-based or space-based), the only way to detect them currently. Their principle relies on the local modification of the optical path when the gravitational wave passes. The first detection of gravitational waves on September 14th 2015 using ground-based interferometers results from the merging of two black holes, one of 36 $M_\odot$, and the second one 29 $M_\odot$[Abbott et al., 2016]. The signal lasted 0.2 second and its frequency range was between 35 and 150 Hz. 90 [LIGO Scientific Collaboration, 2022] events were detected since this first detection, all were compact binaries signals. At this range of frequency, we can also detect merging pulsars. The scientific gravitational wave community also plans to build a space-based detector, LISA [Amaro-Seoane et al., 2012], it will look at frequencies around the mHz band, to detect massive binaries or some extreme mass ratio binary inspirals. Please note that the building of next generation ground-based interferometers is already planned, with the Einstein Telescope project [ET steering committee, 2020].

The second detection process in progress is pulsar timing array. This method consists of using emission of millisecond pulsars as interferometers. The passing of a gravitational wave will slightly modify the pulse time of arrivals and could be detected

by radio telescopes. As mentioned in [Maiorano et al., 2021], the frequency range at which pulsar timing array is sensitive depends on the duration of the observation run and the periodicity of those runs. Currently, observations campaign is thirteen year long, and performed once a week. This leads to a sensitivity in the nHz to mHz frequency range, useful to detect the most massive compact objects in the Universe, millions of solar masses bodies. This technique could potentially detect a stochastic gravitational wave background at very-low frequency, carrying information about the early universe with a significant contribution of supermassive compact objects. The International Pulsar Timing Array (IPTA) consortium is currently observing gravitational waves at nanohertz frequencies. They published two data releases [Verbiest et al., 2016, Antoniadis et al., 2022] for analysis and as mentioned this year in [Antoniadis et al., 2022], even they can not claim the presence of a stochastic background, they provide several hints to keep digging in this way.

All this information can be summarized in Fig.1.5. This figure was provided by a web tool called GW Plotter [Moore et al., 2015], that can reproduce some expected gravitational wave content of astronomical sources and compare them with sensitivity curves. From what was explained above and the figure, we must notice that there is few interest of the scientific community on gravitational waves at high frequencies (above kHz).

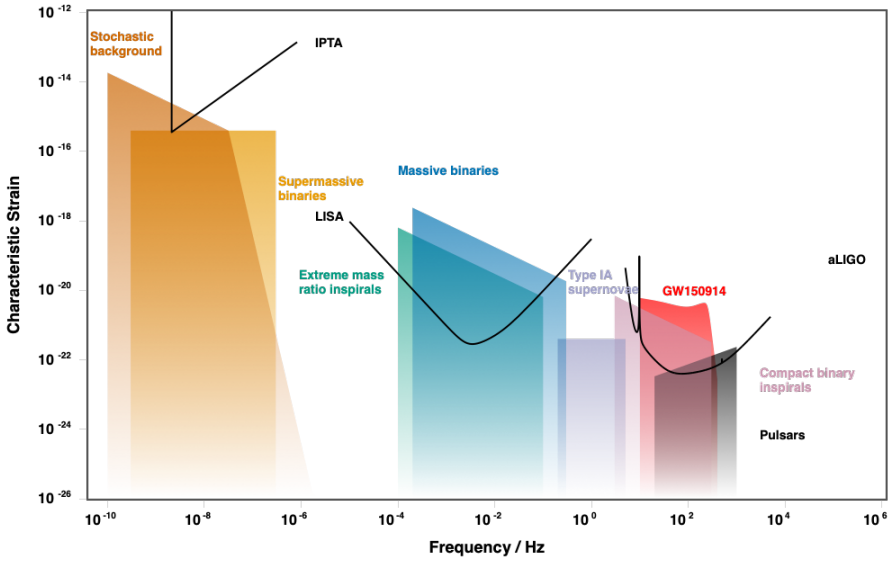

Figure 1.5 – Representation of Gravitational Waves sources with their estimated parameters and sensitivity curves of several detectors. Note that there is not much interest on what happen above the kHz, illustrating the interest of most of the gravitational wave research community. Figure generated by the online tool GW Plotter [Moore et al., 2015]

This is why the Ultra-High-Frequency Gravitational Wave (UHF-GW) [UHF-GW community, 2022] initiative was created in 2019. This group gathers tens of people working on source modeling, detector proposals and experimental feasibility of high-frequency gravitational wave detection. One of the main challenges in this field is that interferometry techniques are not suited for this frequency range. As mentioned in the review of the UHF-GW initiative [Aggarwal et al., 2021], despite several proposals aiming at extending the sensitivity of interferometers to high-frequency (up to 100 MHz), the quantum shot noise will be extremely challenging to overcome, until making any detection impossible above 1 GHz. The other reason that UHF-GW has few interest from the scientific community is that we do not know for now any astrophysical object that can emit gravitational wave at a significant amplitude. On one hand it is a pity because we are not sure if there are gravitational waves at these frequencies but on the other hand if we are able to detect gravitational waves at such high frequencies, this potential detection will reinforce the need of a novel physics to model these objects, or maybe verify some models about cosmology or the early Universe physics. Let us now discuss in a synthetic way the hypothetical sources for high-frequency detection.

1.2.3 Sources of high-frequency gravitational waves

In the review [Aggarwal et al., 2021], two main categories of high frequency gravitational wave sources are considered. This section will present possible sources, insisting on how characterize them.

The first main category of sources are coherent sources coming from the late Universe. They consist mainly of binary systems made of neutron stars, sub-solar primordial black holes or other exotic compact objects such as gravitino stars, Q-balls, boson stars, gravastars or oscillons. Another possible source is the emission of gravitational waves from clouds of axions created by the superradiance [(4)] of black holes [Brito et al., 2015]. To characterize these kinds of sources, since the frequency content of the gravitational wave coming from inspiral binaries is evolving with time, we use a stationary phase approximation, in order to get the analytical Fourier transform of our

(4). These are amplified electromagnetic emission of black holes due to the dissipation of a non-spherical bosonic cloud near the horizon.

signal $\tilde{h}(\omega)$. We can thus define the characteristic strain, adimensional quantity, as

$$h_{c,coh} = \frac{\omega}{\pi}\tilde{h}(\omega). \tag{1.2.47}$$

This quantity is helpful to compare stochastic and coherent sources, but also to compare to sensitivity curves such as Fig.1.5.

Among these coherent sources of the late Universe, we will mostly focus on one specific source, light primordial black hole mergers, which are a candidate to explain at least a part of the dark matter. Detecting black holes that weigh less than the Sun is interesting because it will point automatically to a primordial origin since there exists no possible late Universe scenario of sub-solar black hole formation. Even if these primordial black hole mergers are considered here as late universe sources, the formation of such individual black holes happened obviously in the early stages of the Universe.

As mentioned above in this chapter, the frequency of the gravitational waveform evolves with time, because of the energy loss of the compact binary system due to emission of gravitational waves. This effect was highlighted by the first discovery of a binary pulsar by Hulse and Taylor [Hulse and Taylor, 1975, Taylor and Weisberg, 1982]. The energy loss will get the two bodies closer to each other, until the binary system reaches the innermost stable circular orbit (ISCO), before entering in coalescence. The related gravitational wave frequency at ISCO for a binary system of masses m_1 et m_2 is given by

$$f_{\rm ISCO} = \frac{4400\,{\rm Hz}}{(m_1+m_2)/M_\odot}\ . \tag{1.2.48}$$

This frequency is the limit where we can use post-newtonian methods to get accurate waveforms for compact binary mergers. For instance, a frequency of 220 MHz thus corresponds to a primordial black hole merger of two $10^{-5}M_\odot$ bodies, the same order than the mass of the lenses at the origin of the microlensing events reported in [Niikura et al., 2019]. Nevertheless, for being an interesting gravitational wave signal, one needs to investigate if the merging rate of such black holes can lead to at least $\mathcal{O}(1)$ mergers per year within our detector range. In order to analyze this merging rate, we consider two primordial black holes merging scenarios; the first one is a simple

binary system and the second one is merging of primordial black holes in a cluster of them. This question was investigated in [Herman et al., 2021] where the following results were brought mostly by Sébastien Clesse. For more details about the formation and merging rates, one can read [Aggarwal et al., 2021, Herman et al., 2021]. Those results are in line with recently published papers [Domcke et al., 2022, Franciolini et al., 2022].

If primordial black holes are spatially randomly distributed at formation, it happens that two form so close to each other that their gravitational attraction overpasses the effect of the Hubble-Lemaître expansion at some point before the photon decoupling epoch. In such a case, they directly form a binary whose orbital parameters and lifetime do not only depend on the two black hole masses but also on the mass and distance of the nearest primordial black holes. Eventually, it takes of the order of the age of the Universe for the primordial black hole binary to merge. If one considers the merging rates of equal-mass binaries that produce the largest strain signal, the merging rates with respect to the mass can be approximated by

$$R^{\rm prim}(m_{\rm PBH}) \approx \frac{3.1\times10^6}{\rm Gpc^3\,yr}\tilde{f}^2_{\rm PBH}\left(\frac{m_{\rm PBH}}{M_\odot}\right)^{-0.86}. \tag{1.2.49}$$

where we define an effective parameter

$$\tilde{f}_{\rm PBH}(m_{\rm PBH}) \equiv f_{\rm PBH} f(m_{\rm PBH}) f_{\rm sup}^{1/2} \tag{1.2.50}$$

where $f(m)$ is the today density distribution of PBHs normalized to one ($\int f(m)\mathrm{d}\ln m = 1$) and $f_{\rm PBH}$ is the integrated DM fraction made of PBHs, and includes a rate suppression factor $f_{\rm sup}$ to take into account the possible rate suppression due to binary disruption by early-forming clusters.

In turn, one can determine the radius of the sphere in which one expects one event per year,

$$D_1^{\rm prim} = \left(\frac{4\pi}{3}R^{\rm prim}\right)^{-1/3} \approx 4.2\,{\rm Mpc}\times\tilde{f}_{\rm PBH}^{-2/3}\left(\frac{m_{\rm PBH}}{M_\odot}\right)^{0.29}. \tag{1.2.51}$$

For simplicity we neglected the effects of redshift that are anyway insignificant for most of the considered cases.

The second binary formation channel is through dynamical capture in dense primordial black hole halos. Like any other dark matter candidate, primordial black holes are expected to form halos during the cosmic history, and their clustering properties determine the overall merging rate. We can obtain the merging rate approximation for equal-mass binaries,

$$R^{\rm clus}(m_{\rm PBH}) = 1.2 \times 10^3 \, \tilde{f}^2_{\rm PBH} \, , \tag{1.2.52}$$

and the corresponding source distance $D_1^{\rm capt}$,

$$D_1^{\rm clus} \approx 58\,{\rm Mpc} \times \tilde{f}^{-2/3}_{\rm PBH} . \tag{1.2.53}$$

These equations will show us how a detector must be sensitive to primordial black hole mergers in order to be matched with microlensing observations about the primordial black hole abundance.

The other type of sources considered in the review [Aggarwal et al., 2021] are stochastic sources. As the Cosmological Microwave Background (CMB), the gravitational waves produced at the early stages of the Universe could constitute a stochastic gravitational wave background, produced by cosmological sources at cosmological distances. The most interesting in probing such a signal is that unlike the CMB, the stochastic gravitational wave backgrounds can give information before the photon decoupling epoch, and can "go back in time" up to the grand unification scale, involving physics at very high energy levels that we never met before. The review [Aggarwal et al., 2021] indicates that the existence of a stochastic background in the high-frequency window is well-motivated. The causality put limits on the wavelength of the possible gravitational wave emission. The wavelength must be smaller than the length of the cosmological horizon at the time of production, and GHz frequencies is related to the horizon of high energy physics theory, such the Grand Unification Theory (GUT) scale. Detecting a stochastic gravitational wave background would be a tremendous breaktrough to the understanding of the early Universe physics.

Maggiore [Maggiore, 2007] described first the stochastic gravitational wave background as isotropic, Gaussian and stationary, and its frequency dependence is contained in a one-sided power spectral density. The Gaussian characteristic means that a correlation of N measurements can be reduced to sum and products of two measurements correlation. It is related to the central limit theorem. The stationary property

means that a correlation between two measurements can depend only on time differences and not absolute values. In Fourier space that means that the correlation in Fourier space $\langle \tilde{h}(\omega)\tilde{h}^*(\omega')\rangle$ must be proportional to the Dirac delta $\delta(\omega-\omega')$. Mathematically, this could be summarized as

$$\langle \tilde{h}_A(\omega,\Upsilon)\tilde{h}^*_{A'}(\omega',\Upsilon')\rangle = \frac{1}{2}\delta^2(\Upsilon,\Upsilon')\delta_{AA'}\delta(\omega-\omega')S_h(\omega). \tag{1.2.54}$$

where A and A' are the considered polarization states, and Υ and Υ' are the solid angles determining the detection direction.

The function $S_h(\omega)$ is the one-sided power spectral density that contains the frequency distribution of the signal. The term one-sided is because we only consider positive ω values. The left-hand side of this equation can be seen as a power spectral density when the signal has the same polarization A, the same wavenumber content ω and observed on the same solid angle Υ. With these assumption we obtain

$$|\tilde{h}_+(\omega)|^2 = \frac{S_h\left(\frac{\omega}{2\pi}\right)}{2}. \tag{1.2.55}$$

Due to the Wiener-Khintchine theorem [Wiener, 1930, Khintchine, 1934], this power spectral density is equivalent to the Fourier transform of the autocorrelation function of the signal, which can be used to correlate data coming from several detections.

In the review [Aggarwal et al., 2021], a variety of possible sources of stochastic background are considered, which mostly arises from hypothetical physics of the early universe : (pre)heating, oscillons, cosmic strings, inflation, to name but a few. Most of these hypothetical sources can be characterized by two parameters. The first one is the energy density per logarithmic frequency sampling, constant in some models and defined by

$$\Omega_{\rm GW} = \frac{1}{\rho_{c,0}}\frac{\partial \rho_{\rm GW}}{\partial \ln \frac{\omega}{2\pi}}, \tag{1.2.56}$$

where $\rho_{\rm GW}$ is the energy density of gravitational waves and $\rho_{c,0} = \frac{3H_0^2}{8\pi G}$ is the critical energy density of today where H_0 is the Hubble parameter of today. The second property that we could focus on is that most of the potential sources have a cut-off frequency in the MHz-GHz band. This is due to the waves trapped in the horizon at the epoch of the end of the inflation in the early Universe [Maggiore, 2018]. This cut-

off could also be related to the GUT scale as mentioned above. The equation (1.2.54) can be rewritten to consider the new quantity $\Omega_{\rm GW}$ which leads to

$$\langle \tilde{h}_A(\omega,\Upsilon)\tilde{h}^*_{A'}(\omega',\Upsilon')\rangle = \frac{3H_0^2}{8\pi^2}\Omega_{\rm GW}(\omega)\left(\frac{\omega}{2\pi}\right)^{-3}\delta^2(\Upsilon,\Upsilon')\delta_{AA'}\delta(\omega-\omega'). \quad (1.2.57)$$

We can thus rewrite the parameter $\Omega_{\rm GW}$ as

$$\Omega_{\rm GW} = \frac{1}{3H_0^2}\omega^2 h^2_{c,\rm sto}(\omega), \quad (1.2.58)$$

where $h_{c,\rm sto}$ is the characteristic strain (still dimensionless) defined by

$$h_{c,\rm sto} = \sqrt{\frac{\omega}{2\pi}S_h(\omega)}. \quad (1.2.59)$$

This characteristic strain for stochastic sources will be very useful to compare with coherent sources or sensitivity curves of detector. The characteristic strain is commonly used in the gravitational wave detection community.

In this section we studied two potential sources of high-frequency gravitational waves, primordial black hole merger and stochastic gravitational wave background. The latter can come from many different phenomena, and one of them is the stochastic background coming from primordial black holes (see e.g. [Franciolini et al., 2022]). In this manuscript, we do not focus on one specific model of stochastic background. We study in Chapter 4 a toy model for the stochastic background, to show that our detector proposal described in Chapter 3 can handle stochastic sources.

1.3 The choice of the frame

In the previous sections, we found a coordinate frame where the gravitational wave has no gauge freedom, the transverse-traceless gauge. In this frame, the gravitational wave has only two degrees of freedom, denoting the polarization of the wave. This frame is by the way very convenient for describing the gravitational wave, compute generation processes, etc. One purpose of this thesis is to model the detection of gravitational waves. The physical quantities of the detection process (position of the de-

tector, direction and evolution of the fields,...) are easily described in the frame of the detector itself, the proper detector frame, and we must choose one frame to describe everything. In this section we describe what are the characteristics of the transverse-traceless frame and the proper detector frame, and what is the most convenient frame to model the whole detection process.

Mathematically, one of the most interesting feature in general relativity is its covariance. That means that the tensorial laws are independent of any choice of frame. Among those different frames, the local inertial frame is to be pointed out. This frame is the one where test masses are free falling at a point of the spacetime P, so the space time becomes flat and the laws of physics become the ones of special relativity. It means that all the Christoffel symbols $\Gamma^{\mu}{}_{\nu\rho}$ vanish [(5)] and the geodesic equation (1.1.9) at the point P becomes

$$\left.\frac{d^2x^\mu}{d\tau^2}\right|_P = 0.$$

It means that in this frame, at one point in space at a specific moment, the test masses move freely. We can consider a region of space around the vicinity of the spacetime point P and keep the coordinates we constructed for the local inertial frame. These coordinates are called Riemann coordinates. The problem is that we have to repeat the construction of the coordinates if we consider an observer's trajectory, and as mentioned by Rakhmanov in [Rakhmanov, 2014], "*there is no obvious way to relate the coordinates constructed on two different reference points*". This is why we need coordinates where the test masses can move freely along a reference worldline and not a single reference point anymore. This is what we call Fermi-normal coordinates [Misner et al., 1973]. Those are built by a gyroscope moving along an observer's trajectory, the spin vector of the gyroscope s^μ will behave as

$$\frac{ds^\mu}{d\tau} + \Gamma^{\mu}{}_{\nu\rho}\, s^\mu \frac{dx^\rho}{d\tau} = 0. \tag{1.3.1}$$

The 4-spin vector in the rest frame can be expressed as $s^\mu = (0, \vec{s})$. This equation (1.3.1) can be seen as a generalization of the angular momentum conservation in a curved spacetime $\nabla_U\, s = 0$, where U is the 4-speed of the observer. The beginning of the construction of this frame is the same as for the Riemann coordinates, we build a local inertial frame at the point P, but with three gyroscopes to mark the spatial axes.

(5). Please note that only the Christoffel symbols $\Gamma^{\mu}{}_{\nu\rho}$ vanish, but their derivative do not. The Ricci scalar R does not vanish either, so the spacetime is not necessarily flat.

This frame is moved along the chosen geodesic, the gyroscopes defining the directions of spatial axes. Along this chosen geodesic, we have consequently that $\frac{ds^\mu}{d\tau} = 0$. In order to satisfy equation (1.3.1), the Christoffel symbols vanish not only at P, but all along the geodesic. That's what we call it a freely falling frame, used for instance to model drag-free satellites or space-based detectors.

Now let us introduce the frame used in gravitational wave theory. We already know the TT frame, the frame where we model the gravitational wave in the traceless-transverse gauge. In this set of coordinates, the gravitational wave is described by its two polarization modes, h_+ and $h_\times$ directly, and the equations (1.1.18) are satisfied. Let us show how this set of coordinates behaves physically. We take again the geodesic equation for a test mass initially at rest. Taking equation (1.1.9) for $\tau = 0$, we find

$$\left.\frac{d^2x^i}{d\tau^2}\right|_{\tau=0} = -\left[\Gamma^i{}_{00}\left(\frac{dx^0}{d\tau}\right)^2\right]_{\tau=0}. \tag{1.3.2}$$

Taking back the definition of Christoffel symbols (1.1.1) with the gauge equations (1.1.18), we find that all coefficients $\Gamma^i{}_{00}$ vanishes, meaning that the acceleration is null for a mass initially at rest (constant x^i), which implies that the mass will stay at rest at any time in this set of coordinates. The position of the test mass will remain the same when the gravitational wave passes. This conclusion seems paradoxical because we know from the geodesic deviation equation (1.1.20) that the gravitational wave will modify the distance between test masses. In order to get the positions of the test masses constant, the TT coordinates will stretch themselves when the gravitational wave passes. It can be seen as we measure distance in the TT gauge with a stretchable ruler in order to preserve the position of the masses. This result illustrates clearly that the physical observations are not related to the coordinates in general relativity. To model the physical effect on test masses, one must rely on the proper distance between them, the geodesic deviation.

The TT frame is not very suitable for earth-based detectors, due to the stretching of coordinate when a wave passes. In this thesis, we are going to study a detection process that uses a constant magnetic field. In the TT frame, the magnetic field will no longer be constant. This is not convenient for the computations because the derivatives of the field will no longer be zero, so our equations will be harder to handle. To model gravitational wave detection, we have to consider the proper detector frame,

first modeled by Manasse and Misner [Manasse and Misner, 1963], explained by Misner, Thorne and Wheeler in the famously known textbook Gravitation [Misner et al., 1973] and further developed by Ni and Zimmerman [Ni and Zimmermann, 1978] to cover all the aspects that implies an inertial observer in general relativity. The main advantage of such a frame is that we work in the frame of the laboratory, where coordinates are measured by rigid rulers. The easiest laboratory modeling we can get is a drag-free satellite. In this case, if we restrict our domain to a small region of space, the metric will remain flat at first order in the Fermi-normal coordinate we introduced earlier. It makes sense because we constructed the Fermi coordinates in a way that the Christoffel symbols vanish. The non-flat metric will appear when we push our analysis to second order, it has the form (see [Manasse and Misner, 1963] for details)

$$ds^2 = -c^2dt\left(1+R_{0i0j}x^ix^j\right) - 2cdtdx^i\left(\frac{2}{3}R_{0jik}x^jx^k\right) + dx^idx^j\left(\delta_{ij}-\frac{1}{3}R_{ikjl}x^kx^l\right), \tag{1.3.3}$$

where the Riemann tensor is evaluated at the point P, where we construct our coordinates. We can show that the components of the Riemann tensor restricted to the first order of the metric perturbation are invariant with respect to the frame [Maggiore, 2007], so we can compute the expression using the Riemann tensor in the TT frame. If we want to consider a detector on Earth, our frame is not in free fall anymore and other effects that appear at the Earth surface will influence the metric expression, that is found by Ni and Zimmerman [Ni and Zimmermann, 1978],

$$\begin{aligned} ds^2 =& -c^2dt\left(1+\frac{2}{c^3}\vec{a}\cdot\vec{x}+\frac{1}{c^4}\left(\vec{a}\cdot\vec{x}\right)^2-\frac{1}{c^2}\left(\vec{\Omega}\times\vec{x}\right)^2+R_{0i0j}x^ix^j\right) \\ &+2cdtdx^i\left(\frac{1}{c}\varepsilon_{ijk}\Omega^jx^k-\frac{2}{3}R_{0jik}x^jx^k\right)+dx^idx^j\left(\delta_{ij}-\frac{1}{3}R_{ikjl}x^kx^l\right), \end{aligned} \tag{1.3.4}$$

where $\vec{a}=-\vec{g}$ is the classical local gravitational acceleration and Ω^i is the angular velocity of the laboratory with respect to local gyroscopes. The term in $(\vec{a}\cdot\vec{x})$ is due to the inertial acceleration, and the one in $(\vec{a}\cdot\vec{x})^2$ is the gravitational redshift. The time dilation due to the angular velocity is denoted by the term in $\left(\vec{\Omega}\times\vec{x}\right)^2$. Finally, the term $\frac{1}{c}\varepsilon_{ijk}\Omega^jx^k$ is known as the Einstein-Sagnac effect, and is related to the impossibility to synchronize clocks in a closed accelerated path.

This metric (1.3.4) describe fully the spacetime when a gravitational wave passes in the Fermi-normal coordinates. However, as detailed in [Maggiore, 2007], the effects

of the gravity acceleration $\vec{g}$ are compensated by the suspension mechanism of the detector, and other effects coming from the Earth detector location can be considered as quasi-static with respect to the detection process, because the process time scales are far shorter than the Earth rotation and those effects become negligible. It means that using the metric described in (1.3.3) is a neat and accurate approximation, at least when the wavelength of the gravitational wave considered is small compared to the size of the detector. This is because equation (1.3.3) is a series expansion limited to the second order of coordinates, and if we consider sinusoidal gravitational wavse of wavelength λ, this expansion will be in powers of $\left(\frac{x^i}{\lambda}\right)$, so we may need more orders in the Taylor expansion in coordinates. This was made by Fortini and Gualdini in [Fortini and Gualdi, 1982] for general gravitational fields and specifically made for any gravitational weak field by Marzlin in [Marzlin, 1994]. For an inertial observer, the metric in Fermi-normal coordinates is given by

$$g_{00} = -1-2\sum_{n=0}^{\infty}\frac{n+3}{(n+3)!}\frac{\partial^n}{\partial x^{m_1}\ldots\partial x^{m_n}}R_{0k0l}\; x^k x^l x^{m_1}\ldots x^{m_n}, \tag{1.3.5}$$

$$g_{0j} = -2\sum_{n=0}^{\infty}\frac{n+2}{(n+3)!}\frac{\partial^n}{\partial x^{m_1}\ldots\partial x^{m_n}}R_{0kjl}\; x^k x^l x^{m_1}\ldots x^{m_n}, \tag{1.3.6}$$

$$g_{ij} = \delta_{ij}-2\sum_{n=0}^{\infty}\frac{n+1}{(n+3)!}\frac{\partial^n}{\partial x^{m_1}\ldots\partial x^{m_n}}R_{ikjl}\; x^k x^l x^{m_1}\ldots x^{m_n}. \tag{1.3.7}$$

These series expansions show how we can express the metric and moreover the metric perturbation for any weak gravitational field. In further computation in this manuscript, we will consider an incoming gravitational plane wave, and its propagation is along the Z-axis in the detector frame. Rakhmanov [Rakhmanov, 2014] showed simplified expression of the metric perturbation in the Fermi-normal Cartesian coordinates, for a gravitational wave propagating along the Z-axis, in the negative direction, the $h_{\mu\nu}$ components are

$$h_{11} = P_+, \tag{1.3.8}$$

$$h_{22} = -P_+, \tag{1.3.9}$$

$$h_{12} = P_\times, \tag{1.3.10}$$

$$h_{13} = -\frac{1}{z}\left(xP_+ + yP_\times\right), \tag{1.3.11}$$

$$h_{23} = -\frac{1}{z}\left(xP_\times - yP_+\right), \tag{1.3.12}$$

$$h_{33} = \frac{1}{z^2}\left(\left[x^2-y^2\right]P_+ + 2xyP_\times\right), \tag{1.3.13}$$

$$h_{01} = -\frac{1}{z}\left(xQ_+ + yQ_\times\right), \tag{1.3.14}$$

$$h_{02} = -\frac{1}{z}\left(xQ_\times - yQ_+\right), \tag{1.3.15}$$

$$h_{03} = \frac{1}{z^2}\left(\left[x^2-y^2\right]Q_+ + 2xyQ_\times\right), \tag{1.3.16}$$

$$h_{00} = 2h_{03} - h_{33}, \tag{1.3.17}$$

where

$$P_{+,\times}(z,t) = \sum_{n=2}^{\infty}\frac{n-1}{(n+1)!}z^n\frac{d^n h^{\mathrm{TT}}_{+,\times}(t)}{dt^n}, \tag{1.3.18}$$

$$Q_{+,\times}(z,t) = \sum_{n=2}^{\infty}\frac{n}{(n+1)!}z^n\frac{d^n h^{\mathrm{TT}}_{+,\times}(t)}{dt^n}. \tag{1.3.19}$$

The equations above will be convenient for the analytical treatment of the detection in the manuscript in chapter 3. We can now fully express the gravitational wave tensor $h_{\mu\nu}$ in the detector frame with the Fermi-normal coordinates, and it depends only on the gravitational wave in the TT gauge and the coordinates. From this we can note that solving the wave equation (1.1.16) in another frame than the TT frame is equivalent to propagating the gauge-related and physics-related degrees-of-freedom. Analytically, Rakhmanov [Rakhmanov, 2014] showed that there is no divergence for the metric tensor perturbation at $z = 0$ since it has a finite limit.

In this chapter we have introduced all the concepts involving the modeling and the detection of gravitational waves, insisting on the high frequency sources. Now, before entering in a theoretical conception of an electromagnetic detector, we must take a look at how electromagnetism interacts with gravitation and gravitational waves. This will be done in the next chapter.

Chapter 2

Electromagnetism and Gravitational Waves

In this chapter, we first introduce how gravitation and electromagnetism interact through the Einstein-Maxwell system. Then we focus on electromagnetic interactions of gravitational waves, by describing the Gertsenshtein effects. The closing of this chapter is a review on research using the inverse Gertsenshtein effect as a gravitational wave detection.

2.1 The Einstein-Maxwell system

The name of Einstein-Maxwell system comes from two important physicists that, in their way, improved theoretical physics a lot. The first one is James Clerk Maxwell, who contributed to the foundation of classical electrodynamics and the second one is Albert Einstein, founder of general relativity theory. The system that combines their names also combines their fields. The Einstein-Maxwell system shows how we can do electrodynamics in curved spacetime, in the framework of general relativity. On the other hand, the stress-energy tensor used to denote the matter/energy content in the spacetime is also sourced by the electromagnetic energy.

In this section, we are going to add electrodynamics in our theory of gravitation, and see what is the coupling between these two fundamental interactions. Here we consider the minimal coupling between them.

To do so, let us recall the Einstein-Hilbert action S_{E-H} from equation (1.1.3), the action of general relativity where we add an electromagnetic action S_{EM} defined by

$$S_{EM} = -\int_M \left(\frac{1}{4c\mu_0} g^{\mu\rho} g^{\nu\sigma} F_{\rho\sigma} F_{\mu\nu} + \frac{1}{c^2} g^{\mu\nu} A_\mu j_\nu \right) \sqrt{-g}\, d^4x \tag{2.1.1}$$

where μ_0 is the vacuum magnetic permeability. This action has two different contributions. The first one is the term of the electromagnetic fields, contained in the antisymmetric Faraday tensor $F_{\mu\nu}$, and the second one is the term of the electromagnetic sources, where A_μ is the 4-potential and contains the electromagnetic potentials and j_μ is the 4-current that contains the charge density and current densities. Similarly to the construction of the Einstein equation (1.1.6), we are going to consider a total action $S_{tot} = S_{E-H} + S_{EM}$ and the variation of this action with respect to the metric leads obviously to the Einstein equation (1.1.6), but with the electromagnetic stress-energy tensor $T^{(EM)}_{\mu\nu}$ that can be expressed as

$$T^{(EM)}_{\mu\nu} = \frac{1}{\mu_0} \left(F_{\mu\rho} F_\nu{}^\rho - \frac{1}{4} g_{\mu\nu} F_{\rho\sigma} F^{\rho\sigma} \right). \tag{2.1.2}$$

This tensor put into equation (1.1.6) describes how the electromagnetic energy curves spacetime. The metric describing an electromagnetic spacetime must satisfy the Einstein equation (1.1.6) sourced by the stress-energy tensor (2.1.2). Please note that in this case the trace of the stress-energy tensor (2.1.2) is null [(1)], so, the Einstein equation can be rewritten as

$$R_{\mu\nu} = \frac{8\pi G}{c^4} T^{(EM)}_{\mu\nu}. \tag{2.1.3}$$

This is for instance the case of the charged black-hole metrics of Reissner-Nordström [Reissner, 1916, Weyl, 1917, Nordström, 1918] and Kerr-Newmann [Kerr, 1963, Newman et al., 1965, Newman and Janis, 1965]. Please note that the trace of the stress-energy tensor (2.1.2) is null. You can relate this physically as a consequence of the fact that the photon is massless.

(1). This is called a null-fluid solution

Now we have shown how electromagnetism interacts with gravitation, let us see how gravitation and a curved spacetime has an influence on electromagnetic fields. For that purpose, we have to remind how the electromagnetic fields are related to the electromagnetic 4-potential. The relation is, for any metric

$$F_{\mu\nu} = \nabla_\mu A_\nu - \nabla_\nu A_\mu = \partial_\mu A_\nu - \partial_\nu A_\mu, \tag{2.1.4}$$

where the latter is obtained due to the symmetry of the Christoffel symbols. This construction has automatically one property that leads to the first group of Maxwell equations, which are

$$\partial_\kappa F_{\mu\nu} + \partial_\mu F_{\nu\kappa} + \partial_\nu F_{\kappa\mu} = 0. \tag{2.1.5}$$

The second group of Maxwell equations is found by considering the action variation of S_{tot} with respect to the 4-potential A_μ, which leads to

$$\nabla_\mu F^{\mu\nu} = -\mu_0 j^\nu. \tag{2.1.6}$$

These Maxwell equations contains the four common Maxwell equations of classical electrodynamics in vacuum [Jackson, 1998]. If as in [Hobson et al., 2006] we take these equations in Minkowski spacetime, with Cartesian coordinates, we have that $A_\mu = (c\phi, \vec{A})$, where ϕ is the scalar electric potential and $\vec{A}$ the vector potential. The 4-current is $j_\mu = (c\rho, \vec{j})$ where ρ is the charge density and $\vec{j}$ the current density. With these assumptions, the Faraday tensor becomes

$$F_{\mu\nu} = \begin{pmatrix} 0 & E_x/c & E_y/c & E_z/c \\ -E_x/c & 0 & -B_z & B_y \\ -E_y/c & B_z & 0 & -B_x \\ -E_z/c & -B_y & B_x & 0 \end{pmatrix} \tag{2.1.7}$$

and we can rewrite the first group of Maxwell equations (2.1.5) as

$$\vec{\nabla} \cdot \vec{B} = 0, \tag{2.1.8}$$

$$\vec{\nabla} \times \vec{E} = -\frac{\partial \vec{B}}{\partial t}, \tag{2.1.9}$$

and the second group (2.1.6) as

$$\vec{\nabla}\cdot\vec{E} = \frac{\rho}{\varepsilon_0}, \tag{2.1.10}$$

$$\vec{\nabla}\times\vec{B} = \mu_0\vec{j}+\mu_0\varepsilon_0\frac{\partial\vec{E}}{\partial t}. \tag{2.1.11}$$

We thus have shown how we can generalize the master equations of classical electrodynamics in the frame of general relativity. If we combine the two groups (2.1.5) and (2.1.6), we can obtain the curved spacetime version of the electromagnetic wave equation for the electromagnetic fields [Tsagas, 2005], which is

$$g^{\alpha\beta}\nabla_\alpha\nabla_\beta F_{\mu\nu} + R_{\mu\nu\alpha\beta} F^{\alpha\beta} + R^\alpha{}_\mu F_{\nu\alpha} + R^\alpha{}_\nu F_{\alpha\mu} = \nabla_\mu j_\nu - \nabla_\nu j_\mu, \tag{2.1.12}$$

with the Riemann tensor $R_{\mu\nu\alpha\beta}$ and Ricci tensor $R^\alpha{}_\nu$ previously defined. This equation shows that the generation and the propagation of the electromagnetic fields are influenced by the geometry of the spacetime. This is the key idea of the Gertsenshtein effects. This coupling will allow us to consider generation and detection of gravitational waves using electromagnetic fields.

To finish this section about the Einstein-Maxwell system, let us recall the equations that we construct here above,

$$\begin{cases} R_{\mu\nu} = \dfrac{8\pi G}{c^4}T^{(EM)}_{\mu\nu}, & (2.1.3)\\ T^{(EM)}_{\mu\nu} = \dfrac{1}{\mu_0}\left(F_{\mu\rho}F_\nu{}^\rho - \dfrac{1}{4}g_{\mu\nu}F_{\rho\sigma}F^{\rho\sigma}\right), & (2.1.2)\\ \nabla_\sigma F_{\mu\nu}+\nabla_\nu F_{\sigma\mu}+\nabla_\mu F_{\nu\sigma}=0, & (2.1.5)\\ \nabla_\mu F^{\mu\nu} = -\mu_0 j^\nu. & (2.1.6) \end{cases}$$

This system, applied with gravitational wave theory, will ease the introduction and the understanding of a key concept in this manuscript, the Gertsenshtein effects. Please note that the Maxwell equations in curved spacetime (2.1.5) and (2.1.6) can be verified experimentally since the light is deflected by curved spacetime. By the way the fact that electromagnetic energy couples minimally the gravitation in equations (2.1.3) and (2.1.2) is not yet verified by specific tests [Füzfa, 2016].

2.2 Gertsenshtein effects

The Gertsenshtein effect is a theoretical mechanism introduced in 1962 by Mikhail Evgeny Gertsenshtein which he called the wave resonance mechanism [Gertsenshtein, 1960]. The effect can be described as follows. The passing of an electromagnetic wave in a strong constant magnetic field region will produce a gravitational wave, with the same frequency than its progenitor. Let us now describe this effect using the Einstein-Maxwell system.

As described by Gertsenshtein, we have two different fields in the mechanism, a strong constant magnetic field $F^{(c)}_{ij}$ and a passing electromagnetic wave $F^{(w)}_{\mu\nu}$. If we consider a Faraday tensor made of these two fields, $F_{\mu\nu} = F^{(c)}_{\mu\nu} + F^{(w)}_{\mu\nu}$, the stress-energy tensor computed from equation (2.1.2) will have the form

$$T^{(EM)}_{\mu\nu} = T^{(c)}_{\mu\nu} + T^{(w)}_{\mu\nu} + T^{(g)}_{\mu\nu} \tag{2.2.1}$$

because equation (2.1.2) is quadratic with respect of the Faraday tensor. The term $T^{(c)}_{\mu\nu}$ only contains terms in $\left(F^{(c)}\right)^2$, the $T^{(w)}_{\mu\nu}$ term only contains terms in $\left(F^{(w)}\right)^2$, and $T^{(g)}_{\mu\nu}$ will only contains mixed terms in $\left(F^{(c)}F^{(w)}\right)$. This will lead to take into account three different metric perturbations, each one sourced by one of the stress-energy tensor contribution. The metric has the form

$$g_{\mu\nu} = \eta_{\mu\nu} + c_{\mu\nu} + w_{\mu\nu} + h_{\mu\nu}, \tag{2.2.2}$$

where $c_{\mu\nu}$ is sourced by $T^{(c)}_{\mu\nu}$ and is a pure static perturbation. This electromagnetic gravitational static field generation was studied by André Füzfa for current loops and solenoids [Füzfa, 2016]. The second perturbation $w_{\mu\nu}$ is sourced by $T^{(w)}_{\mu\nu}$ which is a varying term but the frequency content would be the double frequency of $F^{(w)}_{\mu\nu}$. Its amplitude could be faint and negligible compared to the next term, $h_{\mu\nu}$, sourced by $T^{(g)}_{\mu\nu}$ and is the Gertsenshtein effect. Its frequency content will be the same as $F^{(w)}_{\mu\nu}$ and its amplitude should be much greater than $w_{\mu\nu}$, since $h_{\mu\nu}$ is sourced by a combination of static-varying fields. The $w_{\mu\nu}$ term is sourced by a pure varying term and the static field is much more intense. The Gertsenshtein effect is thus coming from the mixed terms in the expression of the stress-energy tensor. Here is how Gertsenshtein imagined generating gravitational waves using electromagnetic fields, which is a very

faint process, due to the extreme weakness of gravitational coupling. Indeed, the produced metric perturbation is given by

$$h_{\mu\nu}(t,\vec{r}) = \frac{4G}{c^4}\int \frac{d\vec{r}'}{|\vec{r}-\vec{r}'|} T^{(g)}_{\mu\nu}\left(t_{ret},\vec{r}'\right). \tag{2.2.3}$$

Dimensional analysis indicates that the metric perturbation produced through the Gertsenshtein mechanism have an amplitude of order

$$h_{\mu\nu} \sim \frac{4GB_0E_0L^2}{c^5\mu_0}\ , \tag{2.2.4}$$

where L is the size of the region in which the magnetic field and the electromagnetic wave interact, and where B_0 and E_0 are respectively the amplitudes of the static magnetic and varying electric fields respectively. To illustrate the fact that the coupling is tiny, in order to generate a strain of the order of the first detection of gravitational waves [Abbott et al., 2016], $h \approx 10^{-21}$ with $B_0 \approx 10$ T and $E_0 \approx 1\,\mathrm{MV/m}$, one needs an interacting region of $L \approx 10^6$ km. The direct Gertsenshtein effect can be used to build electromagnetic gravitational wave generators, but its realization constitutes an extreme experimental challenge, and even if one can generate them, their detection is for now uncertain. Nevertheless, generating gravitational waves with electromagnetic fields could be a direct test for the minimal coupling between gravitation and electromagnetism, in the weak field regime. This is what we call the direct Gertsenshtein effect, because in his paper of 1960 [Gertsenshtein, 1960], Gertsenshtein said that the inverse process is "*hardly of interest*" and indeed, we could possibly detect gravitational waves because their passing in a strong magnetic field region will induce a faint electromagnetic field.

This is what we call the inverse Gertsenshtein effect. Physically, it can be described as follows. A gravitational wave fundamentally constitutes a local distortion of volume. If we put a magnetic field on the way of this spacetime distortion, the passing gravitational wave will modify the electromagnetic flux by affecting the volume, giving rise to an induced electromagnetic field from Faraday's law. This induced EM field is the signature of the passing of a gravitational wave, as it inherits frequency from its gravitational progenitor. Just as the direct effect, the inverse Gertsenshtein effect can be described through the Einstein-Maxwell system.

To do so, we are going to consider a spacetime metric with a Minkowski background and an incoming gravitational wave $g_{\mu\nu} = \eta_{\mu\nu} + h_{\mu\nu}$. Just as for the direct effect, the electromagnetic field has two contributions. The first one is a strong static magnetic field $F^{(0)}_{ij}$, that represents our field at the zeroth order of perturbation, and the electromagnetic wave induced by the inverse Gertsenshtein effect $F^{(1)}_{\mu\nu}$ is a field at the first order of perturbation. With these assumptions, our Faraday tensor has the form

$$F_{\mu\nu} = F^{(0)}_{\mu\nu} + F^{(1)}_{\mu\nu}. \tag{2.2.5}$$

Assuming that the gravitational wave is in the TT gauge (1.1.18), we can linearize the electromagnetic wave equation in curved spacetime, by neglecting all terms of order greater than one. This result was obtained by Grishchuk [Grishchuk and Sazhin, 1975, Grishchuk, 1977] and the wave equation is

$$\begin{aligned} g^{\alpha\beta}\nabla_\alpha\nabla_\beta F^{(1)}{}_{\mu\nu} &= h^{\alpha\kappa}\ \nabla^{(\eta)}_\alpha\nabla^{(\eta)}_\kappa F^{(0)}{}_{\mu\nu} - \partial_\rho\left(\partial_\mu h_{\alpha\nu}\ - \partial_\nu h_{\alpha\mu}\ \right)F^{(0)\,\rho\alpha} \\ &\quad - \left(\partial^\gamma h^{\alpha\beta}\ + \partial^\alpha h^{\beta\gamma}\ - \partial^\beta h^{\gamma\alpha}\ \right) \\ &\quad \left(\eta_{\alpha\mu}\ \nabla^{(\eta)}_\gamma F^{(0)}{}_{\nu\beta} - \eta_{\alpha\nu}\ \nabla^{(\eta)}_\gamma F^{(0)}{}_{\mu\beta}\ \right) = S_{\mu\nu}, \end{aligned} \tag{2.2.6}$$

where $\nabla^{(\eta)}$ denotes the covariant derivative in the Minkowski metric [(2)]. In this equation above, we do not consider yet that the external magnetic field is constant. In this case, all the terms involving $\nabla^{(\eta)}F$ vanishes, and equation (2.2.6) simplifies to

$$g^{\alpha\beta}\nabla_\alpha\nabla_\beta F^{(1)}{}_{\mu\nu} = -\partial_\alpha\left(\partial_\mu h_{\beta\nu}\ - \partial_\nu h_{\beta\mu}\ \right)F^{(0)\,\alpha\beta}\ . \tag{2.2.7}$$

In both equations (2.2.6) and (2.2.7), the wave equation operator is applied to the induced electromagnetic field, and the source is involving the incoming gravitational wave, and the external magnetic field. Mathematically, one can retrieve the wave equation sourced by an effective 4-current density, if we assume an effective 4-current defined by

$$j^{\text{eff}}_\mu = \frac{1}{\mu_0}\partial_\alpha h_{\beta\mu}\, F^{\alpha\beta\,(0)}. \tag{2.2.8}$$

Then the source of the wave equation (2.2.7) can be rewritten as the curl of the 4-

(2). This is equivalent to simple derivative in Cartesian coordinates but not necessarily in other coordinates.

current density, such as

$$g^{\alpha\beta}\nabla_\alpha\nabla_\beta F^{(1)}{}_{\mu\nu} = \mu_0\left(\partial_\nu j_\mu^{\text{eff}} - \partial_\mu j_\nu^{\text{eff}}\right). \tag{2.2.9}$$

With an equation of the form of (2.2.9), we can consider for further treatment the classical inhomogeneous electromagnetic wave equations in vacuum which are

$$\frac{1}{c^2}\frac{\partial^2\vec{E}}{\partial t^2} - \vec{\Delta}\vec{E} = -\left(\frac{1}{\varepsilon_0}\vec{\nabla}\rho + \mu_0\frac{\partial\vec{j}}{\partial t}\right), \tag{2.2.10}$$

$$\frac{1}{c^2}\frac{\partial^2\vec{B}}{\partial t^2} - \vec{\Delta}\vec{B} = \mu_0\vec{\nabla}\times\vec{j}. \tag{2.2.11}$$

where $\vec{\Delta}$ is the vectorial Laplacian.

To use the equations above, we only need to switch the effective current density j_μ^{eff} into an effective charge density ρ^{eff} and effective current density $\vec{j}^{\text{eff}}$. This decomposition will be very convenient to apply some classical electrodynamics methods when we will study the detection.

Anyway, the simplicity of such equations are partially due to the fact of assuming our gravitational wave in the TT gauge. By the way, we introduced in the previous chapter the proper detector frame in which any earthbound detection must be modeled. In this frame, astrophysical gravitational waves no longer holds the TT gauge equation, and we need to take back all our computations, but there is a more elegant and direct way to retrieve directly the effective 4-current density used in equation (2.2.9). This was shown by Berlin et al. [Berlin et al., 2022], considering the electromagnetic action and linearizing it directly in terms of

$$\begin{aligned} S_{EM} &= \int_M \frac{1}{4\mu_0} g^{\mu\rho} g^{\nu\sigma} F_{\rho\sigma} F_{\mu\nu}\sqrt{-g}\, d^4x \\ &= \int_M \left(\frac{1}{4\mu_0}\eta^{\mu\rho}\eta^{\nu\sigma}F_{\rho\sigma}F_{\mu\nu} + \eta^{\mu\nu}A_\mu j_\nu^{\text{eff}}\right) d^4x + \mathscr{O}(h^2) \end{aligned} \tag{2.2.12}$$

with

$$j_\mu^{\text{eff}} = \frac{1}{\mu_0}\partial_\alpha\left(h_{\beta\mu}F^{\alpha\beta} + h^{\alpha\beta}F_{\beta\mu} + \frac{h}{2}F_\mu{}^\alpha\right). \tag{2.2.13}$$

This new effective 4-current density is very useful, because it generalizes the one we found earlier in equation (2.2.8) but with no assumptions about the gauge used to

model the metric perturbations. We can just put the effective 4-current obtained in equation (2.2.13), into equation (2.2.9), and we can solve the electromagnetic field induced by the inverse Gertsenshtein effect.

We now have all the theoretical background to study the detection of high-frequency gravitational waves by resonant electromagnetic cavities, using the inverse Gertsenshtein effect. Before that, we are going to perform a small review of inverse Gertsenshtein effect gravitational wave detection in order to compare our detector proposal with other works.

2.3 Review on HFGW EM detection proposals

In this section, we are going to review the resonant electromagnetic detectors using inverse Gertsenshtein effect. The first part contains results right after the original Gertsenshtein paper. The second one contains some promising detector proposals recently published.

2.3.1 The first paper of Gertsenshtein and immediate further research

After the discovery of the wave resonance mechanism by Gertsenshtein [Gertsenshtein, 1960] in the early 1960s, the first period where inverse Gertsenshtein research was active is the next decade. In parallel of Gertsenshtein paper, Lupanov [Lupanov, 1967] proposed to use a capacitor with an external electric field to detect gravitational waves. The next step, inspired by the two Soviet physicists mentioned above, a team of Bologna in Italy [Boccaletti et al., 1970] provided analytical developments about the direct and the inverse Gertsenshtein effect. They used general relativity and scattering theory to give robust mathematical formulations of the mechanisms. They even proposed at the end of the paper a first experimental setup for a gravitational Hertz experiment, i.e. generating and detecting gravitational waves in the same process. After that, some progress was made by Soviet physicists of the Moskow State University, the first paper [Braginskii and Menskii, 1971] mentioned the way to detect gravitational waves in a resonator with a packet of electromagnetic waves, the next one [Braginskii et al., 1973] proposed to use a waveguide to detect gravitational wave in a strong external magnetic field, and analyze it with the projection of the wave equation on the

proper modes of the waveguide. The two final ones were made by Leonid Grishchuk that introduced the damping of the oscillation due to the cavity walls [Grishchuk and Sazhin, 1975] and in 1977 the case where the external field could oscillate [Grishchuk, 1977], and proposed another gravitational Hertz experiment with a coaxial cylindrical section. The end of the 1970s was quite prolific, with the work of Pegoraro, Radicati and Picasso [Pegoraro et al., 1978b, Pegoraro et al., 1978a] where they insisted on the fact that resonant electromagnetic detectors can be tunable to match the frequency they wanted to detect. The use of oscillating fields, generation and detection of gravitational waves were also mentioned in this paper. Their detector response is proportional to the strain amplitude and they mentioned the difficulty in terms of noises to detect tiny fluctuating values in a strong external field. At the same time, Caves [Caves, 1979] imagined to use the cavity walls in a strong external magnetic field to detect the gravitational waves. Indeed, the passing of a gravitational wave will interacts with the walls and will allow transitions from excited modes and nearly unexcited modes. Then, de Logi and Michelson [De Logi and Mickelson, 1977] provided a quantum explanation of the inverse Gertsenshtein effect. As explained by Cruise later in [Cruise, 2012], *"An incoming graviton interacts with the virtual photon of the static magnetic field and a real photon is generated by the conversion process."* The work of de Logi and Michelson provides some cross sections of potential conversions. They were inspired by the work [Boccaletti et al., 1968]. The next decades have been less active because of the development of interferometry techniques to detect gravitational waves. The regain on interest in high frequency gravitational waves detection will rise the interest in the inverse Gertsenshtein effect. During these decades, we can nonetheless describe in few words the work of [Macedo and Nelson, 1983] where they studied how a gravitational wave behaves in a magnetized plasma. They finally said that the study of such a situation will be very interesting for gravitational wave detection. In the 1990s two papers got our attention, the first one is [Gerlach, 1992], that studied the induced birefringence in the interior of a cavity, how the information of the gravitational wave changes through the passing in a cavity. The second one is [Minakov et al., 1992], that prospected the use of the ionosphere and its electric field as a resonator. In 2003, a collaboration between the CERN and Genova University [Ballantini et al., 2003] led to the design of two coupled spherical microwave cavities to detect gravitational waves, where the detection process is inherited from [Caves, 1979]. We finish this section with the work of Adrian Cruise, that described the rotation of the polarization plane of an electromagnetic wave due to the passing

gravitational waves [Cruise, 1983], and this work was continued in [Cruise, 2000] with more experimental prospects for detection. The aim is to measure this polarization change with a quantum formalism from de Logi [De Logi and Mickelson, 1977]. Since this is a quantum work, they automatically have a generated power quadratic with the strain amplitude, because there is no possibilty to detect the energy variation at first order by detecting photons. Finally, preliminary work about the development of a gravitational Hertz experiment in 2015 using electromagnetic fields was published by Kolosnitsyn and Rudenko [Kolosnitsyn and Rudenko, 2015].

Please note that there exists also the Li effect, described in [Li et al., 2003, Li et al., 2008], where the effect is claimed to be amplified by adding a Gaussian beam photon flux detection. This technique will induce a first order perturbative photon flux, but the noise sensitivity could be unchanged because of the noise and measuring small fluctuations in a dense, oscillating medium. The Li-Baker detector [Baker et al., 2008] and possible applications of high-frequency gravitational waves [Baker, 2005] were analyzed and strongly criticized by the US national security [JASON Program office - The MITRE Corporation, 2008].

2.3.2 Interests in the Inverse Gertsenshtein effect after LIGO detection

After the LIGO first gravitational wave detection [Abbott et al., 2016], the interest in different detection techniques, especially at high frequencies, has been renewed. Thus, several detector proposals came into the spotlight in the few last years. The first was [Ejlli et al., 2019], based on the classical graviton-photon mixing formalism by Damian Ejlli [Ejlli and Thandlam, 2019], inspired by the work on axion-photon mixing (3) [Raffelt and Stodolsky, 1988]. The aim is to use some resonant cavities used for axion detection in the frame of gravitational wave detection. The work is well-documented, provides a generated energy quadratic with the strain amplitude and gets a strain sensitivity around 10^{-25} at very high frequencies ($10^{15} Hz$). Further computations were made in [Ejlli, 2020].

(3). [Raffelt and Stodolsky, 1988] is an article centered on axion-photon mixing, but gives the first prospects for graviton-photon mixing.

The second detector proposal is a response from the Li effect concerns about the advantage of bringing a Gaussian beam. It was answered in [Zheng et al., 2018], where instead of this beam they imagined an oscillating external field to get a first order generated electromagnetic energy, by using the inverse Gertsenshtein effect. Further work [Zheng and Wei, 2022] gives prospects about the potential noise sources.

More recently, the paper [Berlin et al., 2022] brings another point of view on the inverse Gertsenshtein effect modeling. The authors formalize the modeling of the detection in the proper detector frame. Most of the proposals before were modeled in the TT frame. They get a second order generated electromagnetic energy because they discard quantities that vanish in a simple time average. They modeled the detection in TM/TE cavities and shows the directional sensitivity for several modes in the case of monochromatic gravitational wave detection. This directional sensitivity is accurate since they take into account all the terms present in the Taylor series of equations (1.3.5) to (1.3.7). The recent preprint [Schmieden and Schott, 2022] proposes to use the Compact Muon Solenoid (CMS) experiment magnet system to improve the sensitivity of this cavity proposal. In the same way, the proposal [Domcke and Garcia-Cely, 2021] provides also a way to detect high-frequency gravitational waves using low-mass haloscopes. They propose to use a torroidal cavity used for axion detection, and they compute the magnetic flux since this haloscope searches for an anomalous magnetic flux. They provide good sensitivity curve since they have already the ones for the axion detector. They also considered only monochromatic plane wave to model their detection.

At the same time, André Fűzfa patented [Füzfa, 2018] some devices and methods either to generate or detect gravitational waves using the Gertsenshtein effects. This is one of the patented design that we are going to model and study in the following of this manuscript. The patented idea we use is measuring the root-mean-square induced electromagnetic power in an electromagnetic cavity, where an external magnetic field boosts specific cavity modes. At the end of this manuscript, we will compare our detector proposal with the ones mentioned above.

All these detector proposals, including ours, were mentioned in a variety of papers in the last two years either to motivate or prospecting the detection of potential sources. Among these you can see in [Pujolas et al., 2021, Franciolini et al., 2022] prospects for probing primordial blank hole binaries and [Ringwald et al., 2021, Ringwald and Tamarit, 2022] for the search of the stochastic gravitational wave background. In [Ringwald and Tamarit, 2022], the authors provide prospects for its further experimental detection, with a detector using the Li effect.

Now we have all in our hands to begin the modeling of the detector and develop analytically our detector proposal.

Chapter 3

Detector proposal and analysis

In this chapter, we are going to study the case of two resonant electromagnetic detectors, suited for high frequency gravitational waves. We first describe the geometry of these detectors, and then perform electromagnetic modes analysis to compute an electromagnetic response that one could measure.

3.1 Modeling the detector

The detector proposal that we make in this manuscript is the use of resonant electromagnetic cavities, immersed in a strong external magnetic field, to detect high-frequency gravitational waves. The use of such a device was mentioned first by Grishchuk [Grishchuk, 1977], and imagined in few other works [Caves, 1979, Berlin et al., 2022], but the detectors we are going to study here were patented by André Füzfa in 2018 [Füzfa, 2018].

The detectors are constituted by either a waveguide or a cavity in vacuum immersed into a transverse static magnetic field that will boost the output signal through a resonance mechanism on specific radiation modes that are excited by the passing gravitational waves.

Let us now present our proposed experimental set-ups (figure 3.1). One can either consider the resonance of the induced electromagnetic waves inside a cylindrical cavity of radius R (TM resonator) or inside a waveguide made of two (or more) concentric open cylinders with inner radius R_1 and outer radius R_2 (TEM resonator). The cavities symmetry axis is the Z-axis. We denote by L the length of the resonators and by $\vec{B}^{(0)}_{\text{ext}} = B_0\vec{e}_x$ the external magnetic field, assumed to be of constant magnitude along the X-axis for simplicity. Please note that any electromagnetic induced field inside an ideal resonator must verify the boundary conditions along any perfect conducting surfaces which are

$$\vec{E}^{(1)}_{\parallel} = \vec{B}^{(1)}_{\perp} = \vec{0}. \tag{3.1.1}$$

Now that we have defined our detectors, we can express the induced field by the inverse Gertsenshtein effect, using equation (2.2.9). To simplify this equation, one can deduce that our zeroth order Faraday tensor has for only non-vanishing component in Cartesian coordinates (ct, x, y, z) in the proper detector frame,

$$F^{(0)}_{yz} = -F^{(0)}_{zy} = -B_0. \tag{3.1.2}$$

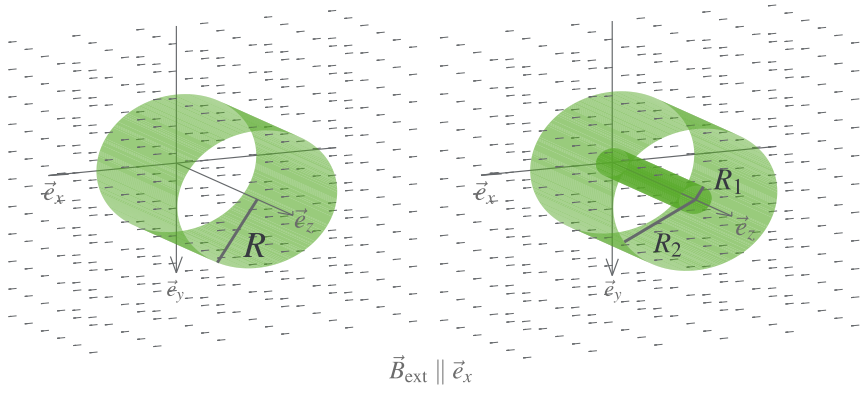

Figure 3.1 – Schematic representation of the experimental designs: a cylindrical TM cavity (left) and TEM waveguide (right), both immersed in an external static and transverse magnetic field.

This equation will considerably reduce the number of terms involved in the computation of j_μ^{eff}. In the following, we are going to consider a total 4-current density that has four different contibutions

$$j^\mu_{\text{tot}} = j^\mu_{\text{eff}} + j^\mu_{\text{loss}} = j^\mu_1 + j^\mu_2 + j^\mu_3 + j^\mu_{\text{loss}} \tag{3.1.3}$$

where

$$\begin{aligned} j^\mu_1 &= \frac{1}{\mu_0} F^{\alpha\beta}_{(0)} \partial_\alpha h_\beta{}^\mu, && (3.1.4)\\ j^\mu_2 &= \frac{1}{\mu_0} F_{(0)\beta}{}^{\mu} \partial_\alpha h^{\alpha\beta}, && (3.1.5)\\ j^\mu_3 &= \frac{1}{2\mu_0} F^{\mu\alpha}_{(0)} \partial_\alpha h, && (3.1.6)\\ j^\mu_{\text{loss}} &= \sigma F^{0\mu}_{(1)}. && (3.1.7) \end{aligned}$$

The three first terms are the three contributions of the effective 4-current described in equation (2.2.13). Please note that if the incoming gravitational wave is traceless ($h = 0$) and satisfies the Lorenz gauge condition ($\partial_\alpha h^{\alpha\beta} = 0$), the terms j^μ_2 ans j^μ_3 vanishes. The term j^μ_{loss} denotes the ohmic losses at the cavities walls. To ease the analysis of the electromagnetic response in the detectors, we set $(j^\mu_{\text{tot}}) = (c\rho_{\text{tot}}, \vec{j}_{\text{tot}})$ and we recover the classical inhomogeneous electromagnetic wave equations in vacuum (2.2.10) and (2.2.11)

$$\begin{aligned} \frac{1}{c^2}\frac{\partial^2 \vec{E^{(1)}}}{\partial t^2} - \vec{\Delta} \vec{E^{(1)}} &= -\left(\frac{1}{\varepsilon_0} \vec{\nabla} \rho^{\text{tot}} + \mu_0 \frac{\partial \vec{j^{\text{tot}}}}{\partial t} \right), && (3.1.8)\\ \frac{1}{c^2}\frac{\partial^2 \vec{B^{(1)}}}{\partial t^2} - \vec{\Delta} \vec{B^{(1)}} &= \mu_0 \vec{\nabla} \times \vec{j^{\text{tot}}}. && (3.1.9) \end{aligned}$$

The equations above allow us to compute some measurable quantities that could be used for possible detection of high frequency gravitational waves. The presence of the ohmic losses by the induced electric fields $\vec{j}_{\text{loss}} = \sigma \vec{E^{(1)}}$ in the 4-current effective density will slightly modify the form of the above equations. Using the Maxwell equation (2.1.9) we obtain

$$\frac{1}{c^2}\frac{\partial^2 \vec{E^{(1)}}}{\partial t^2} + \sigma\mu_0 \frac{\partial \vec{E^{(1)}}}{\partial t} - \vec{\Delta} \vec{E^{(1)}} = -\left(\frac{1}{\varepsilon_0}\vec{\nabla}\rho^{\text{eff}} + \mu_0 \frac{\partial \vec{j^{\text{eff}}}}{\partial t}\right), \quad (3.1.10)$$

$$\frac{1}{c^2}\frac{\partial^2 \vec{B^{(1)}}}{\partial t^2} + \sigma\mu_0 \frac{\partial \vec{B^{(1)}}}{\partial t} - \vec{\Delta} \vec{B^{(1)}} = \mu_0 \vec{\nabla} \times \vec{j^{\text{eff}}}. \quad (3.1.11)$$

Please remind here that the equations above are considered in vacuum. The propagation in a specific material must be discussed with the relative electric permittivity and magnetic permeability.

3.2 Computing the cavity response

In the previous section, we showed that the induced electromagnetic field due to the passing of a gravitational wave is the solution of equations (3.1.10) and (3.1.11). If we solve this in any point of our spacetime, we get the electromagnetic field in any point in the detector and at any moment. However, solving it is quite challenging. Since we use perturbative methods, maybe there is a simple solution at leading order that can be found. Moreover, despite the fact that getting the full electromagnetic field could be useful, computing physical quantities that can be detected must be the main goal of our study.

The first physical quantity than we consider is the electromagnetic energy stored inside the cavity in vacuum, defined by

$$\mathscr{E} = \frac{1}{2}\int_V \left(\varepsilon_0 \|\vec{E}\|^2 + \frac{1}{\mu_0}\|\vec{B}\|^2\right) dV, \quad (3.2.1)$$

where $\|\cdot\|$ denotes the Euclidean norm. Before the passing of the incoming gravitational wave, the electromagnetic energy is

$$\mathscr{E}_0 = \frac{1}{2\mu_0}\int_V \|\vec{B^{(0)}}\|^2 dV, \quad (3.2.2)$$

and when the induced electromagnetic fields appear through the inverse Gertsenshtein effect when a gravitational wave passes, the electromagnetic energy restricted to the

first order of perturbation is

$$\mathscr{E}(t) \simeq \frac{1}{2\mu_0}\int_V \left(\|\vec{B^{(0)}}\|^2 + 2\vec{B^{(0)}}\cdot\vec{B^{(1)}}\right) dV, \tag{3.2.3}$$

where $\cdot$ denotes the scalar product. From equations (3.2.2) and (3.2.3), we can express the energy variation at time t by

$$\Delta\mathscr{E}(t) = \mathscr{E}(t) - \mathscr{E}_0 = \frac{1}{\mu_0}\int_V \vec{B^{(0)}}\cdot\vec{B^{(1)}} dV. \tag{3.2.4}$$

If we made the hypothesis that the external constant magnetic field is aligned with the X-axis, $\vec{B^{(0)}} = B_0\vec{e_x}$, the energy variation equation (3.2.4) becomes

$$\Delta\mathscr{E}(t) = \frac{B_0}{\mu_0}\int_V B_x^{(1)} dV. \tag{3.2.5}$$

Thus, we only need to solve the x-component of the induced magnetic field to compute the energy variation at first order. Instead of this quantity, we can simply express the induced electromagnetic power in the cavity, as in axion electromagnetic detection [Asztalos et al., 2010]. The induced power in the cavity is given by

$$\mathscr{P}(t) = \frac{d\mathscr{E}}{dt} = \frac{d\left(\mathscr{E}_0 + \Delta\mathscr{E}\right)}{dt} = \frac{d\Delta\mathscr{E}}{dt} = \frac{B_0}{\mu_0}\int_V \frac{dB_x^{(1)}}{dt} dV. \tag{3.2.6}$$

Equation (3.2.6) provides an interesting physical quantity that could be detectable with electromagnetic techniques. This quantity is also a first order computation so it would be the leading order of the induced electromagnetic power.

Equation (3.2.6) above is very interesting as it provides the time evolution of the induced power, but another point of interest is how the induced power evolves with the frequency. It is done through the use of the temporal Fourier transform, that we can apply to any time-dependent function $f(t)$, and obtain the temporal Fourier transform

$$\tilde{f}(\omega) = \int_{-\infty}^{\infty} f(t) e^{-i\omega t} dt, \tag{3.2.7}$$

that depends on $\omega = 2\pi\nu$ where ν is the frequency. An important property of the Fourier transform is that it transform temporal derivatives into algebraic products,

$$i\omega\tilde{f}(\omega) = \int_{-\infty}^{\infty} \left[\frac{df}{dt}(t)\right] e^{-i\omega t} dt, \tag{3.2.8}$$

We can thus obtain the frequency-dependent induced power, the temporal Fourier transform of $\mathscr{P}(t)$,

$$\tilde{\mathscr{P}}(\omega) = \frac{iB_0\omega}{\mu_0}\int_V \tilde{B}_x^{(1)} dV, \tag{3.2.9}$$

where $\tilde{B}_x^{(1)}$ is the temporal Fourier transform of $B_x^{(1)}$. Now that we have the observable that we want to focus on, the response of our detector, we need to solve the x-component of our induced magnetic field $B_x^{(1)}$. We could numerically solve equation (3.1.9) with proper boundary conditions that respects the constraints put by the cavities (3.1.1), but since equation (3.2.6) contains a volume integral, some spatially oscillating quantities will vanish in this integral, and could generate numerical errors and the computation time could be quite long to obtain accurate solutions. We suggest to solve the equations in a more clever way, by using the cylindrical harmonics in our cavities.

3.3 Cylindrical harmonics decomposition

Since we need to solve our wave equation (3.1.11) in cylindrical cavities, we will decompose our field in cylindrical harmonics. Mathematically, these are the eigenfunctions of the vectorial Laplacian operator $\vec{\Delta}$ that satisfy our boundary conditions (3.1.1), and their eigenvalues are the resonance frequencies of our cavities. These harmonics are often denoted by "quantum" numbers, that are separation constants arising from solving the Helmholtz equation by variable separation.

In the case of our detector, let us use the cylindrical coordinates (r,θ,z). The eigenfunctions of the Laplacian operator that satisfy our boundary conditions (3.1.1) are

$$\psi^r_{kmn} = C^r_{kmn}\cdot\frac{\mathscr{R}_{km}(r)}{mr}\cdot\begin{Bmatrix}\cos\\ \sin\end{Bmatrix}(m\theta)\cdot\begin{Bmatrix}\cos\\ \sin\end{Bmatrix}\left(\frac{2\pi nz}{L}\right) \tag{3.3.1}$$

$$\psi^\theta_{kmn} = C^\theta_{kmn}\cdot\frac{d\mathscr{R}_{km}(r)}{dr}\cdot\begin{Bmatrix}-\sin\\ \cos\end{Bmatrix}(m\theta)\cdot\begin{Bmatrix}\cos\\ \sin\end{Bmatrix}\left(\frac{2\pi nz}{L}\right) \tag{3.3.2}$$

$$\psi^z_{kmn} = C^z_{kmn}\cdot\mathscr{R}_{km}(r)\cdot\begin{Bmatrix}\cos\\ \sin\end{Bmatrix}(m\theta)\cdot\begin{Bmatrix}\sin\\ \cos\end{Bmatrix}\left(\frac{2\pi nz}{L}\right), \tag{3.3.3}$$

where k,m,n are integers that appear when using the variable separation method. These are "quantum" numbers to differentiate each harmonic. $C^{r,\theta,z}_{kmn}$ are normalization

constants and L is the length of the cavity defined earlier. The two lines containing functions in brackets describe the choice of mathematically possible orthogonal eigenfunction of the Laplacian operator. The discussion about the cavity modes is made in Appendix C. For the hollow cylinder, the TM cavity, the radial functions $\mathscr{R}_{km}(r)$ are

$$\mathscr{R}_{km} = J_m(\alpha_k r), \tag{3.3.4}$$

where J_m is the Bessel function of first kind and the constants α_k are solutions of

$$J_m(\alpha_k R) \quad = \quad 0 \ \forall k \in \mathbb{Z}, \tag{3.3.5}$$

so α_k is k^{th} root of the Bessel function J_m.

In the case of the coaxial TEM waveguide the radial functions are

$$\mathscr{R}_{km} \quad = \quad A_k J_m(\alpha_k r) + Y_m(\alpha_k r), \tag{3.3.6}$$

where the constants α_k and A_K are the solutions of

$$A_k J_m(\alpha_k R_1) + Y_m(\alpha_k R_1) \quad = \quad 0 \ \forall k \in \mathbb{Z}, \tag{3.3.7}$$

$$A_k J_m(\alpha_k R_2) + Y_m(\alpha_k R_2) \quad = \quad 0 \ \forall k \in \mathbb{Z}. \tag{3.3.8}$$

The cylindrical harmonics are a powerful tool for wave equation solving. Indeed, these functions satisfy the Helmholtz equation,

$$\vec{\Delta}\vec{\psi}_{kmn} = -\Omega_{kmn}^2 \vec{\psi}_{kmn}, \tag{3.3.9}$$

where

$$\Omega_{kmn}^2 = \alpha_k^2 + \frac{4\pi^2 n^2}{L^2} \tag{3.3.10}$$

are the squared-norm of the resonant modes wavevectors.

Since these functions $\vec{\psi}_{kmn}$ form an orthonormal basis, we can expand our induced field $\vec{B^{(1)}}$ and the source term of equation (3.1.11) as

$$B^{(1)r,\theta,z}(t,\vec{r}) = \sum_{k,m,n} \hat{b}^{r,\theta,z}_{kmn}(t)\psi^{r,\theta,z}_{kmn}(\vec{r}), \tag{3.3.11}$$

$$\mu_0\left(\vec{\nabla}\times\vec{j^{\text{eff}}}\right)^{r,\theta,z}(t,\vec{r}) = \sum_{k,m,n} \hat{s}^{r,\theta,z}_{kmn}(t)\psi^{r,\theta,z}_{kmn}(\vec{r}), \tag{3.3.12}$$

where the upper indices r,θ,z denotes the components of the fields in the cylindrical coordinates. With these expansions above, using Helmholtz equation (3.3.9) into equation (3.1.11), we obtain

$$\sum_{k,m,n}\frac{1}{c^2}\frac{d^2\hat{b}^{r,\theta,z}_{kmn}}{dt^2}\psi^{r,\theta,z}_{kmn}+\sum_{k,m,n}\sigma\mu_0\frac{d\hat{b}^{r,\theta,z}_{kmn}}{dt}\psi^{r,\theta,z}_{kmn}+\sum_{k,m,n}\Omega^2_{kmn}\hat{b}^{r,\theta,z}_{kmn}\psi^{r,\theta,z}_{kmn}=\sum_{k,m,n}\hat{s}^{r,\theta,z}_{kmn}(t)\psi^{r,\theta,z}_{kmn}. \tag{3.3.13}$$

We consider as [Grishchuk, 1977] that the dissipation in the cavity has an effective conductivity for each mode $\sigma=\frac{c\Omega_{kmn}\varepsilon_0}{Q}$, where Q is the cavity quality factor. With this assumption, by gathering the sums, we obtain for each term (k,m,n)

$$\frac{1}{c^2}\frac{d^2\hat{b}^{r,\theta,z}_{kmn}}{dt^2}+\frac{\Omega_{kmn}}{cQ}\frac{d\hat{b}^{r,\theta,z}_{kmn}}{dt}+\Omega^2_{kmn}\hat{b}^{r,\theta,z}_{kmn}=\hat{s}^{r,\theta,z}_{kmn} \tag{3.3.14}$$

which is a forced and damped harmonic oscillator equation for each coefficient $\hat{b}^{r,\theta,z}_{kmn}$. The forcing term is $\hat{s}^{r,\theta,z}_{kmn}$ and can be computed by projecting the original source term of equation (3.1.11) on the eigenfunctions of the Laplacian $\vec{\psi}_{kmn}$,

$$\hat{s}^{r,\theta,z}_{kmn}(t)=\int_V \mu_0\left(\vec{\nabla}\times\vec{j^{\text{eff}}}(t,\vec{r})\right)^{r,\theta,z}\psi^{r,\theta,z}_{kmn}(\vec{r})dV, \tag{3.3.15}$$

where we use the scalar product of two functions f and g,

$$(f,g)=\int_V f(\vec{r})g^*(\vec{r})dV, \tag{3.3.16}$$

to make the orthogonal projection. That means that if we want to solve equation (3.1.11), we need to solve (3.3.14) sourced by equation (3.3.15). We thus retrieve the induced field by equation (3.3.11). The equation (3.3.14) can also be put in the temporal

Fourier domain, and becomes a pure algebraic equation,

$$-\frac{\omega^2}{c^2}\tilde{b}^{r,\theta,z}_{kmn}+\frac{i\omega\Omega_{kmn}}{cQ}\tilde{b}^{r,\theta,z}_{kmn}+\Omega^2_{kmn}\tilde{b}^{r,\theta,z}_{kmn}=\tilde{s}^{r,\theta,z}_{kmn} \tag{3.3.17}$$

where $\tilde{b}^{r,\theta,z}_{kmn}$ is the temporal Fourier transform of $\hat{b}^{r,\theta,z}_{kmn}$, and

$$\tilde{s}^{r,\theta,z}_{kmn}(\omega)=\int_V \mu_0\left(\vec{\nabla}\times\vec{\mathscr{F}}^{\text{eff}}(\omega,\vec{r})\right)^{r,\theta,z}\psi^{r,\theta,z}_{kmn}(\vec{r})dV, \tag{3.3.18}$$

where $\vec{\mathscr{F}}^{\text{eff}}(\omega,\vec{r})$ is the temporal Fourier transform of $\vec{j^{\text{eff}}}(t,\vec{r})$. This can be made because the temporal and the spatial variables in our effective current density are independent.

The same analytic treatment can be made to solve equation (3.1.10). Nevertheless, we found out a measurable quantity that we defined in equation (3.2.6), which only includes the induced magnetic field $\vec{B^{(1)}}$. This is why we focused on equation (3.1.11). Let us take back the response of our detector equation (3.2.6), which contains the x-component of $\vec{B^{(1)}}$, because our external constant magnetic field is along the X-axis. Thus, since our eigenfunctions $\psi^{r,\theta,z}_{kmn}$ are defined in cylindrical coordinates of the proper detector frame, we can decompose the x-component of $\vec{B^{(1)}}$ as

$$B^{(1)}_x=B^{(1)}_r\cos\theta-B^{(1)}_\theta\sin\theta \tag{3.3.19}$$

in order to rewrite equation (3.2.6) as

$$\mathscr{P}(t)=\frac{B_0}{\mu_0}\int_V\left(\frac{dB^{(1)}_r}{dt}\cos\theta-\frac{dB^{(1)}_\phi}{dt}\sin\theta\right)dV, \tag{3.3.20}$$

and with the decomposition (3.3.11) we obtain

$$\mathscr{P}(t)=\frac{B_0}{\mu_0}\sum_{k,m,n}\int_{0,R_1}^{R,R_2}\int_0^{2\pi}\int_{-\frac{L}{2}}^{\frac{L}{2}}\left(\frac{d\hat{b}^r_{kmn}}{dt}\psi^r_{kmn}\cos\theta-\frac{d\hat{b}^\phi_{kmn}}{dt}\psi^\theta_{kmn}\sin\theta\right)r\,dr\,d\theta\,dz \tag{3.3.21}$$

where the limits on the integral over r depend on the considered cavity. If we take back the expressions of the eigenfunctions (3.3.1) and (3.3.2), only the eigenfuctions independent of z do not vanish in the integral above. If we look at the θ dependence, only

$\psi^r_{kmn} \propto \cos\theta$ and $\psi^\theta_{kmn} \propto \sin\theta$ lead to non-vanishing volume integral. In other words, only the $(k,1,0)$ modes do not vanish in the volume integral in equation (3.3.21), leading to

$$\mathscr{P}(t) = \frac{\pi B_0}{\mu_0} \sum_k \left(\frac{d\hat{b}^r_{k10}}{dt} I^r_k + \frac{d\hat{b}^\theta_{k10}}{dt} I^\theta_k \right), \tag{3.3.22}$$

where we can define the quantities

$$I^r_k = \int_{0,R_1}^{R,R_2} R_{k1}(r)dr, \tag{3.3.23}$$

$$I^\theta_k = \int_{0,R_1}^{R,R_2} \frac{dR_{k1}(r)}{dr} r\,dr. \tag{3.3.24}$$

We can easily compute from Bessel functions properties that $I^r_k = -I^\theta_k \stackrel{\text{def}}{=} I_k$, we can thus rewrite equation (3.3.22) as

$$\mathscr{P}(t) = \frac{\pi B_0}{\mu_0} \sum_k I_k \left(\frac{d\hat{b}^r_{k10}}{dt} - \frac{d\hat{b}^\theta_{k10}}{dt} \right). \tag{3.3.25}$$

We consider

$$\left(\vec{\nabla} \times \vec{j^{\text{eff}}}\right)^r = \left(\vec{\nabla} \times \vec{j^{\text{eff}}}\right)^x \cos\theta + \left(\vec{\nabla} \times \vec{j^{\text{eff}}}\right)^y \sin\theta, \tag{3.3.26}$$

$$\left(\vec{\nabla} \times \vec{j^{\text{eff}}}\right)^\theta = -\left(\vec{\nabla} \times \vec{j^{\text{eff}}}\right)^x \sin\theta + \left(\vec{\nabla} \times \vec{j^{\text{eff}}}\right)^y \cos\theta, \tag{3.3.27}$$

and the fact that only the $(k,1,0)$ modes where eigenfunctions $\psi^r_{kmn} \propto \cos\theta$ and $\psi^\theta_{kmn} \propto \sin\theta$ do not vanish in the volume integral of equation (3.3.15). We also assume a plane wave approximation along the Z-axis, so our source term $\left(\vec{\nabla} \times \vec{j^{\text{eff}}}\right)$ depends spatially only on z. We can rewrite the source term of our harmonic oscillator equation defined by (3.3.15), with all the hypotheses described above,

$$\tilde{s}^{r,\theta}_{k10}(t) = \pi I^{r,\theta}_k \int_{-\frac{L}{2}}^{\frac{L}{2}} \mu_0 \left(\vec{\nabla} \times \vec{j^{\text{eff}}}(t,z)\right)^x dz, \tag{3.3.28}$$

or in the frequency domain

$$\tilde{s}_{k10}(\omega) = \pi I^{r,\theta}_k \int_{-\frac{L}{2}}^{\frac{L}{2}} \mu_0 \left(\vec{\nabla} \times \vec{\mathscr{J}^{\text{eff}}}(\omega,z)\right)^x dz, \tag{3.3.29}$$

which are a very convenient way to compute them. Here again $I_k^r = -I_k^\theta \overset{\text{def}}{=} I_k$ implies that $\hat{s}_{k10}^r(t) = -\hat{s}_{k10}^\theta(t) \overset{\text{def}}{=} \hat{s}_{k10}(t)$, so the solution of equation (3.3.14) for the $(k,1,0)$ mode will be $\hat{b}_{k10}^r(t) = -\hat{b}_{k10}^\theta(t) \overset{\text{def}}{=} \hat{b}_{k10}(t)$. Equation (3.3.25) can be rewritten in a simpler way

$$\mathscr{P}(t) = \frac{2\pi B_0}{\mu_0} \sum_k I_k \frac{d\hat{b}_{k10}}{dt}(t). \tag{3.3.30}$$

Equation (3.3.30) can be transferred to the temporal Fourier domain in order to get the induced power depending on the frequency using equation (3.2.8),

$$\tilde{\mathscr{P}}(\omega) = \frac{2i\pi\omega B_0}{\mu_0} \sum_k I_k \tilde{b}_{k10}(\omega). \tag{3.3.31}$$

We can now quite easily compute the induced electromagnetic power in our detectors evolving with time or frequency thanks to equations (3.3.30) and (3.3.31). Now we need to investigate the source term of our oscillator equations given by equations (3.3.28) and (3.3.29), that we can also simplify in

$$\hat{s}_{k10}(t) = \pi I_k \int_{-\frac{L}{2}}^{\frac{L}{2}} \mu_0 \left(\vec{\nabla} \times \vec{j^{\text{eff}}}(t,z)\right)^x dz, \tag{3.3.32}$$

or in the frequency domain

$$\tilde{s}_{k10}(\omega) = \pi I_k \int_{-\frac{L}{2}}^{\frac{L}{2}} \mu_0 \left(\vec{\nabla} \times \vec{\mathscr{J}}^{\text{eff}}(\omega,z)\right)^x dz, \tag{3.3.33}$$

3.4 The source term

In equations (3.3.32) and (3.3.33), because our external magnetic field is along the X-axis, we only need to get the x-component of the curl of the effective current density in order to obtain the source terms of our harmonic oscillator, useful to obtain the induced electromagnetic power in the cavity. In Cartesian coordinates, we have that

$$\mu_0 \left(\vec{\nabla} \times \vec{j^{\text{eff}}}\right)^x = \mu_0 \left(\partial_y j_{\text{eff}}^z - \partial_z j_{\text{eff}}^y\right). \tag{3.4.1}$$

In this section, we are going to investigate mathematically what is the form of equation (3.4.1), first in the TT gauge, to first analyze the case where the equations are

simplified in order to consider a more realistic case, where the detection process is described in the proper detector frame. In both cases, we are going to consider that the direction of propagation of our incoming gravitational wave is the symmetry axis of our cavities, the Z-axis.

3.4.1 TT frame

We first consider a detection of gravitational waves in the TT frame even though it is not realistic. Indeed, modeling a constant external magnetic field in the TT frame is not very feasible because we saw in the first chapter that the TT coordinates stretch themselves when a gravitational wave passes. Such a constant magnetic field in that frame will oscillate in the laboratory frame and vice-versa. However, it is useful to first consider this TT frame to get used to the equations with simpler expressions before analyzing the proper detector frame. For a gravitational wave in the TT frame, propagating along the Z-axis, the perturbation tensor $h_{\mu\nu}$ satisfies conditions (1.1.18), and has the form

$$h_{\mu\nu} = \begin{pmatrix} 0 & 0 & 0 & 0 \\ 0 & h_+(z,t) & h_\times(z,t) & 0 \\ 0 & h_\times(z,t) & -h_+(z,t) & 0 \\ 0 & 0 & 0 & 0 \end{pmatrix}. \tag{3.4.2}$$

With this kind of metric perturbation, the terms $\vec{j_2}$ and $\vec{j_3}$ defined by equations (3.1.5) and (3.1.6) vanish due respectively to the Lorenz gauge condition $\partial_\mu h^{\mu\nu} = 0$ and the traceless perturbation $h = 0$. The effective current in this case is

$$\vec{j_{\text{eff}}} = \vec{j_1} = \frac{B_0}{\mu_0} \begin{pmatrix} -\partial_z h_\times \\ \partial_z h_+ \\ 0 \end{pmatrix}, \tag{3.4.3}$$

where we used equation (3.1.4) to compute the components. We can see that the effective current has a very simple expression. Putting this effective current in equation (3.4.1), we obtain a source term that is

$$\mu_0 \left(\vec{\nabla} \times \vec{j^{\text{eff}}} \right)^x = -B_0 \frac{\partial^2 h_+}{\partial z^2} \tag{3.4.4}$$

which is again a very simple term for analysis. We can see that the response of our cavity will contain only information of the + polarization since we boost the x-component

of the induced field, boosting the y-component gives us information about the $\times$ polarization. The source term of our magnetic field wave equation only spatially depends on the z-coordinate. We can use the equation (3.3.32) to get the source term of the harmonic oscillator equation (3.3.14), which leads to

$$\hat{s}_{k10}(t) = -\pi B_0 I_k \int_{-\frac{L}{2}}^{\frac{L}{2}} \frac{\partial^2 h_+}{\partial z^2}(z,t)\, dz. \tag{3.4.5}$$

If we assume that the gravitational wave is a plane wave propagating in the negative z-direction, $h_+(z,t) = h_+(t+\frac{z}{c})$ and make the variable change $t' = t + \frac{z}{c}$ for the integral we obtain

$$\begin{aligned} \hat{s}_{k10}(t) &= -\frac{\pi B_0 I_k}{c} \int_{t-\frac{L}{2c}}^{t+\frac{L}{2c}} \frac{\partial^2 h_+}{\partial t'^2}(t')dt' \\ &= -\frac{\pi B_0 I_k}{c} \left(\frac{\partial h_+}{\partial t}(t+\frac{L}{2c}) - \frac{\partial h_+}{\partial t}(t-\frac{L}{2c}) \right). \end{aligned} \tag{3.4.6}$$

Here is how we can compute our forcing term of the harmonic oscillator equation. We can also easily compute the Fourier transform of this expression. If we recall equation (3.2.8) and

$$e^{-i\omega t_0}\tilde{f}(\omega) = \int_{-\infty}^{\infty} f(t-t_0)e^{-i\omega t}dt, \tag{3.4.7}$$

we have that

$$\begin{aligned} \int_{-\infty}^{\infty} \left(\frac{\partial h_+}{\partial t}(t+\frac{L}{2c}) - \frac{\partial h_+}{\partial t}(t-\frac{L}{2c}) \right) e^{-i\omega t}dt &= i\omega\tilde{h}_+(\omega)\left(e^{-i\omega\frac{L}{2c}} - e^{i\omega\frac{L}{2c}} \right) \\ &= -2\omega\tilde{h}_+(\omega)\sin\left(\frac{\omega L}{2c}\right). \end{aligned} \tag{3.4.8}$$

We thus obtain straightforwardly the temporal Fourier transform of our source term

$$\tilde{s}_{k10}(\omega) = \frac{2\pi\omega B_0 I_k}{c}\tilde{h}_+(\omega)\sin\left(\frac{\omega L}{2c}\right). \tag{3.4.9}$$

We have now everything to solve the harmonic oscillator equation to get the induced power in our cavity, computed in the TT gauge. We perform the same computations in the proper detector frame in the following, that will lead to far more complicated expressions, but the next section will show how to cope with that.

3.4.2 The proper detector frame

In this frame, we saw earlier that the incoming gravitational wave $h_{\mu\nu}(\vec{r},t)$ is given by equations (1.3.8) to (1.3.17). We also know that the Lorenz gauge condition does not hold and the effective current for our magnetic field wave equation is

$$\vec{j_{\text{eff}}} = \vec{j_1} + \vec{j_2} + \vec{j_3} \tag{3.4.10}$$

where

$$\vec{j_1} = \frac{B_0}{\mu_0}\begin{pmatrix} -\partial_z P_\times - \frac{P_\times}{z} \\ \partial_z P_+ + \frac{P_+}{z} \\ \frac{yP_+ - xP_\times}{z^2} + \frac{y\partial_z P_+ - x\partial_z P_\times}{z} \end{pmatrix}, \tag{3.4.11}$$

$$\vec{j_2} = \frac{B_0}{\mu_0}\begin{pmatrix} 0 \\ \frac{2\left(x^2-y^2\right)P_+ + 4xyP_\times}{z^3} - \frac{\left(x^2-y^2\right)(\partial_z P_+ - \partial_{ct} Q_+) + 2xy(\partial_z P_\times - \partial_{ct} Q_\times)}{z^2} \\ -\frac{yP_+ - xP_\times}{z^2} - \frac{x(\partial_z P_\times - \partial_{ct} Q_\times) - y(\partial_z P_+ - \partial_{ct} Q_+)}{z} \end{pmatrix}, \tag{3.4.12}$$

$$\vec{j_3} = \frac{B_0}{2\mu_0}\begin{pmatrix} 0 \\ \partial_z h \\ -\partial_y h \end{pmatrix} \text{ with } h = \frac{2\left(x^2-y^2\right)(P_+ - Q_+) + 4xy(P_\times - Q_\times)}{z^2}. \tag{3.4.13}$$

You can see obviously that this effective current is much more complicated than the previous one for the TT gauge (3.4.3), and this current density depends on all the spatial coordinates so it is impossible to use equation (3.3.32) to easily compute the source terms of our harmonic oscillator equations. In order to solve it analytically, we find a practical approximation of the source term that depends only on z and t. The intuition behind this idea, besides equation (3.3.32), is that even if the TT gauge is no longer valid in this case, one can consider the incoming gravitational wave as a plane wave so our source term does not depend on the transverse coordinates (x,y) because the size of the detector is small with respect to the wavefront. Let us now truncate the functions $P_{+,\times}$ and $Q_{+,\times}$ to the first term of the sums defined in equations (1.3.18) and (1.3.19), which leads to

$$P_{+,\times}(z,t) \approx \frac{z^2}{6}\frac{1}{c^2}\frac{d^2 h_{+,\times}}{dt^2}, \tag{3.4.14}$$

$$Q_{+,\times}(z,t) \approx \frac{z^2}{3}\frac{1}{c^2}\frac{d^2 h_{+,\times}}{dt^2}. \tag{3.4.15}$$

Using these approximations, we obtain for the following source term for our wave equation

$$\mu_0 \left(\vec{\nabla} \times \vec{j}_1\right)^x = -B_0 \frac{1}{c^2} \frac{d^2 h_+}{dt^2}, \tag{3.4.16}$$

$$\mu_0 \left(\vec{\nabla} \times \vec{j}_2\right)^x = \frac{B_0}{6} \frac{1}{c^2} \frac{d^2 h_+}{dt^2} - \frac{B_0 z}{3} \frac{1}{c^3} \frac{d^3 h_+}{dt^3}, \tag{3.4.17}$$

$$\mu_0 \left(\vec{\nabla} \times \vec{j}_3\right)^x = -\frac{B_0}{3} \frac{1}{c^2} \frac{d^2 h_+}{dt^2}. \tag{3.4.18}$$

If we neglect the term in $\frac{1}{c^3}$ we find out that

$$\mu_0 \left(\vec{\nabla} \times \vec{j_{\text{eff}}}\right)^x = -\frac{7B_0}{6} \frac{1}{c^2} \frac{d^2 h_+}{dt^2} = \frac{7}{6} \mu_0 \left(\vec{\nabla} \times \vec{j}_1\right)^x. \tag{3.4.19}$$

That means that we can approximate the source term by using the definition of $\vec{j}_1$,

$$\mu_0 \left(\vec{\nabla} \times \vec{j_{\text{eff}}}\right)^x \approx \frac{7}{6} \mu_0 \left(\vec{\nabla} \times \vec{j}_1\right)^x = -\frac{7B_0}{6} \left(\frac{\partial^2 P_+}{\partial z^2} + \frac{2}{z} \frac{\partial P_+}{\partial z}\right). \tag{3.4.20}$$

The approximation (3.4.20) can be validated computationally if we implement the sum involved in $P_{+,\times}$ and $Q_{+,\times}$ in symbolic math software. We check the accuracy of this approximation in figure 3.2. On the top, the blue curve represents the L^2-norm of the source term for a slice at several values of z (in meters), integrated over a unit disk for the x and y coordinates. The orange curve is the same computation for the approximation equation (3.4.20). The bottom panel is the source term in the detector frame divided by the source term in the TT gauge to validate equation (3.4.20). The signal considered here is the Newtonian GW inspiral phase of primordial black hole mergers ($10^{-5} M_\odot$), given by equations (1.2.22) and (1.2.23). The number of terms considered in Eqs. (1.3.18,1.3.19) are $n = 10$. Please note that we have to use geometric units in order to avoid numerical errors. The quantities here are transformed in SI units at the end of the simulation. We can see that the approximation becomes less accurate with growing z-coordinate, but keeps the amplitude and frequency of the source terms for cavities that are in order of meters. Otherwise we would consider points far from the reference curve used for the Fermi-Normal coordinates and we need to investigate a better approximation. We use in the following approximation (3.4.20) as our source term in the proper detector frame.

Since the approximation (3.4.20) is valid, we can use the equation (3.3.32) to get the source terms of our harmonic oscillator equations,

$$\begin{aligned}\hat{s}_{k10}(t) &= -\frac{7\pi B_0 I_k}{6}\int_{-\frac{L}{2}}^{\frac{L}{2}}\left(\frac{\partial^2 P_+}{\partial z^2}+\frac{2}{z}\frac{\partial P_+}{\partial z}\right)dz,\\ &= -\frac{7\pi B_0 I_k}{6}\int_{-\frac{L}{2}}^{\frac{L}{2}}\sum_{n=2}^{+\infty}\frac{z^{n-2}}{(n-2)!\,c^n}\frac{\partial^n h_+}{\partial t^n}\,dz,\end{aligned} \tag{3.4.21}$$

where we used the definition of P_+ in equation (1.3.18) to get the second line.

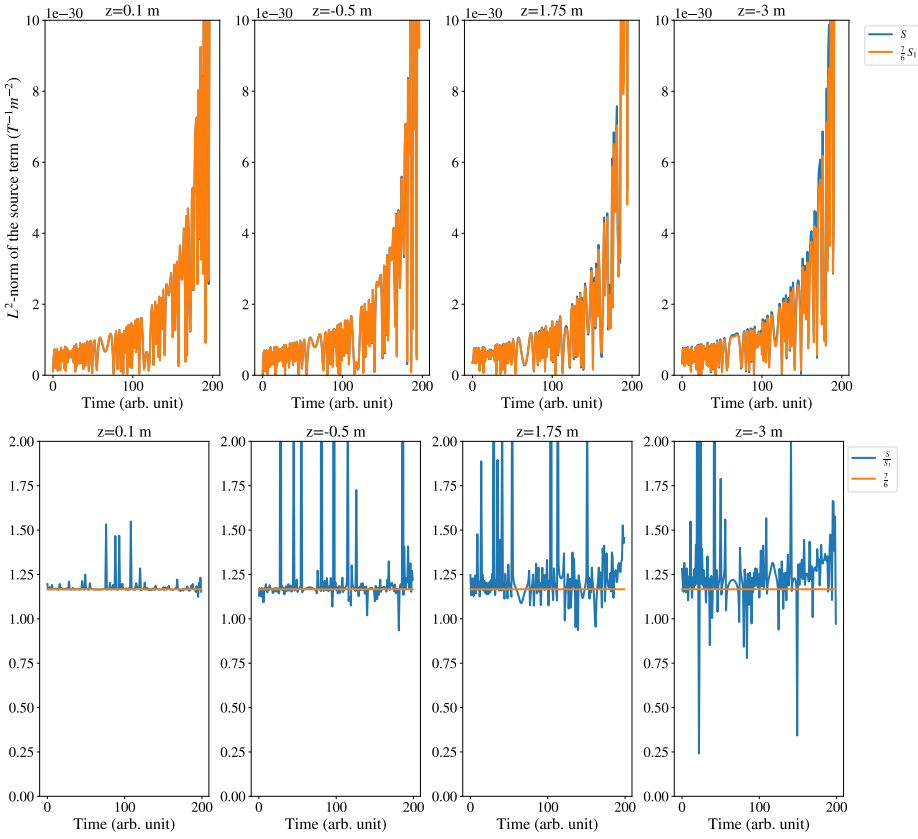

Figure 3.2 – Validation of the approximation Eq. (3.4.20).

If we switch the integral and the series [1] we obtain

$$\hat{s}_{k10}(t) = -\frac{7\pi B_0 I_k}{6} \sum_{n=2}^{+\infty} \frac{1}{(n-1)!\, c^n} \left[\left(\frac{L}{2}\right)^{n-1} - \left(-\frac{L}{2}\right)^{n-1} \right] \frac{\partial^n h_+}{\partial t^n}, \qquad (3.4.22)$$

we can easily compute its temporal Fourier transform to obtain

$$\tilde{s}_{k10}(\omega) = -\frac{7\pi B_0 I_k}{6} \sum_{n=2}^{+\infty} \frac{1}{(n-1)!} \left[\left(\frac{L}{2}\right)^{n-1} - \left(-\frac{L}{2}\right)^{n-1} \right] \left(\frac{i\omega}{c}\right)^n \tilde{h}_+. \qquad (3.4.23)$$

We consider these small algebraic manipulations and sum indices modifications,

$$\begin{aligned} -\sum_{n=2}^{+\infty} \frac{1}{(n-1)!} \left[\left(\frac{L}{2}\right)^{n-1} - \left(-\frac{L}{2}\right)^{n-1} \right] \left(\frac{i\omega}{c}\right)^n &= -\sum_{m=1}^{+\infty} \frac{1}{(2m-1)!} 2 \left(\frac{L}{2}\right)^{2m-1} \left(\frac{i\omega}{c}\right)^{2m} \\ &= 2\frac{\omega}{c} \sum_{m=1}^{+\infty} \frac{(-1)^{m-1}}{(2m-1)!} \left(\frac{L\omega}{2c}\right)^{2m-1} \\ &= 2\frac{\omega}{c} \sum_{p=0}^{+\infty} \frac{(-1)^p}{(2p+1)!} \left(\frac{L\omega}{2c}\right)^{2p+1}. \end{aligned} \qquad (3.4.24)$$

The first line above is valid because only the even n terms of the sum do not vanish. We can thus obtain as source term

$$\tilde{s}_{k10}(\omega) = \frac{7\pi B_0 I_k \omega \tilde{h}_+}{3c} \sum_{p=0}^{+\infty} \frac{(-1)^p}{(2p+1)!} \left(\frac{L\omega}{2c}\right)^{2p+1}, \qquad (3.4.25)$$

where we identify in the sum the Taylor development of a sine function, so we can write

$$\tilde{s}_{k10}(\omega) = \frac{7\pi B_0 I_k \omega \tilde{h}_+}{3c} \sin\left(\frac{\omega L}{2c}\right). \qquad (3.4.26)$$

It means that in the frequency domain, the source terms of our harmonic oscillator equations that contribute to the first order induced electromagnetic power are the same in the TT frame and in the proper detector frame, besides a $\frac{7}{6}$ factor. It will considerably ease the analysis of the detection process of astrophysical gravitational waves.

(1). We can do this if the series converges uniformly, which is the case for values in the assosciated convergence radii because P_+ is computed with Taylor series and the functions are C^∞.

Chapter 4

Numerical Simulations and results

In this chapter, we are going to show numerical simulations from the analytical results we presented in the previous chapter. First, few comments will be given about the implementation of the methods that we summarize in the Appendices A and B. We will then apply those to the primordial black holes merger detection. After that, we will adapt our results to stochastic gravitational background detection in order to study a toy model of this phenomenon. Finally, we will consider the detection sensitivity and compare our work with the literature to conclude this chapter.

4.1 Building a code

To illustrate the analytical computations presented in the previous chapter and apply them to some gravitational wave detections, we build a Python code. We first implement a method to compute the cavity modes, and then, create some functions to model the detection process in the time domain and the frequency domain. We implement also a method to compute our estimation of the RMS induced electromagnetic power generated by a signal. The computations of the cavity modes are explained in Appendix C. The use of adimensional quantities is required in our code in order to avoid numerical errors. Now let us describe our codes.

4.1.1 Time domain simulation

To perform the simulation in the time domain, we start with a plus polarized gravitational wave signal $h_+(t)$, discretized in a set of n discrete points $(t_i, h_i)_{i=1}^n$ where each time point t_i is equally spaced by δt. The inverse of this spacing is the sampling frequency, important in signal analysis. The first step is to compute the source term of the harmonic oscillator equations denoted by

$$\hat{s}_{k10}(t) = -\frac{7\pi B_0 I_k}{6c}\left(\frac{\partial h_+}{\partial t}(t+\frac{L}{2c}) - \frac{\partial h_+}{\partial t}(t-\frac{L}{2c})\right), \tag{4.1.1}$$

explained in Appendix B. Since this equation needs the use of shifted time quantities, we use cubic spline interpolation to compute the derivative of h_+ at the shifted times. After that the computation of $\hat{s}_{k10}$ is straightforward.

The next step is computing the solutions of the harmonic oscillator equations given by

$$\hat{b}_{k10}(t) = e^{-\frac{\alpha_k c}{2Q}t}\left(A_{k10}\cos(\varpi_k t) + B_{k10}\sin(\varpi_k t)\right) + \frac{1}{2\pi}\int_{-\infty}^{\infty} \frac{c^2 \tilde{s}_{k10}(\omega)}{\alpha_k^2 c^2 + \frac{i\omega\alpha_k c}{Q} - \omega^2} e^{i\omega t} d\omega \tag{4.1.2}$$

computed in Appendix B. To use this equation, we obtain $\tilde{s}_{k10}$ by using the Fast Fourier Transform (FFT) algorithm on $\hat{s}_{k10}$. Then, we implement the rest of the solution computation in a subroutine coded in Fortran 90, to increase the performance of the code. This subroutine compute the integral in the particular solution of our harmonic oscillator, then compute the integration constants to get the homogeneous solution. Since we can have a wide range of frequencies in our final solution, we allow to adjust the sampling frequency of our output signal in order to avoid the aliasing due to Shannon theorem. Once these steps performed, we get the derivatives of solutions $\hat{b}_{k10}$ by applying a second order central finite difference method, with forward and backward schemes on the interval's edges. This method allow us to compute the induced electromagnetic power in our cavity by equation (3.3.30). With this signal $\mathscr{P}(t)$ sampled in a set of $\tilde{n}$ points $(t_i, P_i)_{i=1}^{\tilde{n}}$, we can get an estimation of the RMS induced power by computing

$$P_{RMS}^2 = \frac{1}{\tilde{n}}\sum_{i=1}^{\tilde{n}} P_i^2. \tag{4.1.3}$$

4.1.2 Frequency Domain Simulation

To perform the simulation in the frequency domain, we have a signal of plus-polarized gravitational wave $\tilde{h}(\omega)$ discretized in a set of n points $(\omega_i, \tilde{h}_i)_{i=1}^{n}$, each point ω_i is separated by a distance $2\pi\delta\nu$ where $\delta\nu$ is the frequency interval. These computations are easier than in the time domain, because the differential equations become algebraic equations. The source term $\tilde{s}_{k10}$ is computed straightforwardly by equation (3.4.26). Then we can compute the solution of our harmonic equations with

$$\tilde{b}_{k10}(\omega) = \frac{A_{k10} + iB_{k10}}{-\frac{\alpha_k c}{2Q} + i(\omega - \varpi_k)} + \frac{c^2 \tilde{s}_{k10}(\omega)}{c^2\alpha_k^2 + \frac{i\omega\alpha_k c}{Q} - \omega^2} \tag{4.1.4}$$

as obtained in Appendix B. As for the solution in the time domain, we have to take into account of the aliasing phenomenon for further analysis. The sampling frequency of the signal is given by $\frac{\omega_n}{2\pi}$. In the case where the maximal frequency of our signal is lower than our cavity resonance frequencies, we extend the number of frequency points to $\tilde{n}$ to get the end of our frequency interval $\frac{\omega_{\tilde{n}}}{2\pi}$ greater than the last resonance frequency. The space between two frequency points remains the same. Once the $\tilde{s}_{k10}$ computation achieved, we can compute the electromagnetic induced power with equation (3.3.31), in a set of $\tilde{n}$ points $(t_i, \tilde{P}_i)_{i=1}^{\tilde{n}}$. We can also get an estimation of the RMS induced power with

$$P_{RMS}^2 = \frac{1}{\tilde{n}} \sum_{i=1}^{\tilde{n}} \tilde{P}_i^2. \tag{4.1.5}$$

The above estimation is theoretically the same as equation (4.1.3) for $\tilde{n}$ goes to infinity because the Fourier transform is unitary for the $\mathscr{L}^2$ functional norm.

4.1.3 Computing RMS power

In order to compute the RMS induced power estimation obtained in Appendix B,

$$\mathscr{P}_{\mathrm{RMS}}^2 \simeq \int_0^{\infty} |P_{\mathrm{RIR}}(\omega)|^2 |\tilde{h}_+(\omega)|^2 d\omega, \tag{4.1.6}$$

we need to compute the RMS impulse response given by

$$P_{\mathrm{RIR}}(\omega) = \frac{7\sqrt{2}c}{3\mu_0}\pi^2 B_0^2 \omega^2 \left|\sin\left(\frac{\omega L}{2c}\right)\right| \sum_k \frac{(I_k)^2}{\sqrt{\left(\alpha_k^2 c^2 - \omega^2\right)^2 + \left(\frac{\alpha_k \omega c}{2Q}\right)^2}}. \tag{4.1.7}$$

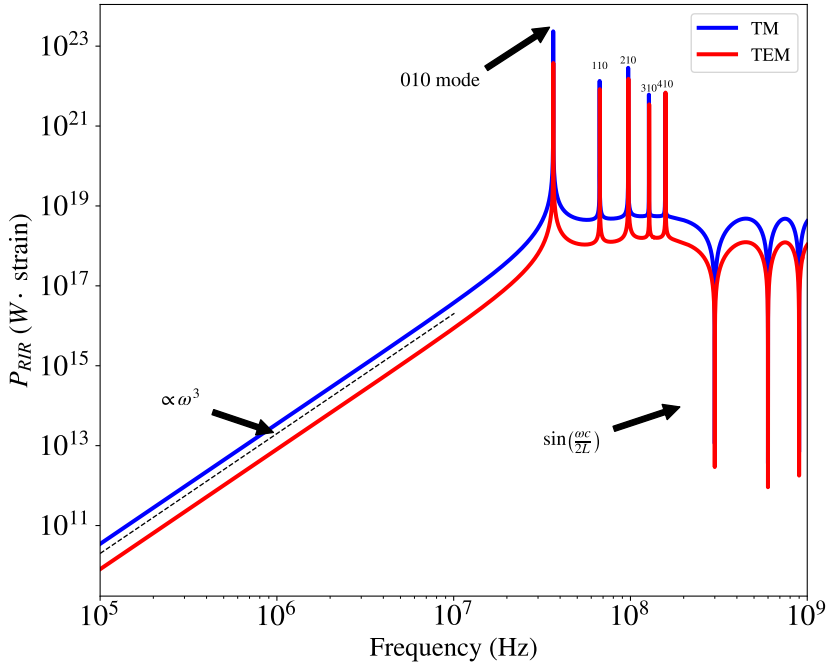

Figure 4.1 – The RMS impulse response for the TM cavity and the TEM waveguide.

Figure 4.1 shows the RMS impulse response for the TM cavity and the one for the TEM waveguide. We chose for parameters an outer radius that is 5m for both, the external magnetic field is 5T and for the TEM waveguide, the inner radius is 10cm. The detectors are 1-meter long and the quality factor is assumed to be 10^5. Those parameters are realistic with the current technology on resonant cavities and intense magnetic field production [Posen et al., 2022].

We can see in (4.1.7) that the response is proportional to ω^3 before the resonance frequency because $\frac{\omega L}{2c} \ll 1$ so $\sin\left(\frac{\omega L}{2c}\right) \approx \frac{\omega L}{2c}$. Then, we have the resonance frequency peaks. The first is the 010 mode, and then we have computed the four following $k10$ modes. The peaks amplitude is lower when k increases. After this resonant peaks zone, we have a constant amplitude response with some big drops due the roots of the $\sin\left(\frac{\omega L}{2c}\right)$ term. Please note that the TEM waveguide curve is slightly below the TM cavity one, this because of the difference of volume due to the inner cylinder.

To compute the estimation of the RMS induced power, we use the expression of P_{RIR} and perform the integral in equation (4.1.6) using Romberg method [Romberg, 1955]. For this kind of detectors of 5m outer radius, we can see that the difference between the TM cavity and the TEM waveguide is not significant. For such a configuration, we are not systematically analyzing both detectors in the following.

Now we have explained the transition of analytical result to the building of a numerical code. We use it in two applications. The first is primordial black hole merger detection and the second one is stochastic gravitational wave background detection.

4.2 Primordial black hole merger detection

The first astrophysical application to simulate the detection of primordial black hole merger. We study first the case of the merger of two black holes of 10^{-5} solar masses ($M_\odot$). This value is chosen because it is in the range of the expected masses for light primordial black hole detection using microlensing techniques [Niikura et al., 2019, Mróz et al., 2017]. Then, we study how our detector reacts with other masses merger signals, in order to set detection limits on the fraction of dark matter we could detect with our methods.

4.2.1 Case of two $10^{-5}M_\odot$ merging black holes

In this section we are going to simulate the detection of two merging $10^{-5}M_\odot$ non-spinning binary black holes, by the devices we presented in this manuscript. We compute the electromagnetic induced power in the cavity using the codes we presented above. But we have to generate the incoming gravitational wave signal.

We use the function `SimInspiralChooseTDWaveform`, coming from the LALsuite library [LIGO Scientific Collaboration, 2018], to get our time-dependent signal $h_+(t)$. The function generate in our case a 4$^{\text{th}}$ post-Newtonian order gravitational waveform of two $10^{-5}M_\odot$ non-spinning merging binary black holes. The signal begins at a frequency $\frac{f_{ISCO}}{25}$ to end at f_{ISCO}. The panel a) of Figure 4.2 shows the signal in function of time and the panel b) its Fourier transform through FFT algorithm for further analysis.

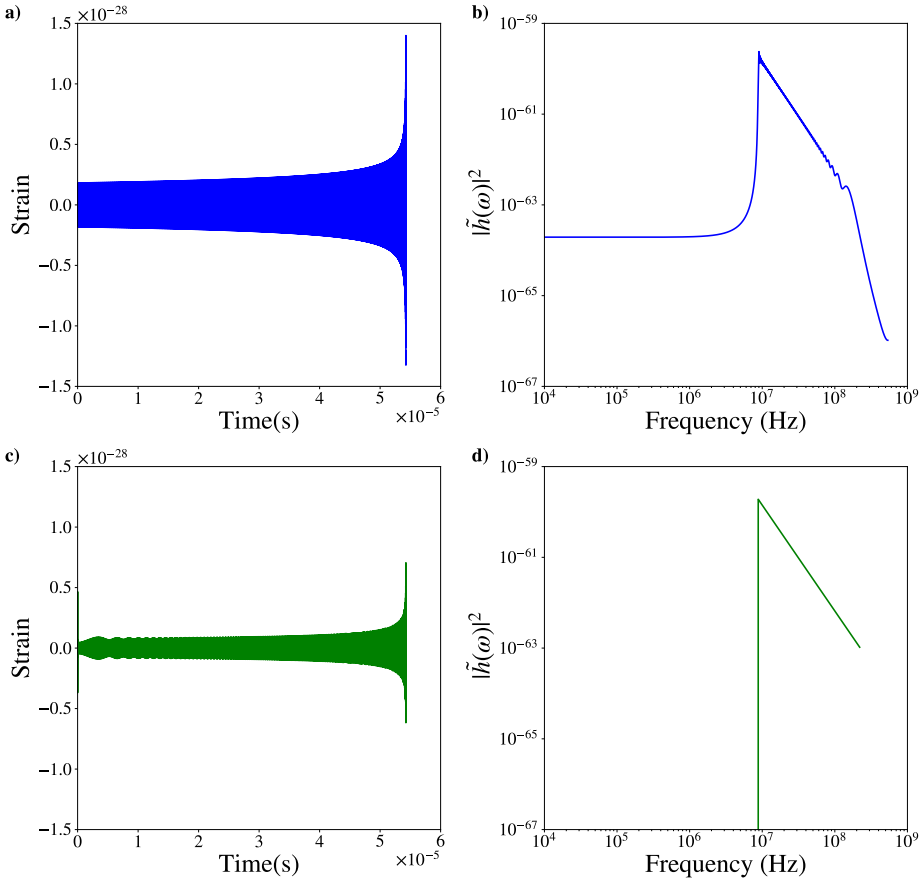

Figure 4.2 – On panel a), the gravitational waveform generated by `SimInspiralChooseTDWaveform` for two $10^{-5}M_{\odot}$ non-spinning merging binary black holes. On panel b) we have its Fourier transform obtained by the FFT algorithm. On the panel d), the one generated by `SimInspiralChooseFDWaveform` for the same parameters, On panel c) we have its inverse Fourier transform obtained by the FFT algorithm.

On the other hand, we can also obtain the frequency-dependent signal $\tilde{h}_+(\omega)$ by using the LALsuite function `SimInspiralChooseFDWaveform`, which compute the same signal as above but in the frequency domain. We show on the panel c) of Figure 4.2 the inverse Fourier transform using FFT and on panel d) the squared module of the frequency-dependent signal $|\tilde{h}_+(\omega)|^2$. We can obviously see if we compare this panel d) with the panel b) of Figure 4.2 that the time-dependent signal computed in the frequency domain with the FFT algorithm presents numerical artifact, the plateau at low frequencies that could provide inaccurate results if we use this numerical Fourier transform. On the other hand we can see that the recombination of the time-dependent with the frequency-dependent one is corrupted by numerical errors. We can thus see the utility to consider time and frequency simulations to provide complementary results, which could be used by wavelets methods for time-frequency analysis

We can present now the results of this detection in the two detectors we modeled. We choose 1-meter long cavities with an outer radius of 5m. The external field is 5T and the inner radius for the TEM waveguide is 10cm. The quality factor Q is assumed to be 10^5. We can see in Figure 4.3 the induced electromagnetic power in the cavities. The results computed in both domains were made with their related method. We can see in the time-domain plots that the amplitude of the induced power is increasing with time and at some point gets a massive boost. This is when the first resonance frequency is triggered. We can see also that the shape of the induced power is similar to the incoming signal, with a big increase in amplitude near the merger. The RMS estimated values are respectively of order $10^{-10}W$ for the time domain code and of order $10^{-11}W$ for the frequency domain code. The frequency domain one must be more accurate because we have the frequency content of an infinite duration signal, which is obviously not the case with the time domain simulation. We can also compute the RMS induced power estimation (4.1.6) where we use equation (1.2.31) to compute $h_+(\omega)$. We obtain RMS induced power estimation of order $10^{-11}W$. This is consistent with the above estimations.

We will compare the two codes one step further with Figure 4.4. On panel a), we plot the time-dependent signal for the induced power coming from the time-domain code in blue. The green curve is the one obtained by the inverse FTT of the frequency-dependent induced power obtained by the frequency-domain code. The increase of amplitude near the merger is still there but the fifty first microseconds of the signal has

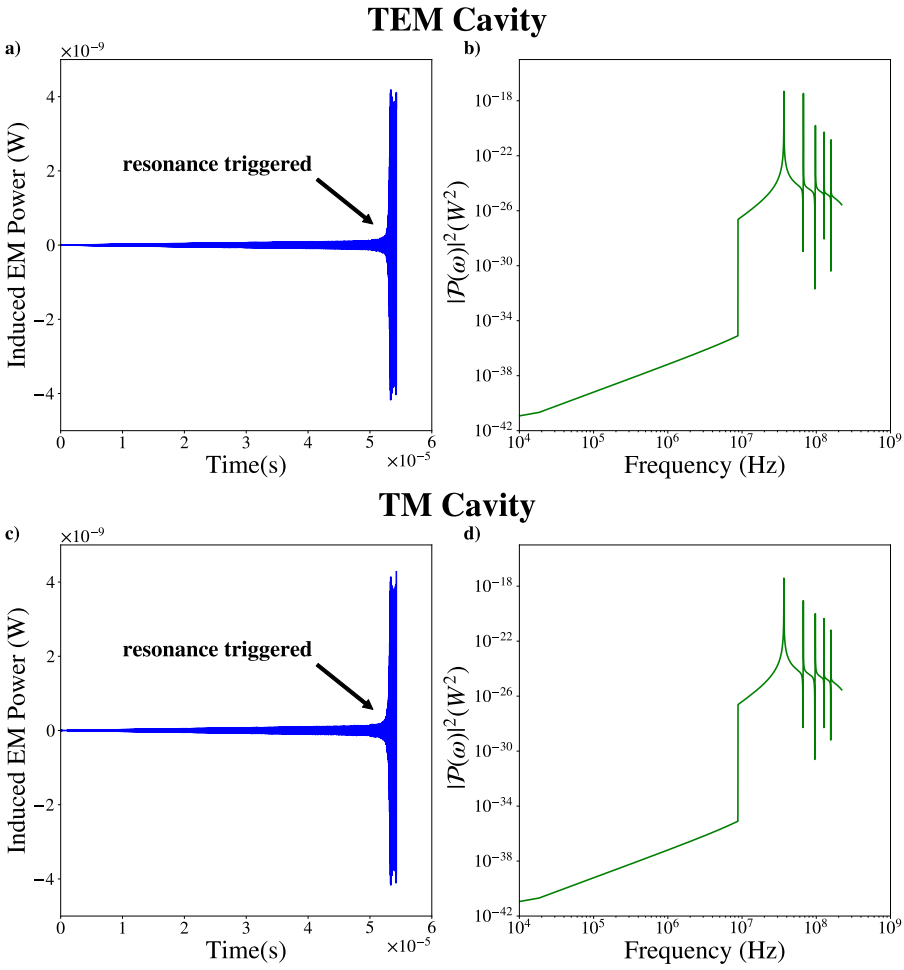

Figure 4.3 – Simulation of the cavity response to the gravitational wave signal of two $10^{-5}M_{\odot}$ non-spinning merging binary black holes. On panel a) we consider the TEM cavity with the time domain code, on panel b) the TEM cavity with the frequency domain code. On panel c) we consider the TM cavity with the time domain code, on panel d) the TM cavity with the frequency domain code.

an amplitude way too high, at least one order of magnitude. This is due to small phase shift when computing the induced electromagnetic power in the frequency domain. The recombination of the Fourier modes fail to decrease as much as expected the amplitude of the signal to match the amplitude of the time-domain signal. On panel b), we can find the squared-module of the frequency-dependent induced power in green and in blue we have the FFT of the time-dependent induced power. We can see that the peaks of the resonance frequencies are also present but their maxima are lower. The main feature that we can notice is that at low frequency the FFT remains constant in the time domain and in the frequency code it decreases monotonically. This leads to some numerical errors when we compute quantities with the time domain code.

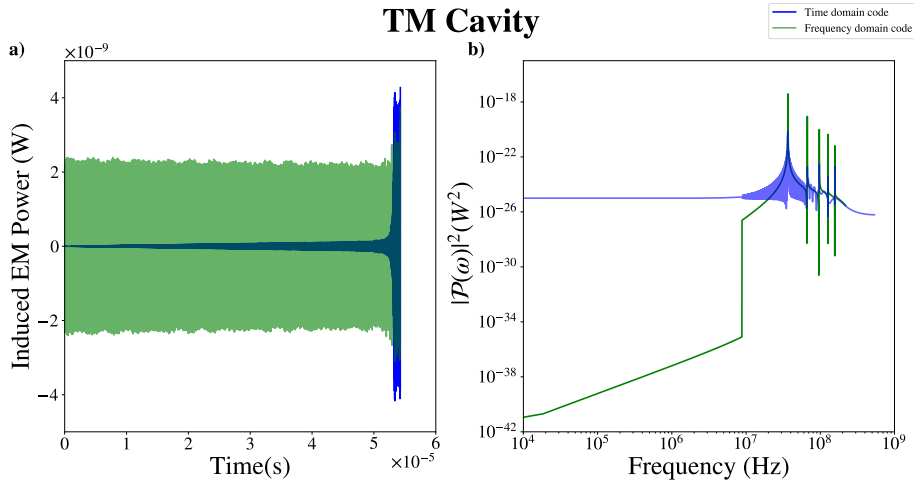

Figure 4.4 – Comparison of the two codes for the simulation of the cavity response to the signal of two $10^{-5}M_{\odot}$ non-spinning merging binary black holes using the TM cavity

The principal limitation of the time-domain simulation is when the incoming signal has a frequency content higher than the resonance frequency band (a case like figure 4.6 below). Since the FFT of such a signal contains a plateau where it should be decreasing, which is a numerical artifact. The computation of the solution (4.1.2) with a numerical Fourier transform will overestimate the solution. The frequency simulation has also some limitations, since it is difficult to access to the duration of the signal, and since the resonant peaks are quite narrow, we need to have a good frequency resolution near the peaks to get accurate results, and the recombination of

Fourier modes into a time-dependent signal is very sensitive to the small phase shifts that can occur in the algorithm. These numerical problem could be solved by the use of windowing functions, but we prefer use the domain-related code to analyze the results in one specific domain.

Now that we studied this first case deeply, we are going to study how we could possibly detect heavier or lighter primordial black holes.

4.2.2 Response in function of PBH mass

To study how the response in our cavity behaves in function of the primordial black hole mass, we consider the merger of binary black holes of two other masses. The first one is the merger of two $10^{-3}M_{\odot}$ primordial black holes and the second one is the merger of two $10^{-7}M_{\odot}$ primordial black holes. We can see the results in Figures 4.5 and 4.6. These simulations have the same detector parameters as the previous case except the binary merger masses. For the $10^{-3}M_{\odot}$ merger case (Figure 4.5), the frequency content of the signal is below the resonance frequencies. We see here that the electromagnetic wave produced by the inverse Gertsenshtein effect has the same frequency as the incoming gravitational wave. Let us recall the solution of the harmonic for the spectral coefficients of the induced magnetic field, in the frequency domain, equation (4.1.4),

$$\begin{aligned}\tilde{b}_{k10}(\omega) &= \tilde{b}_h(\omega) + \tilde{b}_p(\omega) \\ &= \frac{A_{k10} + iB_{k10}}{-\frac{\alpha_k c}{2Q} + i(\omega - \varpi_k)} + \frac{c^2\tilde{s}_{k10}(\omega)}{c^2\alpha_k^2 + \frac{i\omega\alpha_k c}{Q} - \omega^2}\end{aligned} \tag{4.1.4}$$

If $\omega \ll \alpha_k$ and $\frac{\omega L}{2c} \ll 1$, we wave that $\tilde{s}_{k10} \propto \omega^2\tilde{h}_+(\omega)$ by equation (3.4.26) and the particular solution $\tilde{b}_p(\omega)$ has a behavior proportional to $\omega^2\tilde{h}_+(\omega)$, and thanks to equation (3.3.31), the induced electromagnetic power is proportional to $\omega^3\tilde{h}_+(\omega)$. Because of equation (1.2.31) we have $\tilde{h}_+(\omega) \propto \omega^{-\frac{7}{6}}$, so the variation of the induced power in the cavity is proportional to $\omega^{\frac{11}{6}}$. We can see that the resonance frequencies are still triggered due to the homogeneous solution $\tilde{b}_h(\omega)$. But we can see that the amplitude in the time or the frequency domain is far below the previous case. If we look at the RMS induced power, we obtain a value around $10^{-14}W$ for the time domain code, $10^{-17}W$ for the frequency one, and $10^{-15}W$ for the integral estimation (4.1.6).

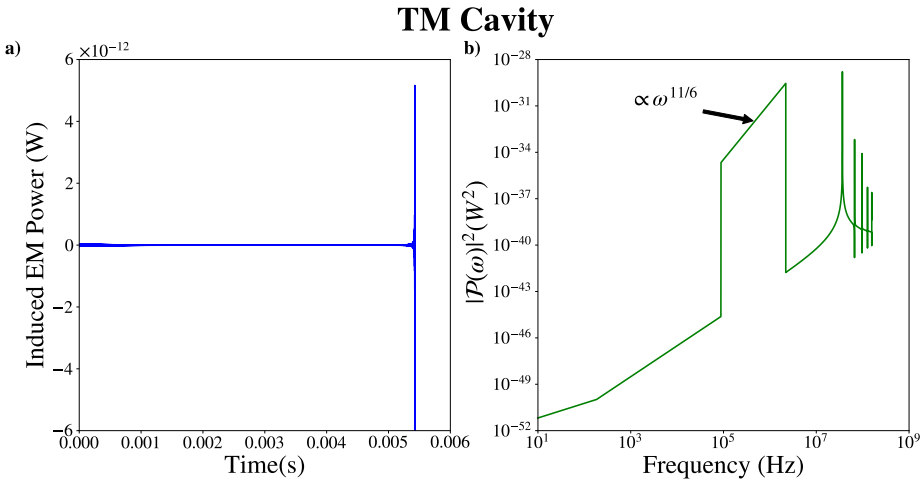

Figure 4.5 – Simulation of the cavity response to the gravitational wave signal of two $10^{-3}M_{\odot}$ non-spinning merging binary black holes. On panel a) we consider the TM cavity with the time domain code, on panel b) the TM cavity with the frequency domain code.

The time domain tends to overestimate the RMS power and we will study deeper this further in this manuscript. On the other hand, if we assume that our analytical estimation (4.1.6) is quite correct because it does not rely on numerical results, we can say that the frequency domain code tends to underestimate the RMS power for such a high mass.

The case of the $10^{-7}M_{\odot}$ merger can be discussed when looking at Figure 4.6. On panel a), we can see the time-dependent induced power has a different shape than in the case of the other masses. This is because the homogeneous solution is dominant. The homogeneous solution is actually overestimated because of the shape of the Fourier transform obtained by the FFT algorithm (recall the plateau of Figure 4.2). This feature will increase the particular solution at such low frequencies and will boost the values of the integration constants of the homogeneous solution $\tilde{b}_h(\omega)$. These numerical issues lead to inaccurate results for the behavior of the detector in the time domain when the frequency content is higher than the resonance frequency. In this case, computing in frequency domain is closer to physical reality . The resonance frequencies are excited due to the homogeneous solution but here the peaks are present with a bad frequency resolution, because our sampling is linear and in our figures the scale

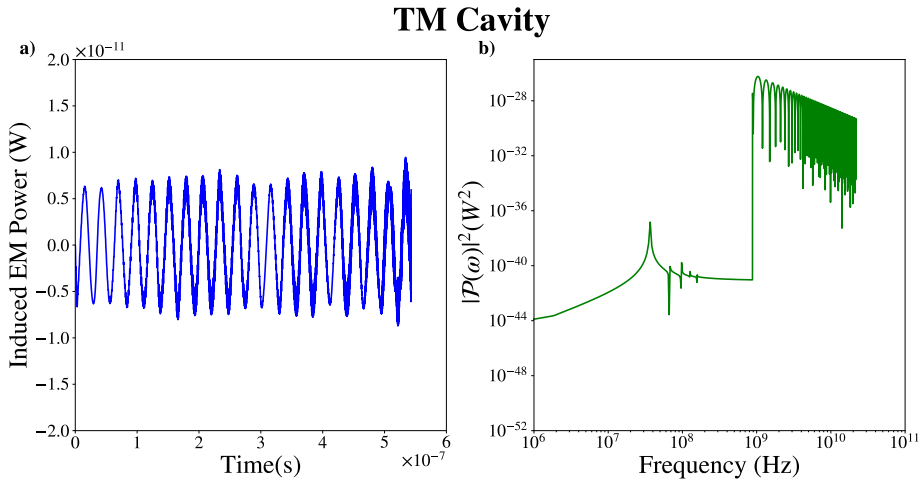

Figure 4.6 – Simulation of the cavity response to the gravitational wave signal of two $10^{-7}M_{\odot}$ non-spinning merging binary black holes. On panel a) we consider the TM cavity with the time domain code, on panel b) the TM cavity with the frequency domain code.

is logarithmic, so, we do not have enough points near the peaks when they are located at low frequencies. For the particular solution, we can easily find that if the frequency goes to infinity, we find that the induced power is proportional to $\tilde{h}_+(\omega)\sin\left(\frac{\omega L}{2c}\right)$. We can see the sine dependence because the particular solution is oscillating. The amplitude of these oscillations decrease because of $\tilde{h}_+(\omega) \propto \omega^{-\frac{7}{6}}$. In terms of the RMS values of the induced power, the time domain code gives us a value around $10^{-12}W$, the frequency domain code gives us $10^{-14}W$, and the RMS estimation integral gives us a value around $10^{-15}W$.

We will discuss the accuracy of all the methods by looking at the mass dependence of the RMS induced power, by studying the Figure 4.7. To plot this figure, we simulate the detection of the merger of binary primordial black holes of 50 different masses ranging from $10^{-3}M_{\odot}$ to $10^{-8}M_{\odot}$. For each mass, we simulate the detection of 50 different signals by their starting frequency chosen linearly between $\frac{f_{ISCO}}{30}$ to $\frac{f_{ISCO}}{10}$. We simulate this kind of detection process for the 5-meter TM cavity, the same detector that we consider above in this manuscript. The blue curve corresponds to the median of the RMS induced power obtained for each mass with the time domain code, the red curve is the same for the frequency domain code, and the green curve is the median of

the RMS induced power estimation integral. First, We can say about this figure is that the estimation of the RMS induced power is greater by using the time-domain code. For the lowest masses, we even reach a plateau for the RMS power. This phenomenon is due to a numerical artifact (plateau) coming from the FFT algorithm. This is why all the left part of the blue curve in Figure 4.7 is overestimated, the homogeneous solution of equation (4.1.2) is higher due to the FFT. For the highest masses, the time domain code is slightly higher than the two other codes. This is probably due to rounding errors and phase shifts in the addition of the homogeneous and particular solution. For the highest masses, the frequency domain code provide higher values than expected by analytical estimates. This could be because at such high frequencies, $\sin\left(\frac{\omega L}{2c}\right)$ oscillates very quickly and we cannot get an accurate RMS estimation. Let us now focus on the asymptotic behavior for the green curve, the RMS estimation integral. Recalling equations (4.1.7)

$$P_{\mathrm{RIR}}(\omega) = \frac{7\sqrt{2}c}{3\mu_0}\pi^2 B_0^2 \omega^2 \left|\sin\left(\frac{\omega L}{2c}\right)\right| \sum_k \frac{(I_k)^2}{\sqrt{\left(\alpha_k^2 c^2 - \omega^2\right)^2 + \left(\frac{\alpha_k \omega c}{2Q}\right)^2}}. \tag{4.1.7}$$

and (1.2.31),

$$\tilde{h}_+(\omega) = Ce^{i\psi_+(\omega)}\frac{c}{r}\left(\frac{GM_c}{c^3}\right)^{5/6}\left(\frac{\omega}{2\pi}\right)^{-7/6}\left(\frac{1+\cos^2\theta}{2}\right), \tag{1.2.31}$$

and the frequency dependence analysis we made, we can say that the behavior of the detector for mergers that have a frequency content below the resonance frequencies is proportional to $\omega^{\frac{11}{6}}$. Since the frequency is related to the inverse of the mass, we can conclude that the behavior for masses greater than $10^{-4}M_\odot$ is proportional to $M^{-\frac{11}{6}}$ (figure 4.7). In the same way, we can conclude that the behavior for masses lower than $10^{-6}M_\odot$ is proportional to $\omega^{-\frac{7}{6}}$ so the power is proportional to $M^{\frac{7}{6}}$. We can also check this in Figure 4.7.

We end this mass-dependence analysis of the induced power in the cavity by performing the same RMS power estimation (4.1.6) as the green curve in Figure 4.7 but for several outer radii of cavity. We can see the results in Figure 4.8, where we can see that for each radius, there is a resonant zone that is moved due to the displacement of the resonance frequencies that depends on the outer radius as we can see in Figure C.2

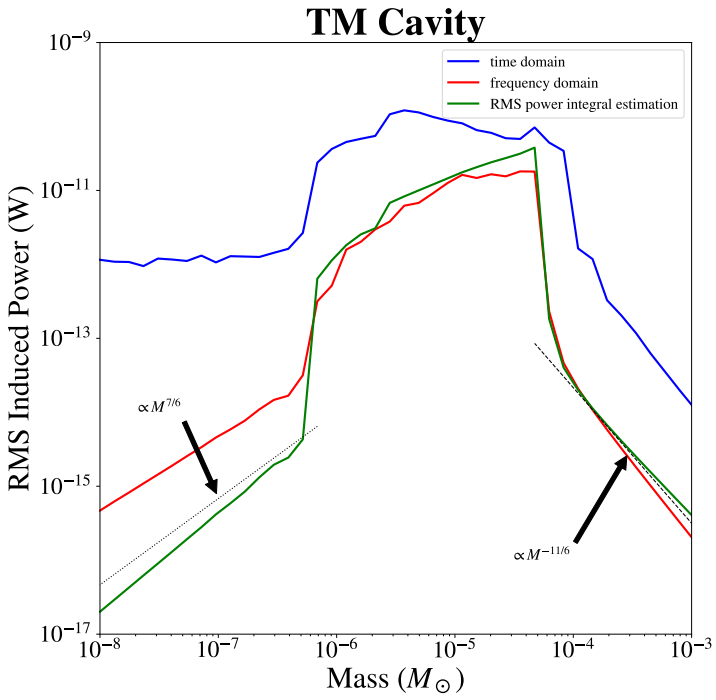

Figure 4.7 – Computation of the RMS induced power with respect of the mass of the merging black holes for the TM cavity.

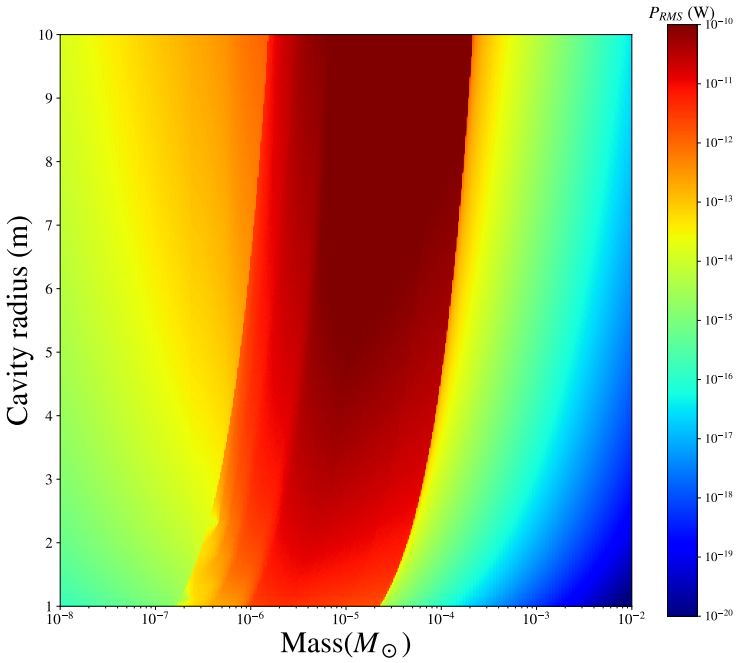

Figure 4.8 – Computation of the RMS induced power depending on the mass of the merging black holes and the outer radius for the TM cavity.

in Appendix C. We have to insist on the fact that choosing the parameters wisely for the cavity will allow optimizing the detection in the frequency window that we want, and in the case of primordial black hole detection, the mass of the primordial black holes we want to detect. Another feature that we can infer from this figure is that the response of the detector increases if the radius increases, even if the frequency is not in the resonant zone. This is because the induced power in our detectors is given by a volume integral (1). So if the radius of the cavity increases, the volume increases and the induced power increases. To conclude these results about primordial black hole merger detection, we show how we can set experimental limits on the PBH abundance in the dark matter and the Universe.

(1). In other words, we could possibly detect estimations of the variation of the energy stored in the cavity.

4.2.3 Detection limit on PBH abundance

As a final step, we combine the information we have on primordial black holes merging rates and the induced power as a function of the mass we found. The Figure 4.7 represents the induced power in the cavity for mergers at a fixed distance of 1 Gpc. This combination will forecast limits on the primordial black hole abundance for a fixed detector sensitivity of 10^{-14}W [(2)]. The duration of the signals are less than a second and we consider a survey of one year. To compute these expected limits, we calculated values the maximal radius where we can find at least an event a year for the two binary formation channels for primordial black holes, isolated binaries or binaries in clusters. Given that the gravitational strain amplitude is inversely proportional to the distance of the source, the induced power released in the detector is also inversely proportional to the distance. So for an electromagnetic power sensitivity $P_{\rm det}$, we have already (figure 4.7) computed the induced power in our detector depending on the primordial black hole mass and at a distance of 1 Gpc, what we call now $P_{RMS}(m_{PBH}, 1Gpc)$. We could detect at least one event a year if

$$\frac{P_{RMS}(m_{PBH}, D_1^{prim,clus})}{P_{\rm det}} \geq 1 \tag{4.2.1}$$

where $D_1^{prim,clus}$ is the maximal radius where we can find at least one event a year given by equations (1.2.51) and (1.2.53). Since these quantities $D_1^{prim,clus}$ depend on the fraction of dark matter made of primordial black holes $\tilde{f}_{PBH}$, we can express the limit on this parameter to get at least an event a year. For the isolated binaries we have

$$\tilde{f}_{PBH} \lesssim \left(4.2 \times 10^{-3} \frac{P_{\rm det}}{P_{RMS}(m_{PBH}, 1Gpc)} \left(\frac{m_{PBH}}{M_\odot} \right)^{0.29} \right)^{\frac{3}{2}} \tag{4.2.2}$$

and for the binaries in cluster we have

$$\tilde{f}_{PBH} \lesssim \left(58 \times 10^{-3} \frac{P_{\rm det}}{P_{RMS}(m_{PBH}, 1Gpc)} \right)^{\frac{3}{2}}. \tag{4.2.3}$$

Our final results are displayed in Fig. 4.9 that represents the expected limits on the effective parameter $\tilde{f}_{\rm PBH}$ corresponding to the dark matter density fraction in primor-

(2). This is a semi-educated guess, we think that it is achievable with current technology since for axion detection it is possible to go below this threshold ($10^{-22}W$ in [Asztalos et al., 2010]).

dial black holes at a given mass and per logarithmic mass interval in both formation models. These limits are computed for the proposed experimental designs described earlier, assuming a power sensitivity of 10^{-14}W for signals shorter than a second, achievable with current technology. The orange curve shows the possible abundance of planetary-mass PBHs inferred from recent microlensing observations towards the galactic bulge [Niikura et al., 2019]. These limits could be as low as $\tilde{f}_{\rm PBH} \lesssim 10^{-8}$ for primordial binaries, and $\tilde{f}_{\rm PBH} \lesssim 10^{-4}$ for tidal capture in clusters. The range (between 10^{-6} and 10^{-4} $M_\odot$) where the resonance plays a role is clearly visible and this boosts the limits by about four orders of magnitude. This could therefore set unprecedent and independent limits on the abundance of planetary-mass primordial black holes.

Now in this manuscript we look at an another application of resonant cavities gravitation wave detection, the detection of the stochastic gravitational wave background.

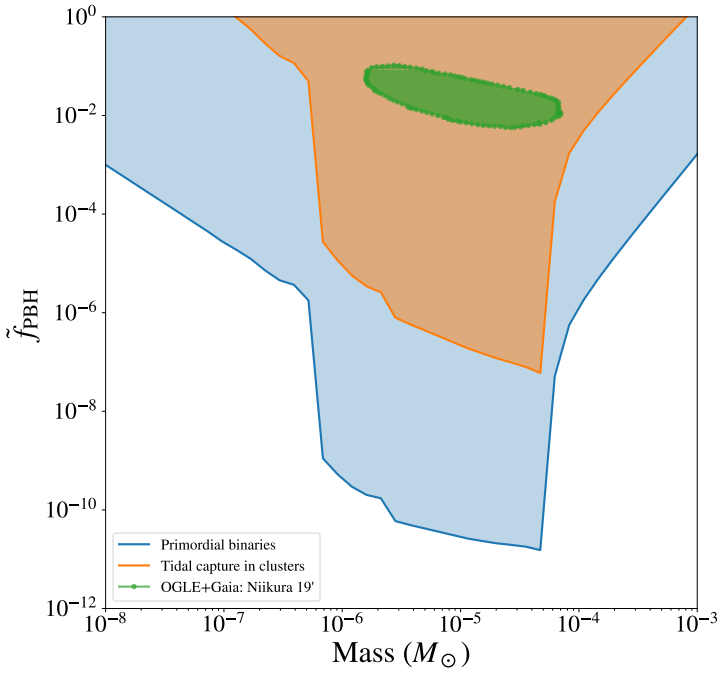

Figure 4.9 – Expected limits on the effective parameter $\tilde{f}_{\rm PBH}$ for an event a year detection

4.3 Stochastic Gravitational wave background

The second application we simulate is the stochastic gravitational wave background detection. This source, as its name indicates, is a stochastic source. It is not a transient one like the primordial black hole merger we studied above. This feature leads us to slightly adapt the way we study the detection process, using a toy model for the stochastic gravitational wave background and see how we can detect its cut-off frequency or its frequency dependence.

4.3.1 From transient to stochastic signals

In the code we previously built, we took a time-dependent or frequency-dependent signal, unlike a stochastic one. We show how to deal with it. We saw in the first chapter how we can model the stochastic gravitational wave background. If we correlate the plus polarization of the gravitational wave, looking at the same solid angle and the same frequency we have equation (1.2.55)

$$|\tilde{h}_+(\omega)|^2 = \frac{S_h\left(\frac{\omega}{2\pi}\right)}{2}, \tag{4.3.1}$$

where $S_h(\omega)$ is a one-sided power spectral density. That means that we have an information about the frequency dependent signal. The Wiener-Khintchine theorem [Wiener, 1930, Khintchine, 1934] says that the module squared $|\tilde{h}_+(\omega)|^2$ is the Fourier transform of the autocorrelation function of $h_+(t)$ that we denote $\gamma(h_+(t))$ and can be defined as

$$\gamma(h_+(t)) = \lim_{T\to\infty} \frac{1}{2T} \int_{-T}^{T} h_+^*(\tau) h_+(\tau + t) d\tau. \tag{4.3.2}$$

This is the convolution between a signal and his time-shifted version. The Wiener-Khintchine theorem can be written as $\tilde{\gamma} = |\tilde{h}_+(\omega)|^2$. In stochastic process analysis, this function is used to detect when shifted signals are the same, so having its Fourier transform is extremely useful for the study of the stochastic gravitational wave background. In the case of our code, we can for instance use our frequency code with a purely real frequency dependent signal

$$\tilde{h}_+(\omega) = \sqrt{\frac{S_h\left(\frac{\omega}{2\pi}\right)}{2}}, \tag{4.3.3}$$

as the source for our frequency domain code. We can thus compute $\tilde{\mathscr{P}}(\omega)$ where we can infer the power spectral density of the induced power, which is $|\tilde{\mathscr{P}}(\omega)|^2$. Since only the modulus squared quantities are relevant for such an analysis, the simplification (4.3.3) is valid because it does not affect the modulus of the induced power. The only thing we do is a phase shift in the complex plane to make $\tilde{h}_+(\omega)$ real. To determine the one-sided spectral density $S_h(\nu)$, where $\nu = \frac{\omega}{2\pi}$, we can recall equations (1.2.58) and (1.2.59) to get

$$S_h(\nu) = \frac{3H_0^2}{4\pi^2}\Omega_{\mathrm{GW}}(\nu)\nu^{-3} sigm(-\nu + \nu_{\mathrm{cut}}). \tag{4.3.4}$$

where $sigm(\nu) = \frac{1}{1+e^{-\zeta\nu}}$ is the sigmoid function, where we choose the scale parameter $\zeta = \frac{20}{\nu_{\mathrm{cut}}}$ to have the sharpness of decrease in logarithmic scale whatever the cut-off frequency ν_{cut} is.

With equation (4.3.4), we can model our stochastic background by two parameters, the first is the energy density per logarithmic frequency sampling $\Omega_{\mathrm{GW}}(\nu)$, and the second is the cut-off frequency ν_{cut}, where the stochastic background vanishes above this threshold. Please note that our two-parameters model (4.3.4) consider a correlation at any solid angle, this model should be multiplied by a cross-section related to the detection direction, that we can assume of unit order and neglect at this stage of analysis.

4.3.2 Study of a toy model for SGWB

Since we can model our stochastic background with only two parameters, we are going to make a simple toy model to study a stochastic background detection process. We assume that $\Omega_{\mathrm{GW}} = 10^{-10}$. The constancy and the value of this parameter is coherent with the tables given in [Aggarwal et al., 2021] with the model of stochastic gravitational wave background in [Maggiore, 2018] for the single-field slow-roll inflation. From [Aggarwal et al., 2021] we get also the value for the cut-off frequency, 100 MHz. Here we consider a cut-off with a sigmoid function so the stochastic background vanishes exponentially as mentioned in the inflation stochastic background models in [Maggiore, 2018]. You can see an example of the toy model in the Figure 4.10.

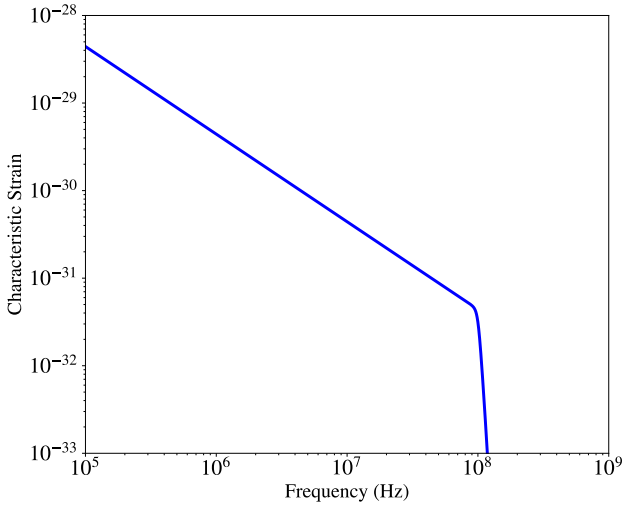

Figure 4.10 – The characteristic strain for our stochastic GW background toy model.

The plot of the power spectral density of the induced power in the cavity through the detection of this toy model can be found for three different cut-off frequencies ν_{cut} (10 MHz, 100 MHz and 1GHz) in Fig. 4.11. The simulation was made with our frequency domain code for the TEM cavity, for 5m outer radius and 1m-long cavity, the inner radius is 10cm and the external field is 5T. We can see that for our cavity the resonance frequencies before the cut-off will have much higher density than the other ones. Indeed, for $\nu_{cut} = 10$ MHz, all the resonant peaks have low density, for $\nu_{cut} = 100$ MHz, only the three first resonant peaks have high density and for the latter $\nu_{\text{cut}} = 1$ GHz, all the resonant peaks have a high density. This means that the auto-correlation of several signals coming from the stochastic background will be higher at the first resonance frequency and if we detect a significant drop between two resonance frequencies, the cut-off frequency must be somewhere in between.

We want to insist on the fact that it is possible to tune the detectors parameters to get the resonance frequencies we want, for optimal detection. This is also shown in Fig. 4.12. Here we simulate the RMS induced power for several outer radius between 1m and 10m. We also considered other distribution for Ω_{GW}, as one can see through the green and blue points. There is a gap in the values around 1.5m. This gap is where the fundamental ($k = 0$) resonance frequency goes below the stochastic background cut-off frequency and the response is several orders of magnitude higher. We can

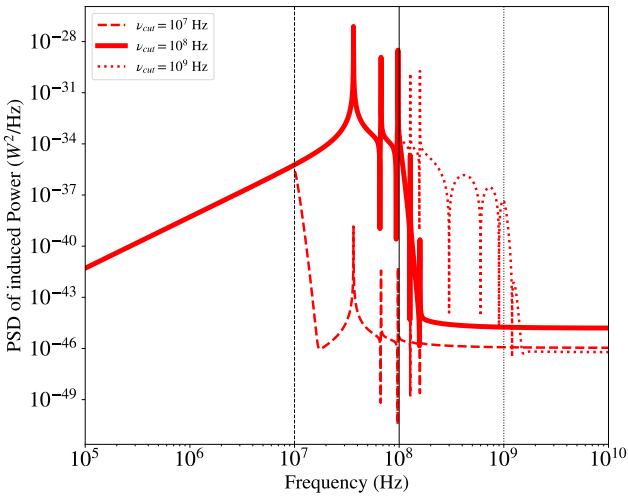

Figure 4.11 – The power spectral density of the induced EM Power expected with our stochastic GW background toy model, for three different cut-off frequencies.

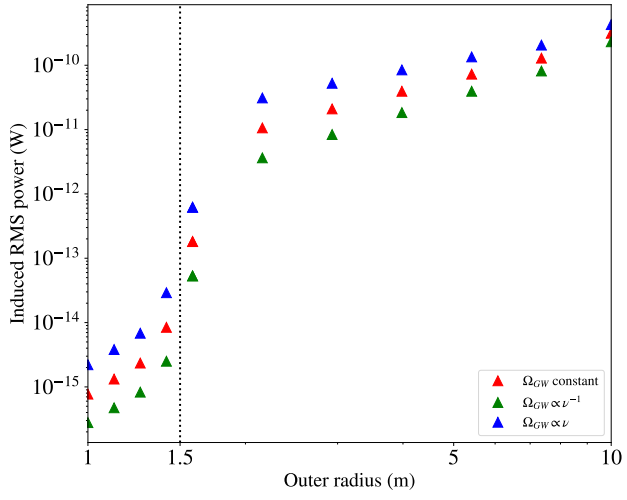

Figure 4.12 – RMS induced EM power generated in our cavity with respect to the radius of the detector for our stochastic GW background toy model.

see that the cavities resonance frequencies are close to the cut-off frequency $\nu_{\text{cut}} =$ 100 MHZ when the radius is 1.5m in Figure C.2 in Appendix C. If one can combine detectors of different radii, we can also spot more precisely the cut-off frequency and also check whether or not Ω_{GW} is constant with frequency as could be supposed for instance in [Maggiore, 2018]. The value of the slope after the gap, could not be straightforwardly computed as the radius of the cavity appears on many quantities in the response computation. This slope is around 2 for constant Ω_{GW}, meaning that the main contribution of the increasing induced power with the radius comes from the increase of the detection volume, which is proportional to the square of the radius for a cylinder. Another assumption for Ω_{GW} will lead to another slope in this model, since the frequency content in the integral (4.1.6) will be different. For instance, for the Ω_{GW} varying linearly with the frequency, the slope will be around 1.5.

To sum up the results presented above, resonant detectors allow to probe the cut-off frequency of the yet hypothetical stochastic gravitational wave background and also check the constancy of the gravitational wave density with frequency, two parameters that are specific to some early Universe stochastic gravitational wave background models.

4.4 Sensitivity curves and conclusion

As final step for this chapter, we present the sensitivity curves for the resonant electromagnetic detection, in Figure 4.13

The black dashed curve represents the strain we could possibly detect if we can detect 10^{-14} W of RMS induced power, with respect to the frequency. (3) The detector parameters are the same as the previous simulations, 5T external field, 5m radius and 1m-long cavity. This is the parameters we advice because the radius is suited to maximize the detection of $10^{-5} M_{\odot}$ primordial black hole binaries and also suited to spot a stochastic background cut-off frequency around 100 MHz. This curve is derived from the RMS impulse response given in equation (4.1.7). To obtain this information, we have to use the first results in this chapter, the computation of the resonance frequencies summarized in the Figure C.2 in Appendix C, and the computation of all the cavity-related quantities (modes, volume integrals, resonance frequencies).

(3). This sensitivity is directly proportional to the detection threshold. Choosing another threshold will only shift the black dashed curve on the y-axis.

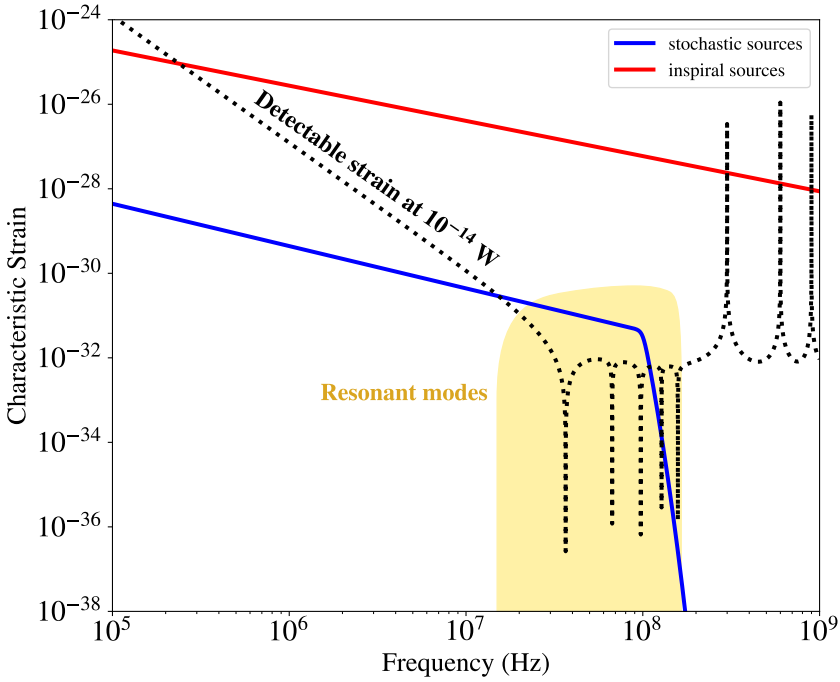

Figure 4.13 – Strain sensitivity of our cavity and possible sources. If the straight lines are above the dotted one, that means that our detector is sensitive to these sources for the frequencies considered.

To go back to the dashed black curve, we can see that the sensitivity is the best at the resonance frequencies highlighted by the yellow zone. At lower frequency, the sensitivity will go as ν^{-3}, and at higher frequency, the sensitivity will be bounded, but will oscillate as $\sin\left(\frac{\omega L}{2c}\right)$. Please note that here we can speak about sensitivity curve but in this manuscript we do not take account of the noise sources. One of the future work for this research is to investigate the noise sources to obtain a signal-to-noise ratio that we can put in the sensitivity curves, that will be more realistic.

The second curve, the red one, represents the characteristic strain for an inspiral binary gravitational wave signal. This curve is consistent with several stochastic background presented in [Aggarwal et al., 2021]. If we could detect $10^{-14}W$ of RMS induced power, we could detect a wide range of frequency for these sources, since the inspiral source curve is above the dashed line in a wide frequency range. The best sensitivity is still at the resonance frequencies.

The third and final curve, the blue one, is the characteristic strain for stochastic sources. This curve is also consistent with [Aggarwal et al., 2021]. We could probably have a good sensitivity around 100 MHz. We showed first how to adapt our code to consider these stochastic sources.

In this chapter we simulated the detection of mergers of equal-mass primordial black holes binaries. We first studied the merger of two 10^{-5} primordial black holes, because this is the most likely planetary-mass primordial hole regarding microlensing observations. We showed how our codes in the time and the frequency domain works, and how estimate the expected RMS induced power. We also used this first merger signal to compare the codes. Then, we simulated the detection of heavier or lighter black holes to see what can influence the response of our detector. We finally showed how the induced power in the cavity varies with the mass of the black holes and the radius in the cavity. We also put some experimental limits to the effective parameter that represents the part of primordial black holes that explain the dark matter. We showed that even for a quite small fraction of dark matter made of primordial black holes (less than 1%), we could possibly detect at least one event a year. Then, we studied how we could detect stochastic gravitational wave background and characterize its cut-off frequency and its energy density per logarithmic frequency sampling Ω_{GW}. In this purpose and also for primordial binaries, the use of several detectors of different radii could be useful to have a better sensitivity on a wider range of frequency and to understand deeper the frequency dependence of the wave generated by those sources.

4.5 Our detector proposal in the literature

This detector proposal is one of the inverse Gertsenshtein electromagnetic devices proposed for high-frequency gravitational wave detection. Our detector has the advantage to provide a response at first order of gravitational perturbation, as the oscillating external field one proposed in [Zheng et al., 2018]. This feature is a great advantage because we could get a much better strain sensitivity (many order of magnitude), if we compare to the detectors on second order (e.g [Berlin et al., 2022]), the detector proposed in [Ejlli et al., 2019] is a bit different since it aims to detect a frequency band above THz.

Another feature of our detector proposal is that we simulate the detection of astrophysical gravitational wave signals. In our review of the proposals, they provide hints of detection but no detection simulation. Our analysis was also made in both temporal and frequency domain, to minimize numerical artifacts. Some other works do not have this problem since they consider only monochromatic signals.

Our temporal approach provides accurate temporal response for incoming signals of frequencies equal or lower to the resonant frequencies of our cavity. This approach is commonly used in the literature. The frequency approach was not used in the different papers we mentioned in section 2.3 of this manuscript. Frequency approach helped us to analyze stochastic signals without generating a huge number of random incoming signals. We conclude that the temporal approach is more sensitive to numerical artifacts. However, the accuracy of both approach is limited due to the fact that we work on discretized signals in both domains. The last computations we made are estimations of the RMS induced power in a cavity with a volume integral. This estimation is first an analytical estimation computed then with the Romberg algorithm, a accurate numerical computation of integrals. This estimation is less contaminated by numerical errors, but is still an estimation. However, the behavior outside the resonance zone is close to what we expected analytically. Practically, trying to detect outside the resonance zone is inefficient, and the three approaches provide similar results inside the resonance zone as we can see in figure 4.7.

One of the main feature of our work is that we want to measure the RMS induced power in the cavity at first order. This is a macroscopic quantity over a volume, related to the energy variation inside the cavity. Even if, as mentioned in [Berlin et al., 2022],

this term vanishes if we take simple time average. The situation studied in our work and in [Berlin et al., 2022] is quite similar, despite the fact that we consider a coaxial cavity. In the approach, we decided to consider directly the quantity we thought interesting to study, the RMS induced power in the cavity. Quantity that vanish in [Berlin et al., 2022] because it vanishes in a simple time average. In [Berlin et al., 2022], they studied how the cavity modes are triggered to compute the energy stored in the cavity, where they discard the first order contribution. Nevertheless, we think that this quantity deserved to be considered to boost the sensitivity of electromagnetic detection.

One of the limitations of our work is that we might develop more the proposal to make a concrete experiment. We do not take into account the noise sources to get sensitivity curves with the signal-to-noise ratio, and we do not consider clearly how the induced power in the cavity will be detected. This is why we need collaboration with experimental physicist to make a step forward. A starting point is the work [Zheng and Wei, 2022] which gives the first prospects about the noise sources for inverse Gertsenshtein detection with an external oscillating field.

The fact that we assume that the direction of propagation is aligned with the symmetry axis of the cavity is also a limitation. The results of our paper [Herman et al., 2021] was made in the TT frame, before considering the detector frame, and in [Berlin et al., 2022] they provide directional sensitivity plots thanks to the modeling in the proper detector frame. The question of the directional sensitivity is clearly an aim for further research.

After discussing the accuracy of our results, and their limitations, we can notice that our work triggered some interests in the scientific community, the first paper [Herman et al., 2021] was cited by some papers of the primordial black hole research community [Bastero-Gil and Subías Díaz-Blanco, 2021, Pujolas et al., 2021, Carr et al., 2021, Miller et al., 2022, Franciolini et al., 2022], the high-frequency gravitational wave community [Goryachev et al., 2021, Tobar et al., 2022], the search for stochastic background [Saito et al., 2021] and the other detector proposals [Berlin et al., 2022, Domcke et al., 2022, Zheng and Wei, 2022]. The second paper [Herman et al., 2022] is still in publication process. However, the preprint was already mentioned in three different published papers [Ringwald and Tamarit, 2022, Franciolini et al., 2022, Dasgupta et al., 2022].

We want to end this chapter by saying that we think there are "good" ideas among the different proposals about inverse Gertsenshtein effect detection, that combined together could lead to another breakthrough in gravitational wave astronomy, the electromagnetic detection of gravitational waves.

Conclusion and perspectives

In this manuscript, we study the resonant electromagnetic detection of high-frequency gravitational waves, from a theoretical point of view. The search for high-frequency gravitational waves can for instance get us information about the early stages of the Universe, and this is what we focus on.

We first introduced the gravitational wave theory, with a short introduction about the general relativity theory, and then considered a perturbative theory in it, that leads to the gravitational wave equation. These are perturbations of spacetime itself that propagates in the Universe. We saw what are the polarization of such waves in the vacuum, before considering how they could be generated. After making an overview about the current situation on gravitational wave detection, we presented some sources of high-frequency gravitational waves. Those can not be detected by interferometers, so we had to imagine another type of detection. Among these sources, there are two witnesses of the early Universe that we focused on. The first are sub-solar mass primordial black holes. Those tiny black holes formed in the beginning of the Universe are what we call a dark matter candidate, meaning it can explain at least a part of the matter we could not detect non-gravitationally in the Universe. The second one is the stochastic gravitational wave background, which could be the first emission of gravitational waves in the Universe, an analog to the cosmic microwave background with gravitational waves. This background could contain information about the early Universe physics, and describe events that happen before the photon decoupling epoch, when the cosmic microwave background was emitted. These two high-frequency gravitational wave sources are still hypothetical, so this is another motivation to try to detect them. The possible detection of the stochastic gravitational wave background would a revolutionary breakthrough in physics and a giant leap for the understanding of the

beginning of the Universe. After all these considerations, we discussed the choice of the frame for detection modeling.

Once this gravitational wave theory described, we had to focus on the link between electromagnetism and gravitational waves. We first constructed the Einstein-Maxwell system, covariant electromagnetism theory in the framework of general relativity. Then we described the Gertsenshtein effects. The direct one is generation of gravitational waves with electromagnetic fields, the inverse one is the generation of faint electromagnetic waves due to the passing of a gravitational wave in a magnetic region. After describing their theories, we reviewed all the inverse Gertsenshtein effects gravitational wave detector proposal since the formulation of the effect by Gertsenshtein [Gertsenshtein, 1960].

Then, we began to describe our results. First, we modeled two detectors that are patented [Füzfa, 2018] cylindrical cavities, immersed in a strong external magnetic field. We obtained the wave equations for the induced electromagnetic field produced by the inverse Gertsenshtein effect. The following was some analytical work on computing the cavity response, projecting our wave equation on the eigenfunctions of the Laplacian operator, and computing the source term of our wave equations, which contains the incoming gravitational wave. At the end, we got quite simple expressions to compute the induced electromagnetic power in the cavity, at first order of perturbation. We can compute that in time or frequency domains, and a practical approximation of the root-mean-square induced power.

The final chapter used the analytical expressions mentioned above in numerical simulations about primordial black hole merger detection and the search for stochastic gravitational wave background.. We showed what would be the response of our cavity to primordial black holes where their masses match the microlensing observation bounds [Niikura et al., 2019], and saw what happens with heavier or lighter black holes, and if we tune the radius of the detector. We also dealed with poor approximations in several cases due to numerical artifacts. We ended up by putting experimental limits on the fraction of dark matter explained by primordial black holes that we could possibly detect. Our code was made for transient signals so, we had to adapt our analysis to stochastic signals in the frequency domain. We considered a toy model for the stochastic gravitational wave background that contains two parameters, the gravitational wave energy density per logarithmic frequency sampling and the cut-off

frequency, a toy model close to the ones presented in [Maggiore, 2018]. We showed how to detect the cut-off frequency and get the distribution of the energy density by tuning the radius of cavity. We ended this manuscript by talking about sensitivity curves and placing our detector proposal in the literature.

There are several perspectives about this work. The first that comes in mind is to make this research one step forward to experimental realization. In order to do this, we need to collaborate with experimental physicists from gravitational waves detection, axion detection, electromagnetic cavities and intense magnetic fields communities. The main goal is to make a sketch of a feasible table-top experiment, with taking into account the noise sources, perform sensitivity curves as already made for interferometry techniques. This experimental step is crucial to make the transition between the theoretical level considered here and the experimental one.

Another immediate perspective of this work is to perform a cross-validation of the analytical results with a naive approach. This approach is to compute the induced magnetic field in our cavity by resolving the full wave equation numerically, for instance with finite differences methods. This method allows us to implement the full effective current density and check if our predictions for the induced electromagnetic power in the cavity are correct. The challenging aspect of doing this is to avoid numerical artifacts and control the numerical error. This kind of methods could also open the door to perform second order energy corrections, and correlate them with the work made in [Berlin et al., 2022] for monochromatic incoming signals. This approach could make easier the study of directional sensitivities or computing other quantities as detector response.

The study of generation of gravitational waves by these cavities could also be interesting, by using the direct Gertsenshtein effect. The benefit of this work is twofold. First, manipulating the direct effect could help us to better understand the Gertsenshtein effects. Second, it could help us to elaborate a gravitational Hertz experiment [Kolosnitsyn and Rudenko, 2015], an experience of generation and detection of gravitational waves. This experiment would be groundbreaking in gravitational wave science, meaning that we could manipulate those waves as the electromagnetic ones.

In our proposal, we chose a defined geometry for our detector. It could be interesting to study other cavity geometries, like rectangular or toroidal ones. The latter came

recently into the spotlight [Domcke et al., 2022]. It would be interesting to check if the geometry has a big influence on the response of the detector. We already know that the volume has an amplification role. It would be useful to check other parameters.

The final perspective that comes in mind is to model different sources suitable for electromagnetic detection, and develop data analysis techniques to identify potential detected signals, as already made for interferometers. We could also consider better models for the stochastic gravitational wave background to be more realistic and find key indicators to rule out some models with experimental observations.

I will end this manuscript by claiming that electromagnetic high-frequency gravitational wave detection theory is still at the beginning, but seems to me very promising. I strongly encourage experimental physicists to get into this part of gravitational wave physics, that could lead to table-top-size experiments and could be very complementary to interferometers and pulsar timing arrays. This could be the way to better understand the early moments of our Universe, or make a step forward to the unification of the fundamental interactions.

Appendices

Appendix A

The harmonic oscillator equation

In this appendix, we will consider general resolution of an forced and damped harmonic oscillator equation, in the time and the frequency domain, to clearly define our way to solve equations (3.3.14) and (3.3.17).

$$\frac{d^2x}{dt^2} + 2\gamma\frac{dx}{dt} + \Omega^2 x = s(t) \tag{A.0.1}$$

and his Fourier transform equation

$$-\omega^2\tilde{x} + 2i\omega\gamma\tilde{x} + \Omega^2\tilde{x} = \tilde{s}(\omega). \tag{A.0.2}$$

Such linear equations admit solutions of the type

$$x = x_h + x_p \tag{A.0.3}$$

where x_h is the homogeneous solution (where $s(t) = \tilde{s}(\omega) = 0$) and x_p the inhomogeneous one. The equation (A.0.1) provides us easily the homogeneous solution in function of time

$$x_h(t) = e^{-\gamma t}\left(A\cos(\varpi t) + B\sin(\varpi t)\right) \tag{A.0.4}$$

where $\varpi = \sqrt{\Omega^2 - \gamma^2}$ and the integration constants A and B are to be determined with the initial conditions. On the other hand, the inhomegenous solution in the frequency domain can be easily computed with the algebraic equation (A.0.2),

$$\tilde{x}_p(\omega) = \frac{\tilde{s}(\omega)}{\Omega^2 + 2i\omega\gamma - \omega^2}. \tag{A.0.5}$$

We can thus obtain the solution of our harmonic oscillator equation in both domains by applying the Fourier transform of the homogeneous solution $x_h(t)$ and the inverse Fourier transform of $\tilde{x}_p$. The solution in the time domain is

$$x(t) = e^{-\gamma t}\left(A\cos(\varpi t) + B\sin(\varpi t)\right) + \frac{1}{2\pi}\int_{-\infty}^{\infty} \frac{\tilde{s}(\omega)}{\Omega^2 + 2i\omega\gamma - \omega^2} e^{i\omega t} d\omega \tag{A.0.6}$$

and the solution in the frequency domain is

$$\tilde{x}(\omega) = \frac{A + iB}{-\gamma + i(\omega - \varpi)} + \frac{\tilde{s}(\omega)}{\Omega^2 + 2i\omega\gamma - \omega^2} \tag{A.0.7}$$

With these equations (A.0.6) and (A.0.7), we are able to solve our harmonic oscillator equations, (3.3.14) and (3.3.17).

Appendix B

Synthesis: Compute the response of our detector

This section will show you how to compute the induced electromagnetic power at leading order, for the detection of a plus-polarized wave, $h_+(t)$ in the time domain or $\tilde{h}_+(\omega)$ in the frequency domain. Those responses are functions, and we will show here how we can estimate the root-mean-square power of such induced power signals, related to the $\mathscr{L}^2$ norm. Please note that we only consider the plus polarization because there aren't any cross polarized gravitational wave terms in the source terms (3.4.21), because the cavity is aligned with the propagation direction of the gravitational wave.

B.1 Time domain

In the time domain, we can study the detection of time dependent signal, with their plus polarization in the TT gauge, $h_+(t)$. We can compute the useful source term of our harmonic oscillator equation with equation (3.4.6) multiplied by $\frac{7}{6}$ due to equation (3.4.20)

$$\hat{s}_{k10}(t) = -\frac{7\pi B_0 I_k}{6c}\left(\frac{\partial h_+}{\partial t}(t+\frac{L}{2c}) - \frac{\partial h_+}{\partial t}(t-\frac{L}{2c})\right). \tag{4.1.1}$$

With that we can solve the equation (3.3.14) for the $(k,1,0)$ modes, and can be written as

$$\frac{1}{c^2}\frac{d^2\hat{b}_{k10}}{dt^2}+\frac{\alpha_k}{cQ}\frac{d\hat{b}_{k10}}{dt}+\alpha_k^2\hat{b}_{k10}=\hat{s}_{k10}(t) \tag{B.1.1}$$

with $\Omega_{k10}=\alpha_k$ due to equation (3.3.10), the α_k coefficients are the resonant wavenumbers of the cavity. Please note that, by dimensional analysis, the coefficients $\hat{b}_{k10}$ are in T (tesla) and $\hat{s}_{k10}(t)$ in $\frac{T}{m^2}$. We can easily solve these harmonic oscillator equations with equation (A.0.6) in the Appendix A, in order to obtain

$$\hat{b}_{k10}(t)=e^{-\frac{\alpha_k c}{2Q}t}\left(A_{k10}\cos\left(\varpi_k t\right)+B_{k10}\sin\left(\varpi_k t\right)\right)+\frac{1}{2\pi}\int_{-\infty}^{\infty}\frac{c^2\tilde{s}_{k10}(\omega)}{\alpha_k^2c^2+\frac{i\omega\alpha_k c}{Q}-\omega^2}e^{i\omega t}d\omega \tag{4.1.2}$$

where $\tilde{s}_{k10}(\omega)$ is the temporal Fourier transform of $\hat{s}_{k10}(t)$ and $\varpi_k=c\alpha_k\sqrt{1-\frac{1}{2Q}}$. The constants A_{k10} and B_{k10} are determined with initial conditions $\hat{b}_{k10}(t=0)=\left.\frac{d\hat{b}_{k10}}{dt}\right|_{t=0}=0$, because there is no induced field before the passing of the gravitational wave. With these solutions we can finally compute the first order induced electromagnetic power, computed in the proper detector frame, with equation (3.3.30)

$$\mathscr{P}(t)=\frac{2\pi B_0}{\mu_0}\sum_k I_k\frac{d\hat{b}_{k10}}{dt}(t). \tag{3.3.30}$$

B.2 Frequency Domain

In the frequency domain, we can study the detection of frequency dependent signal, with their plus polarization in the TT gauge, $\tilde{h}_+(\omega)$. We can compute the useful source term of our harmonic oscillator equation with equation (3.4.26)

$$\tilde{s}_{k10}(\omega)=\frac{7\pi B_0 I_k\omega\tilde{h}_+(\omega)}{3c}\sin\left(\frac{\omega L}{2c}\right). \tag{3.4.26}$$

With that we can solve the equation (3.3.17) for the $(k,1,0)$ modes

$$-\frac{\omega^2}{c^2}\tilde{b}_{k10}+\frac{i\omega\alpha_k}{cQ}\tilde{b}_{k10}+\alpha_k^2\tilde{b}_{k10}=\tilde{s}_{k10}(\omega) \tag{B.2.1}$$

with $\Omega_{k10}=\alpha_k$ due to equation (3.3.10). We can easily solve these harmonic oscillator

equations with equation (A.0.7) in the Appendix A, in order to obtain

$$\tilde{b}_{k10}(\omega) = \frac{A_{k10} + iB_{k10}}{-\frac{\alpha_k c}{2Q} + i(\omega - \varpi_k)} + \frac{c^2 \tilde{s}_{k10}(\omega)}{c^2\alpha_k^2 + \frac{i\omega\alpha_k c}{Q} - \omega^2} \tag{4.1.4}$$

with $\varpi_k = c\alpha_k\sqrt{1-\frac{1}{2Q}}$. The constants A_{k10} and B_{k10} are determined with initial condition $\hat{b}_{k10}(t=0) = \frac{d\hat{b}_{k10}}{dt}\Big|_{t=0} = 0$. With these solutions we can finally compute the first order induced electromagnetic power, computed in the proper detector frame, with equation (3.3.31)

$$\tilde{\mathscr{P}}(\omega) = \frac{2i\pi\omega B_0}{\mu_0}\sum_k I_k \tilde{b}_{k10}(\omega). \tag{3.3.31}$$

B.3 RMS power calculation

In this section, we summarized how we can compute the induced electromagnetic field at first order, in the proper detector frame, in a gravitational wave detection process. This is the response we chose to compute for our detectors. This response can be function of time of frequency, but the duration of the signal or its frequency content could be quite different with respect of the incoming gravitational wave. This is why we have to compute a quantity that can be useful to compare signals between each other. For such oscillating field, we have to consider the root-mean-square average, that can be defined as

$$\mathscr{P}^2_{\mathrm{RMS}} = \lim_{T\to\infty}\frac{1}{T}\int_0^T (\mathscr{P}(t))^2\, dt. \tag{B.3.1}$$

This is a key quantity because it is related to the $\mathscr{L}^2$ norm of the signal, which is conserved through the Fourier transform since this last is unitary. Physically, as it can be done for AC electric currents, the RMS power is related to the energy of the signal. One quantity that we can compute using this definition of RMS power is the RMS power impulse response. This the RMS power when the incoming signal is a sine wave. If we consider $h_+(t) = \sin(\omega t)$, we have with equation (4.1.1) that

$$\hat{s}_{k10}(t) = \frac{7\pi B_0 I_k \omega}{3c}\sin\left(\frac{\omega L}{2c}\right)\sin(\omega t). \tag{B.3.2}$$

This equation (B.3.2) is coherent with equation (3.4.26). With such a source term the solution of equation is simpler,

$$\begin{aligned}\hat{b}_{k10}(t) =& e^{-\frac{\alpha_k c}{2Q}t}\left(A_{k10}\cos(\varpi_k t)+B_{k10}\sin(\varpi_k t)\right)\\ &+\frac{7\pi c B_0 I_k \omega}{3}\sin\left(\frac{\omega L}{2c}\right)\frac{\sin(\omega t+\phi)}{\alpha_k^2 c^2+\frac{i\omega\alpha_k c}{Q}-\omega^2}.\end{aligned} \tag{B.3.3}$$

If we look at the behavior of this solution when t goes to infinity, one can discard the homogeneous solution because of the decreasing exponential $e^{-\frac{\alpha_k c}{2Q}t}$. In this case, we can compute the P_{RIR}, the RMS impulse response electromagnetic power,

$$P_{\mathrm{RIR}}(\omega)=\frac{7\sqrt{2}c}{3\mu_0}\pi^2 B_0^2\omega^2\left|\sin\left(\frac{\omega L}{2c}\right)\right|\sum_k\frac{(I_k)^2}{\sqrt{\left(\alpha_k^2c^2-\omega^2\right)^2+\left(\frac{\alpha_k\omega c}{2Q}\right)^2}}. \tag{4.1.7}$$

This equation can be useful because if we neglect the contribution of the homogeneous solution that vanish when t goes to infinity, equations (3.3.31) and (4.1.2) can show us that

$$|P(\omega)|^2=2|P_{\mathrm{RIR}}(\omega)|^2|\tilde{h}_+(\omega)|^2, \tag{B.3.4}$$

where we have here the GW power spectral density $|\tilde{h}_+(\omega)|^2$. This expression will help us to close this chapter by finding a practical estimation of RMS induced power when we have a signal $\tilde{h}_+(\omega)$. Let us first assume that $\mathscr{P}(t)$ is a periodic function, one can expand it as a real-valued Fourier series, (1)

$$\mathscr{P}(t)=\sum_{n=1}^{\infty}\left(a_n\cos\left(\tfrac{2\pi}{U}nt\right)+b_n\sin\left(\tfrac{2\pi}{U}nt\right)\right) \tag{B.3.5}$$

where U is the period. Putting the expression above in the definition (B.3.1) gives us

$$\mathscr{P}^2_{\mathrm{RMS}}=\sum_{n=1}^{\infty}\frac{a_n^2+b_n^2}{2}. \tag{B.3.6}$$

By generalizing the equation above to any function with the Fourier transform and using the approximation (B.3.4), we find our estimation of the RMS power which is

$$\mathscr{P}^2_{\mathrm{RMS}}\simeq\int_0^{\infty}|P_{\mathrm{RIR}}(\omega)|^2|\tilde{h}_+(\omega)|^2 d\omega. \tag{4.1.6}$$

(1). We can discard the constant term since $\mathscr{P}(t)|_{t=0}=0$ by the initial conditions and since the quantity vanishes on simple time average.

Appendix C

Cavity modes computation

Before getting into the computation of the electromagnetic induced power in the cavity in the time of the frequency domain, we must first compute the cavity mode-related quantities that we need. These modes are related to the cylindrical harmonics defined by equations (3.3.1) to (3.3.3),

$$\psi^r_{kmn} = C^r_{kmn} \cdot \frac{\mathscr{R}_{km}(r)}{mr} \cdot \begin{Bmatrix} \cos \\ \sin \end{Bmatrix} (m\theta) \cdot \begin{Bmatrix} \cos \\ \sin \end{Bmatrix} \left(\frac{2\pi nz}{L} \right) \tag{3.3.1}$$

$$\psi^\theta_{kmn} = C^\theta_{kmn} \cdot \frac{d\mathscr{R}_{km}(r)}{dr} \cdot \begin{Bmatrix} -\sin \\ \cos \end{Bmatrix} (m\theta) \cdot \begin{Bmatrix} \cos \\ \sin \end{Bmatrix} \left(\frac{2\pi nz}{L} \right) \tag{3.3.2}$$

$$\psi^z_{kmn} = C^z_{kmn} \cdot \mathscr{R}_{km}(r) \cdot \begin{Bmatrix} \cos \\ \sin \end{Bmatrix} (m\theta) \cdot \begin{Bmatrix} \sin \\ \cos \end{Bmatrix} \left(\frac{2\pi nz}{L} \right). \tag{3.3.3}$$

The modes for the cavities we considered are defined in [Jackson, 1998]. Here all the electromagnetic field for the TM modes in a hollow cylindrical cavity can be computed with only the longitudinal electric field E_z, defined by

$$E_z = \phi(r,\theta) \cos \left(\frac{2\pi nz}{L} \right) \tag{C.0.1}$$

where

$$\phi(r,\theta) = E_0 J_m \left(\frac{a_{mn}}{R} r \right) e^{im\theta} \tag{C.0.2}$$

is in complex notation. The other fields can be deduced with the following equations

$$\vec{E}_\perp = -\frac{2\pi n}{L\upsilon^2}\sin\left(\frac{2\pi nz}{L}\right)\vec{\nabla}_\perp\phi \quad \text{(C.0.3)}$$

$$\vec{B}_\perp = \frac{i\mu_0\omega}{\upsilon^2}\cos\left(\frac{2\pi nz}{L}\right)\vec{e_z}\times\vec{\nabla}_\perp\phi \quad \text{(C.0.4)}$$

where $\upsilon^2 = \omega^2 - \left(\frac{2\pi n}{L}\right)^2$ and $\perp$ denotes that the vector is considered only in the transverse components. The expressions for the magnetic field are consistent with our cylindrical harmonics (3.3.1) to (3.3.2). An analogous analytical treatment can be made for TE modes [Jackson, 1998]. For the TEM cavity, the same treatment can be made besides the boundary conditions for the inner conductor and the fact that there is not any longitudinal field.

We showed that only the (k,1,0) modes contributes to the induced power at first order, so we will focus on those specific modes. You can find a representation of the cylindrical harmonics ψ^r_{k10} and ψ^θ_{k10} in figure C.1.

We can now compute several quantities about the cavity modes. The first one are the resonance wavevectors α_k. For the TM resonator,a resonant frequency must satisfy equation (3.3.5) with $m = 1$,

$$J_1(\alpha_k R) = 0 \ \ \forall k \in \mathbb{N}. \quad \text{(C.0.5)}$$

The solution of such equation is $\alpha_k = \frac{a_{1k}}{R}$, where a_{1k} is the k^{th} zero of the bessel function of first kind J_1. These zeros are easily available in the `scipy` library in Python with the function `jn_zeros`. The TEM resonant frequencies are a bit more complicated to compute, since they are solution of the system made of equations (3.3.7) and (3.3.8) for $m = 1$,

$$A_k.J_1(\alpha_k R_1) + Y_1(\alpha_k R_1) = 0 \ \ \forall k \in \mathbb{N}, \quad \text{(C.0.6)}$$

$$A_k.J_1(\alpha_k R_2) + Y_1(\alpha_k R_2) = 0 \ \ \forall k \in \mathbb{N}, \quad \text{(C.0.7)}$$

which is actually a system with two variables, A_k and α_k.

We can easily rewrite this system as

$$-Y_1(\alpha_k R_1)J_1(\alpha_k R_2) + Y_1(\alpha_k R_2)J_1(\alpha_k R_1) = 0 \quad \text{(C.0.8)}$$

$$-\frac{Y_1(\alpha_k R_1)}{J_1(\alpha_k R_1)} = A_k. \tag{C.0.9}$$

We can thus solve equation (C.0.8) using the Optimization and root finding routines in `scipy`. After that, the computation of A_k is straightforward. We can thus represent the resonant frequencies for both detectors. That is what we made in the Figure (C.2). We represent the first five resonant frequencies of both cavities in function of the outer radius of the cavity. The straight lines represent the frequencies for the TM resonator and the dotted lines for the TEM resonator. The chosen inner radius for the TEM waveguide is 10 cm. Please note that in order to obtain resonant frequencies in Hertz we have to consider as resonant frequencies $\frac{c\alpha_k}{2\pi}$ which is consistent with the harmonic oscillator equation (B.1.1). The first thing that you can see is that if the outer radius

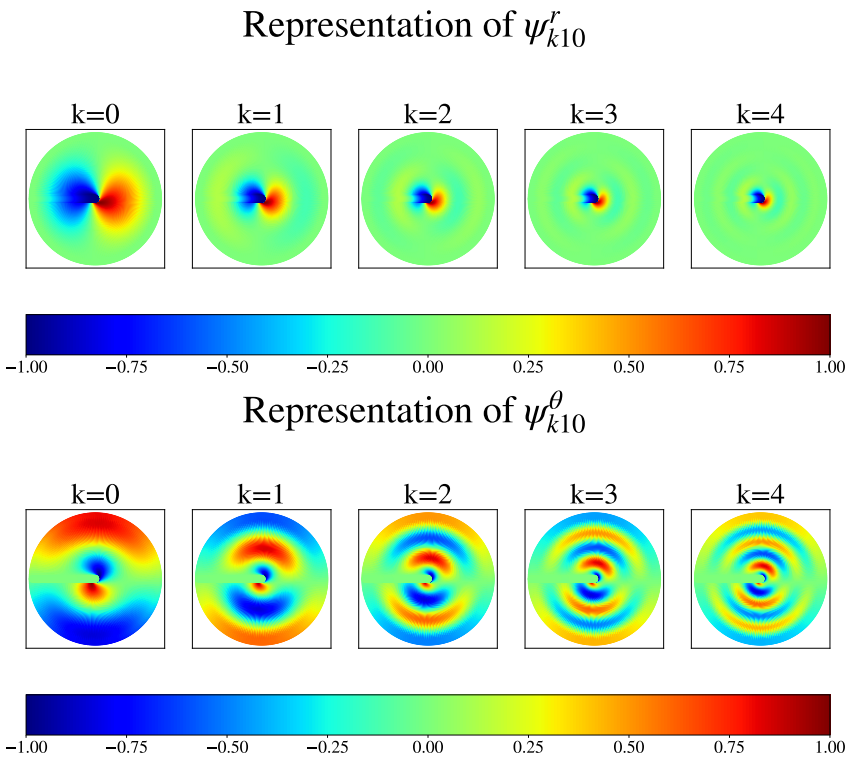

Figure C.1 – Representation of the cylindrical harmonics for the k10 modes. Since these modes are constant in the z coordinate, we only need a circular section to fully describe it. For each mode, we normalize the maximal amplitude to 1 to improve the visualization.

is quite large, the difference between the two detectors is not very significant. For the TEM waveguide, the resonant frequencies increase quickly if the outer radius is close to the inner radius. The main thing that we can learn from this figure is that the choice of the radius is very important and we have the possibility to tune this parameter to get the resonance frequencies in the same window as the signal we want to detect. Practically, if we want to use these cavities as detectors, the induced power in the cavity will be proportional to the volume of the detector, so it is not interesting to consider the case where the outer radius is close to the inner one for the TEM waveguide. In the practical case of the detection, we can consider that the resonant frequencies of the two cavities will be very close. The TEM waveguide has the advantage to produce only transverse induced field, and theoretically, there also exists the possibility to consider a detector made of concentric cylinder that could constitute a set of TEM waveguides with different radii. The TM cavity since this is just one hollow cylinder seems to be easier to elaborate, and these cavities are commonly used in experimental physics, for instance the Axion Dark Matter Experiment [Asztalos et al., 2010]. Another possibility for both detectors is to combine several cavities of different radii to get a resonant detection in a wide range of frequencies.

We can also compute the two other mode-related quantities that are the radial integral I_k and the normalization constants for the modes $C_{k10}^{r,\theta,z}$. The latter can be easily computed by considering $\|\vec{\Psi}_{k10}\| = 1$ with equations (3.3.1) to (3.3.3), and we find

$$C_{k10}^{r} = C_{k10}^{\theta} = C_{k10}^{z} = \sqrt{\frac{2}{L\pi\alpha_k^2 R^2 J_0^2(\alpha_k R)}} \tag{C.0.10}$$

for the TM cavity and

$$C_{k10}^{r} = C_{k10}^{\theta} = C_{k10}^{z} = \sqrt{\frac{2}{L\pi\left(\mathscr{F}(R_2) - \mathscr{F}(R_1)\right)}} \tag{C.0.11}$$

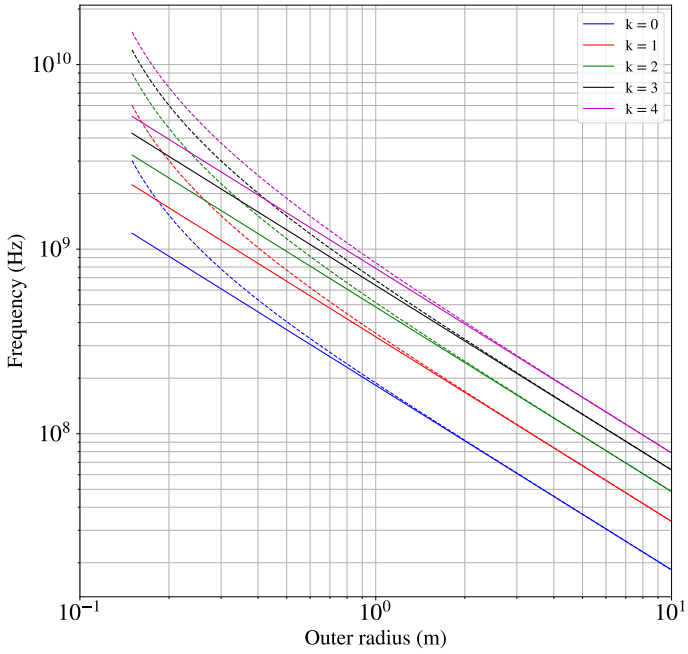

Figure C.2 – The first five resonant frequencies in function of the outer radius for the TM cavity (straight) and the TEM waveguide (dotted).

for the TEM waveguide. This normalization contains the function

$$\mathscr{F}(x) = \frac{1}{2}\left[-(A_k^2+1)\,{}_1F_2\left(\frac{1}{2};1,2;-\alpha_k^2x^2\right) - \frac{2G^{3,0}_{2,4}\left(\begin{matrix}-\frac{1}{2},\frac{1}{2}\\ -1,0,0,-\frac{1}{2}\end{matrix}\middle|\,\alpha_k x,\frac{1}{2}\right)}{\sqrt{\pi}}\right.$$

$$\left. - 2A_kJ_0(\alpha_k x)Y_0(\alpha_k x) - 2A_kJ_1(\alpha_k x)Y_1(\alpha_k x)\right], \tag{C.0.12}$$

where ${}_pF_q$ is the generalized hypergeometric function [NIST, 2011] and $G^{m,n}_{p,q}$ is the Meijer-G function [Meijer, 1936, NIST, 2011]. Those are special functions, and the computation of $\mathscr{F}(x)$ was made by symbolic computation tools.[Wolfram, 2022] The last quantity we have to compute is the I_k integral that is necessary to compute the source term of the harmonic oscillator equation (B.1.1) and the induced electromagnetic power in the cavity. For the TM resonator, we obtain

$$I_k = \frac{1-J_0(\alpha_k R)}{\alpha_k}, \tag{C.0.13}$$

and for the TEM waveguide we obtain

$$I_k = \frac{A_k - A_kJ_0(\alpha_k R_2) - Y_0(\alpha_k R_2)}{\alpha_k} - \frac{A_k - A_kJ_0(\alpha_k R_1) - Y_0(\alpha_k R_1)}{\alpha_k}. \tag{C.0.14}$$

Bibliography

Abbott, B. P., Abbott, R., Abbott, T. D., et al. (2016). Observation of Gravitational Waves from a Binary Black Hole Merger. *Physical Review Letters*, 116(6):061102, arXiv:1602.03837. doi:10.1103/PhysRevLett.116.061102.

Aggarwal, N., Aguiar, O. D., Bauswein, A., et al. (2021). Challenges and opportunities of gravitational-wave searches at MHz to GHz frequencies. *Living Reviews in Relativity*, 24(1), arXiv:2011.12414. doi:10.1007/s41114-021-00032-5.

Amaro-Seoane, P., Aoudia, S., Babak, S., et al. (2012). Low-frequency gravitational-wave science with eLISA/NGO. *Classical and Quantum Gravity*, 29(12):124016, arXiv:1202.0839. doi:10.1088/0264-9381/29/12/124016.

Antoniadis, J., Arzoumanian, Z., Babak, S., et al. (2022). The International Pulsar Timing Array second data release: Search for an isotropic gravitational wave background. *Monthly Notices of the Royal Astronomical Society*, 510(4):4873–4887, arXiv:2201.03980. doi:10.1093/mnras/stab3418.

Asztalos, S. J., Carosi, G., Hagmann, C., et al. (2010). SQUID-based microwave cavity search for dark-matter axions. *Physical Review Letters*, 104(4):41301, arXiv:0910.5914. doi:10.1103/PhysRevLett.104.041301.

Baker, R. M. (2005). Applications of High-Frequency Gravitational Waves (HFGWs). *AIP Conference Proceedings*, 746:1306–1314. doi:10.1063/1.1867259.

Baker, R. M., Stephenson, G. V., and Li, F. (2008). Proposed Ultra-High Sensitivity High-Frequency Gravitational Wave Detector. *AIP Conference Proceedings*, 969(1):1045. doi:10.1063/1.2844941.

Ballantini, R., Bernard, P., Chiaveri, E., et al. (2003). A detector of high frequency gravitational waves based on coupled microwave cavities. *Classical and Quantum Gravity*, 20(15):3505. doi:10.1088/0264-9381/20/15/316.

Bastero-Gil, M. and Subías Díaz-Blanco, M. (2021). Gravity waves and primordial black holes in scalar warm little inflation. *Journal of Cosmology and Astroparticle Physics*, 2021(12). doi:10.1088/1475-7516/2021/12/052.

Berlin, A., Blas, D., D'Agnolo, R. T., et al. (2022). Detecting high-frequency gravitational waves with microwave cavities. *Physical Review D*, 105(11):116011. doi:10.1103/PHYSREVD.105.116011.

Blanchet, L. (1987). Radiative gravitational fields in general relativity II. Asymptotic behaviour at future null infinity. *Proceedings of the Royal Society of London. A. Mathematical and Physical Sciences*, 409(1837):383–399. doi:10.1098/rspa.1987.0022.

Blanchet, L. (2014). Gravitational Radiation from Post-Newtonian Sources and Inspiralling Compact Binaries. *Living Reviews in Relativity 2014 17:1*, 17(1):1–187, arXiv:1310.1528. doi:10.12942/LRR-2014-2.

Blanchet, L. and Damour, T. (1989). Post-Newtonian generation of gravitational waves. *Ann. Inst. Henri Poincare Physique theorique*, 50(4). URL `http://www.numdam.org/item?id=AIHPA_1989__50_4_377_0`.

Boccaletti, D., De Sabbata, V., Fortini, P., et al. (1970). Conversion of photons into gravitons and vice versa in a static electromagnetic field. *Il Nuovo Cimento B Series 10*, 70(2):129–146. doi:10.1007/BF02710177.

Boccaletti, D., De Sabbata, V., Gualdi, C., et al. (1968). Gravitons in the universe. *Il Nuovo Cimento B Series 10*, 54(1):134–144. doi:10.1007/BF02711531.

Braginskii, V. B., Grishchuk, L. P., Doroshkevich, A. G., et al. (1973). Electromagnetic detectors of gravitational waves. *Zhurnal Eksperimental'noi i Teoreticheskoi Fiziki*, 65(5):1729–1737. URL `https://articles.adsabs.harvard.edu/cgi-bin/nph-iarticle_query?1974IAUS...64...54B&defaultprint=YES&filetype=.pdf`.

Braginskii, V. B. and Menskii, M. B. (1971). HIGH-FREQUENCY DETECTION OF GRAVITATIONAL WAVES. *JETP Letters*, 13(11):417–419. URL `http://jetpletters.ru/ps/1587/article_24346.pdf`.

Brito, R., Cardoso, V., and Pani, P. (2015). Black holes as particle detectors: evolution of superradiant instabilities. *Classical and Quantum Gravity*, 32(13):134001. doi:10.1088/0264-9381/32/13/134001.

Buonanno, A., Iyer, B. R., Ochsner, E., et al. (2009). Comparison of post-Newtonian templates for compact binary inspiral signals in gravitational-wave detectors. *Physical Review D - Particles, Fields, Gravitation and Cosmology*, 80(8):084043, arXiv:0907.0700. doi:10.1103/PhysRevD.80.084043.

Carr, B., Kohri, K., Sendouda, Y., et al. (2021). Constraints on primordial black holes. *Reports on Progress in Physics*, 84(11), arXiv:2002.12778. doi:10.1088/1361-6633/AC1E31.

Carr, B., Kühnel, F., and Sandstad, M. (2016). Primordial black holes as dark matter. *Physical Review D*, 94(8):083504, arXiv:1607.06077. doi:10.1103/PhysRevD.94.083504.

Caves, C. M. (1979). Microwave cavity gravitational radiation detectors. *Physics Letters B*, 80(3):323–326. doi:10.1016/0370-2693(79)90227-2.

Cruise, A. M. (1983). An interaction between gravitational and electromagnetic waves. *Monthly Notices of the Royal Astronomical Society*, 204(2):485–492. doi:10.1093/mnras/204.2.485.

Cruise, A. M. (2000). An electromagnetic detector for very-high-frequency gravitational waves. *Classical and Quantum Gravity*, 17(13):2525–2530. doi:10.1088/0264-9381/17/13/305.

Cruise, A. M. (2012). The potential for very high-frequency gravitational wave detection. *Classical and Quantum Gravity*, 29(9):095003. doi:10.1088/0264-9381/29/9/095003.

Dasgupta, A., Dev, P. S. B., Ghoshal, A., et al. (2022). Gravitational wave pathway to testable leptogenesis. *Physical Review D*, 106(7):075027, arXiv:2206.07032. doi:10.1103/PHYSREVD.106.075027/FIGURES/3/MEDIUM.

De Logi, W. K. and Mickelson, A. R. (1977). Electrogravitational conversion cross sections in static electromagnetic fields. *Physical Review D*, 16(10):2915–2927. doi:10.1103/PhysRevD.16.2915.

Domcke, V. and Garcia-Cely, C. (2021). Potential of Radio Telescopes as High-Frequency Gravitational Wave Detectors. *Physical Review Letters*, 126(2):021104, arXiv:2006.01161. doi:10.1103/PhysRevLett.126.021104.

Domcke, V., Garcia-Cely, C., and Rodd, N. L. (2022). Novel Search for High-Frequency Gravitational Waves with Low-Mass Axion Haloscopes. *PHYSICAL REVIEW LETTERS*, 129:41101. doi:10.1103/PhysRevLett.129.041101.

Einstein, A. (1915). Die Feldgleichungen der Gravitation. *Sitzungsberichte der Königlich Preußischen Akademie der Wissenschaften (Berlin)*, pages 844–847. https://einsteinpapers.press.princeton.edu/vol6-trans/130 and https://articles.adsabs.harvard.edu/pdf/1915SPAW.

Einstein, A. (1916a). Die Grundlage der allgemeinen Relativitätstheorie. *Annalen der Physik*, 354(7):769–822. doi:10.1002/andp.19163540702.

Einstein, A. (1916b). Näherungsweise Integration der Feldgleichungen der Gravitation. *Sitzungsberichte der Königlich Preußischen Akademie der Wissenschaften (Berlin)*, pages 688–696. URL https://articles.adsabs.harvard.edu/pdf/1916SPAW.....688E.

Einstein, A. (1918). Über Gravitationswellen. *Sitzungsberichte der Königlich Preußischen Akademie der Wissenschaften (Berlin)*, pages 154–167. URL https://articles.adsabs.harvard.edu/pdf/1918SPAW.....154E.

Ejlli, A., Ejlli, D., Cruise, A. M., et al. (2019). Upper limits on the amplitude of ultra-high-frequency gravitational waves from graviton to photon conversion. *European Physical Journal C*, 79(12):1–14. doi:10.1140/epjc/s10052-019-7542-5.

Ejlli, D. (2020). Graviton-photon mixing. Exact solution in a constant magnetic field. *JHEP06*, page 29. doi:10.1007/JHEP06(2020)029.

Ejlli, D. and Thandlam, V. R. (2019). Graviton-photon mixing. *Physical Review D*, 99(4):044022. doi:10.1103/PHYSREVD.99.044022.

ET steering committee (2020). Einstein Telescope: Science Case, Design Study and Feasibility Report. Technical report, ET steering committee. URL https://apps.et-gw.eu/tds/?content=3&r=17196.

Fortini, P. L. and Gualdi, C. (1982). Fermi normal co-ordinate system and electromagnetic detectors of gravitational waves - I.-Calculation of the Metric. *Il Nuovo Cimento B Series 11*, 71(1):37–54. doi:10.1007/BF02721692.

Franciolini, G., Maharana, A., and Muia, F. (2022). Hunt for light primordial black hole dark matter with ultrahigh-frequency gravitational waves. *Physical Review D*, 106(10):103520, arXiv:2205.02153. doi:10.1103/PhysRevD.106.103520.

Füzfa, A. (2016). How current loops and solenoids curve spacetime. *Physical Review D*, 93(2):24014, arXiv:1504.00333. doi:10.1103/PhysRevD.93.024014.

Füzfa, A. (2018). Devices for the directional emission and reception of gravitational waves. Patents PCT/EP2018/086758, PCT/EP2018/086760.

https://patentscope.wipo.int/search/fr/detail.jsf?docId=WO2019129745&tab=PCTDESCRIPTION and https://patentscope.wipo.int/search/fr/detail.jsf?docId=WO2019129746&_fid=WO2019129745.

Gerlach, U. H. (1992). Cavity quantum-electrodynamical response to a gravitational wave. *Physical Review D*, 46(4):1239–1262. doi:10.1103/PhysRevD.46.1239.

Gertsenshtein, M. (1960). Wave Resonance of Light and Gravitational Waves. *Journal of Experimental and Theoretical Physics*, 14(1):113. URL http://jetp.ras.ru/cgi-bin/dn/e_014_01_0084.pdf.

Goryachev, M., Campbell, W. M., Heng, I. S., et al. (2021). Rare Events Detected with a Bulk Acoustic Wave High Frequency Gravitational Wave Antenna. *Physical Review Letters*, 127(7), arXiv:2102.05859. doi:10.1103/PHYSREVLETT.127.071102.

Gourgoulhon, E. (2013). *Cours de Relativité générale*. Master Astronomie, Astrophysique et Ingénierie Spatiale - Observatoire de Paris, Universités Paris 6, Paris 7 et Paris 11, École Normale Supérieure. URL http://luth.obspm.fr/~luthier/gourgoulhon/fr/master/relat.html.

Grishchuk, L. P. (1977). Gravitational waves in the cosmos and the laboratory. *Soviet Physics - Uspekhi*, 20(4):319–334. doi:10.1070/PU1977v020n04ABEH005327.

Grishchuk, L. P. and Sazhin, M. V. (1975). Excitation and detection of standing gravitational waves. *Zhurnal Eksperimentalnoi i Teoreticheskoi Fiziki*, 68:1569–1582. URL http://adsabs.harvard.edu/abs/1975ZhETF..68.1569G.

Herman, N., Fűzfa, A., Lehoucq, L., et al. (2021). Detecting planetary-mass primordial black holes with resonant electromagnetic gravitational-wave detectors. *Physical Review D*, 104(2):023524, arXiv:2012.12189. doi:10.1103/PhysRevD.104.023524.

Herman, N., Lehoucq, L., and Fűzfa, A. (2022). Electromagnetic Antennas for the Resonant Detection of the Stochastic Gravitational Wave Background. *arXiv preprint*, arXiv:2203.15668. doi:10.48550/arxiv.2203.15668.

Hobson, M. P., Efstathiou, G. P., and Lasenby, A. N. (2006). *General Relativity*. Cambridge University Press. doi:10.1017/CBO9780511790904.

Hulse, R. A. and Taylor, J. H. (1975). DISCOVERY OF A PULSAR IN A BINARY SYSTEM. *The Astrophysical Journal*, 51:51–53. URL https://articles.adsabs.harvard.edu/pdf/1975ApJ...195L..51H.

Jackson, J. (1998). *Classical Electrodynamics*. Wiley, 3rd edition.

JASON Program office - The MITRE Corporation (2008). High Frequency Gravitational Waves. Technical report, Defense Intelligence Agency. URL https://irp.fas.org/agency/dod/jason/gravwaves.pdf.

Kahniashvili, T., Brandenburg, A., Gogoberidze, G., et al. (2021). Circular polarization of gravitational waves from early-Universe helical turbulence. *Physical Review Research*, 3(1):13193. doi:10.1103/PhysRevResearch.3.013193.

Kerr, R. P. (1963). Gravitational field of a spinning mass as an example of algebraically special metrics. *Physical Review Letters*, 11(5):237–238. doi:10.1103/PhysRevLett.11.237.

Khintchine, A. (1934). Korrelationstheorie der stationären stochastischen Prozesse. *Mathematische Annalen 1934 109:1*, 109(1):604–615. doi:10.1007/BF01449156.

Kolosnitsyn, N. I. and Rudenko, V. N. (2015). Gravitational hertz experiment with electromagnetic radiation in a strong magnetic field. *Physica Scripta*, 90(7):074059. doi:10.1088/0031-8949/90/7/074059.

Li, F., Baker, R. M. L., Fang, Z., et al. (2008). Perturbative photon fluxes generated by high-frequency gravitational waves and their physical effects. *Eur. Phys. J. C*, 56:407–423. doi:10.1140/epjc/s10052-008-0656-9.

Li, F. Y., Tang, M. X., and Shi, D. P. (2003). Electromagnetic response of a Gaussian beam to high-frequency relic gravitational waves in quintessential inflationary models. *Physical Review D*, 67(10):104008. doi:10.1103/PhysRevD.67.104008.

LIGO Scientific Collaboration (2018). LIGO Algorithm Library - LALSuite. doi:10.7935/GT1W-FZ16.

LIGO Scientific Collaboration (2022). O3B CATALOG. accessed on 2022/12/16. URL https://www.ligo.org/detections/O3bcatalog.php.

Lupanov, G. A. (1967). A CAPACITOR IN THE FIELD OF A GRAVITATIONAL WAVE. *J. Exptl. Theoret. Phys. (U.S.S.R.)*, 25(1):118–123. URL http://jetp.ras.ru/cgi-bin/dn/e_025_01_0076.pdf.

Macedo, P. G. and Nelson, A. H. (1983). Propagation of gravitational waves in a magnetized plasma. *Physical Review D*, 28(10):2382–2392. doi:10.1103/PhysRevD.28.2382.

Maggiore, M. (2007). *Gravitational Waves: Volume 1: Theory and Experiments*. Oxford University Press. doi:10.1093/acprof:oso/9780198570745.001.0001.

Maggiore, M. (2018). *Gravitational Waves: Volume 2: Astrophysics and Cosmology*. Oxford University Press. doi:10.1093/oso/9780198570899.001.0001.

Maiorano, M., De Paolis, F., and Nucita, A. A. (2021). Principles of gravitational-wave detection with pulsar timing arrays. *Symmetry*, 13(12). doi:10.3390/sym13122418.

Manasse, F. K. and Misner, C. W. (1963). Fermi normal coordinates and some basic concepts in differential geometry. *Journal of Mathematical Physics*, 4(6):735–745. doi:10.1063/1.1724316.

Marzlin, K. P. (1994). Fermi coordinates for weak gravitational fields. *Physical Review D*, 50(2):888–891. doi:10.1103/PhysRevD.50.888.

Meijer, C. S. (1936). Über Whittakersche bzw. Besselsche Funktionen und deren Produkte. *Nieuw Arch. Wiskd., II. Ser.*, 18(4):10–39. URL `https://zbmath.org/pdf/0013.20801.pdf`.

Miller, A. L., Aggarwal, N., Clesse, S., et al. (2022). Constraints on planetary and asteroid-mass primordial black holes from continuous gravitational-wave searches. *Physical Review D*, 105(6), arXiv:2110.06188. doi:10.1103/PHYSREVD.105.062008.

Minakov, A. A., Nikolaenko, A. P., and Rabinovich, L. M. (1992). Gravitational-to-electromagnetic wave conversion in electrostatic field of earth-ionosphere resonator. *Radiophysics and Quantum Electronics*, 35(6-7):318–323. doi:10.1007/BF01041780.

Misner, C. W., Thorne, K. S., and Wheeler, J. A. (1973). *Gravitation*. W. H. Freeman, San Francisco.

Moore, C. J., Cole, R. H., and Berry, C. P. (2015). Gravitational-wave sensitivity curves. *Classical and Quantum Gravity*, 32(1):015014, arXiv:1408.0740. doi:10.1088/0264-9381/32/1/015014.

Mróz, P., Udalski, A., Skowron, J., et al. (2017). No large population of unbound or wide-orbit Jupiter-mass planets. *Nature*, arXiv:1707.07634. doi:10.1038/nature23276.

Newman, E. T., Couch, E., Chinnapared, K., et al. (1965). Metric of a rotating, charged mass. *Journal of Mathematical Physics*, 6(6):918–919. doi:10.1063/1.1704351.

Newman, E. T. and Janis, A. I. (1965). Note on the Kerr spinning-particle metric. *Journal of Mathematical Physics*, 6(6):915–917. doi:10.1063/1.1704350.

Ni, W. T. and Zimmermann, M. (1978). Inertial and gravitational effects in the proper reference frame of an accelerated, rotating observer. *Physical Review D*, 17(6):1473–1476. doi:10.1103/PhysRevD.17.1473.

Niikura, H., Takada, M., Yokoyama, S., et al. (2019). Constraints on Earth-mass primordial black holes from OGLE 5-year microlensing events. *Physical Review D*, 99(8):83503, arXiv:1901.07120. doi:10.1103/PhysRevD.99.083503.

NIST (2011). NIST Digital Library of Mathematical Functions. URL `http://dlmf.nist.gov/`.

Nordström, G. (1918). On the Energy of the Gravitation field in Einstein's Theory. *Proc. K. Ned. Akad. Wet. B*, 20:1238–1245. URL `https://ui.adsabs.harvard.edu/abs/1918KNAB...20.1238N/abstract`.

Pegoraro, F., Picasso, E., and Radicati, L. A. (1978a). On the operation of a tunable electromagnetic detector for gravitational waves. *Journal of Physics A: Mathematical and General*, 11(10):1949–1962. doi:10.1088/0305-4470/11/10/013.

Pegoraro, F., Radicati, L. A., Bernard, P., et al. (1978b). Electromagnetic detector for gravitational waves. *Physics Letters A*, 68(2):165–168. doi:10.1016/0375-9601(78)90792-2.

Posen, S., Checchin, M., Melnychuk, O. S., et al. (2022). Measurement of high quality factor superconducting cavities in tesla-scale magnetic fields for dark matter searches. *arXiv preprint*, arXiv:2201.10733. doi:10.48550/arxiv.2201.10733.

Pujolas, O., Vaskonen, V., and Veermäe, H. (2021). Prospects for probing gravitational waves from primordial black hole binaries. *Physical Review D*, 104(8):083521. doi:10.1103/PhysRevD.104.083521.

Raffelt, G. and Stodolsky, L. (1988). Mixing of the photon with low-mass particles. *Physical Review D*, 37(5):1237–1249. doi:10.1103/PhysRevD.37.1237.

Rakhmanov, M. (2014). Fermi-normal, optical, and wave-synchronous coordinates for spacetime with a plane gravitational wave. *Classical and Quantum Gravity*, 31(8):085006. doi:10.1088/0264-9381/31/8/085006.

Reissner, H. (1916). Über die Eigengravitation des elektrischen Feldes nach der Einsteinschen Theorie. *Annalen der Physik*, 355(9):106–120. doi:10.1002/andp.19163550905.

Ringwald, A., Schütte-Engel, J., and Tamarit, C. (2021). Gravitational waves as a big bang thermometer. *Journal of Cosmology and Astroparticle Physics*, 2021(03):054. doi:10.1088/1475-7516/2021/03/054.

Ringwald, A. and Tamarit, C. (2022). Revealing the cosmic history with gravitational waves. *Physical Review D*, 106(6):063027. doi:10.1103/PhysRevD.106.063027.

Romberg, W. (1955). Vereinfachte numerische integration. *Norske Vid. Selsk. Forh.*, 28:30–36.

Saito, K., Soda, J., and Yoshino, H. (2021). Universal stochastic gravitational waves from photon spheres of black holes. *Physical Review D*, 104(6), arXiv:2106.05552. doi:10.1103/PHYSREVD.104.063040.

Schmieden, K. and Schott, M. (2022). Searching for Gravitational Waves with CMS. *arXiv preprint*, arXiv:2209.12024. URL `http://arxiv.org/abs/2209.12024`.

Taylor, J. H. and Weisberg, J. M. (1982). A new test of general relativity - Gravitational radiation and the binary pulsar PSR 1913+16. *The Astrophysical Journal*, 253:908. doi:10.1086/159690.

Tobar, M. E., Thomson, C. A., Campbell, W. M., et al. (2022). Comparing Instrument Spectral Sensitivity of Dissimilar Electromagnetic Haloscopes to Axion Dark Matter and High Frequency Gravitational Waves. *Symmetry*, 14(10), arXiv:2209.03004. doi:10.3390/SYM14102165.

Tsagas, C. G. (2005). Electromagnetic fields in curved spacetimes. *Classical and Quantum Gravity*, 22(2):393–407, arXiv:gr-qc/0407080. doi:10.1088/0264-9381/22/2/011.

UHF-GW community (2022). Ultra-High-Frequency Gravitational Waves Initiative. accessed on 2022/12/16. URL `https://www.ctc.cam.ac.uk/activities/UHF-GW.php`.

Verbiest, J. P., Lentati, L., Hobbs, G., et al. (2016). The international pulsar timing array: First data release. *Monthly Notices of the Royal Astronomical Society*, 458(2):1267–1288, arXiv:1602.03640. doi:10.1093/mnras/stw347.

Weyl, H. (1917). Zur Gravitationstheorie. *Annalen der Physik*, 359(18):117–145. doi:10.1002/andp.19173591804.

Wiener, N. (1930). Generalized harmonic analysis. *https://doi.org/10.1007/BF02546511*, 55(none):117–258. doi:10.1007/BF02546511.

Wolfram (2022). Wolfram|Alpha: Computational Intelligence. accessed on 2022/12/16. URL `https://www.wolframalpha.com/`.

Zheng, H. and Wei, L. F. (2022). Experimental system to detect the electromagnetic response of high-frequency gravitational waves. *Physical Review D*, 106(10):104003. doi:10.1103/PHYSREVD.106.104003.

Zheng, H., Wei, L. F., Wen, H., et al. (2018). Electromagnetic response of gravitational waves passing through an alternating magnetic field: A scheme to probe high-frequency gravitational waves. *Physical Review D*, 98(6):064028. doi:10.1103/PhysRevD.98.064028.